

Geochemistry and Mineralogy of Eastern Ag-rich Epithermal Veins in the Midas District, Nevada, USA

by

Rue Anne Chitwood

A thesis submitted to the Graduate Faculty of
Auburn University
in partial fulfillment of the
requirements for the degree of
Master of Science in Geology

Auburn, Alabama
May 7, 2012

Keywords: Epithermal, Gold-Silver, Newmont,
Mid-Miocene, Midas, Nevada

Copyright 2012 by Rue Anne Chitwood

Approved by

James A. Saunders, Chair, Professor of Geology and Geography
Willis E. Hames, Professor of Geology and Geography
Mark Steltenpohl, Department Chair of Geology and Geography

Abstract

Five Ag-rich epithermal veins were recently discovered in the eastern section of the Midas district in northern Nevada. Initial data collected indicated that these veins had a significantly higher quantity of silver relative to the main production veins at Midas. The focus of this study was on the geochemistry, ore petrography, and geochronology of three of the five eastern veins: Charger Hill, GP, and Ace. Geochemical ICP-MAS results indicate that Ag and Se occur strongly together suggesting that Ag-selenides are the dominant ore minerals while Au does not appear to have a significant correlation with any elements. An overall Ag:Au ratio for the eastern veins is 176:1. Longitudinal sections indicate that there is an elevation control on mineralization. In addition, mineralization preferentially occurs within the Elko Prince Formation and mafics sills. There is also no significant correlation between vein thickness and ore grade. SEM-EDAX results document most Ag-selenide minerals are an aguilarite-naumannite solid solution, and electrum, which is higher in Au than Ag at the atomic level, occurs in lower quantity relative to the main production veins. Overall, the paragenetic sequence suggests that the minerals were co-precipitated and overall mineralogy is similar to that of the Colorado Grande vein with the exception of the abundance of fluorite. The low quantity of Au appears to be the result of hydrothermal fluid transport dynamics, colloidal/nanoparticle transport, and the higher density of Au vs Ag implying that Au particles would not travel very far from the source. Based on the petrographic, SEM-EDAX, and ICP-MAS evidence found in this study, the eastern veins appear to be a distal product of the same large-scale magmatic-hydrothermal event that formed the main production veins.

Acknowledgements

This research was supported through an internship with Newmont Mining Corporation at their Midas Operations based out of Winnemucca, Nevada. I would like to thank everyone at the Midas mine for their guidance and assistance with this work and for giving me first-hand experience in the underground mines, and for helping me to better hone my skills as a geologist. I would especially like to thank Derick Unger, Gabriel Graf, Tom Roman, and Mike Robinson of Newmont Mining who served as my supervisors during the internship providing me with a wealth of guidance. I also thank Dr. James Saunders of Auburn University for serving as my advisor and for providing me this great opportunity with Newmont. Finally, I want to thank my family who has been my rock and my greatest supporters through everything.

Table of Contents

Abstract	ii
Acknowledgments.....	iii
List of Tables	vi
List of Figures	vii
List of Abbreviations	x
Chapter 1 Introduction	1
General Features of Epithermal Deposits	1
Objective	3
Historical and Exploration Background	4
Chapter 2 Geologic Setting	8
Regional Geology	8
District Geology	10
Geochronology	13
Structural Geology and Ore Control	15
Midas Vein Textures and Alterations	17
Chapter 3 Previous Work	20
Trace Element Geochemistry	20
Sem/MLA Studies	23
Pb Isotope and Fluid Inclusion Studies	24

Chapter 4 Methodology	27
Field Work	27
Geochemistry	30
Ore Petrography	32
Chapter 5 Results	33
Geochemistry	33
Eastern Veins Structural Interpretation	36
Ore Petrography	47
Chapter 6 Discussion	58
Chapter 7 Conclusions	65
References	67
Appendix I	77
Appendix II	78
Appendix III.....	102

List of Tables

Table 1. K/Ar and $^{40}\text{Ar}/^{39}\text{Ar}$ Dates for Midas District (Leavitt et al., 2004).	14
Table 2. Summary of Geochronology of Midas Area (Leavitt et al., 2004).	15
Table 3. ICP-MS geochemical data correlation matrix of selected elements from coarse rejects of eastern veins.	34

List of Figures

Fig. 1. Hand specimen photograph of typical epithermal crustiform texture in the Midas district. Basalt is encrusted in the center of the sample (sample provided by Dr. James Saunders; photograph by Rue Anne Chitwood, 2011).....	2
Fig. 2. Map showing the location of the northern Nevada rift and Midas mine as well as the bimodal volcanics in the northern Nevada rift (Leavitt et al., 2004).....	3
Fig. 3. Geologic map of the Midas district zoomed in on vein traces and mine workings. Veins are projected onto the surface (see list of abbreviations for rock names) (Newmont Mining, 2011).....	6
Fig. 4. <i>Left:</i> Map of the Northern Great Basin showing the Yellowstone Hotspot tracks. <i>Right:</i> Map showing the locations of epithermal deposits and mine sites in northern Nevada and southern Idaho (Saunders et al., 2008).....	9
Fig. 5. Stratigraphic column of the Midas deposit breaking down the five major stratigraphic units. (Leavitt et al., 2004).....	12
Fig. 6. Photograph of hand specimen RACGC010 65130N of Gold Crown HW (305) vein taken from 6N5130 on 6-15-11.....	19
Fig. 7. Contoured Au values (ppm) shown in a longitudinal section of the Colorado Grande vein; red line indicates outline of proven/probable ore and mined out areas (Redak, 2005).....	22
Fig. 8. Contoured Ag values (ppm) shown in a longitudinal section of the Colorado Grande vein (Redak, 2005).....	22
Fig. 9. Photomicrograph of aguilarite associating with pyrite (McComb, 2011).....	23
Fig. 10. Photograph of MUC-02054 exploration core from Ace (9052) vein.....	28
Fig. 11. Photograph of hand specimen RACGP017 44800E of GP (905) vein taken from 4-4800 on 7-18-11.....	29
Fig. 12. Scatter plot with trend line showing the correlation between Ag and Se.....	35
Fig. 13. Longitudinal section of the Charger Hill FW showing varying lithologies along the vein (modified from Gabriel Graf, Midas Mine Geology Department, 2012).....	38

Fig. 14. Longitudinal section of the Charger Hill vein showing Au equivalents along the vein (modified from Gabriel Graf, Midas Mine Geology Department, 2012).....	39
Fig. 15. Longitudinal section of the Charger Hill vein showing the true thickness of the vein (modified from Gabriel Graf, Midas Mine Geology Department, 2012).....	40
Fig. 16. Longitudinal section of the GP FW showing varying lithologies along the vein (modified from Gabriel Graf, Midas Mine Geology Department, 2012).....	41
Fig. 17. Longitudinal section of the GP vein showing Au equivalents along the vein (modified from Gabriel Graf, Midas Mine Geology Department, 2012).....	42
Fig. 18. Longitudinal section of the GP vein showing the true thickness of the vein (modified from Gabriel Graf, Midas Mine Geology Department, 2012).....	43
Fig. 19. Longitudinal section of the Ace FW showing varying lithologies along the vein (modified from Gabriel Graf, Midas Mine Geology Department, 2012).....	44
Fig. 20. Longitudinal section of the Ace vein showing Au equivalents along the vein (modified from Gabriel Graf, Midas Mine Geology Department, 2012).....	45
Fig. 21. Longitudinal section of the Ace vein showing the true thickness of the vein (modified from Gabriel Graf, Midas Mine Geology Department, 2012).....	46
Fig. 22. Photomicrograph of sample RACGP017-002 showing pyrite associated with Ag-selenide minerals and sphalerite predominately occurring around the rims of the pyrite (reflected light).....	47
Fig. 23. Photomicrograph of sample RACGP017-002 showing additional pyrite association with Ag-selenide minerals and tiny electrum grains (reflected light).....	48
Fig. 24. Photomicrograph of sample RACGP017-005 showing encrustation of pyrite within the Ag-selenide, aguilarite, and electrum and chalcopyrite also associated with the aguilarite (reflected light).....	49
Fig. 25. Photomicrograph of sample RACGP017-004 showing gangue minerals and textures. Fluorite appears isotropic. Bladed calcite and quartz indicate hydrothermal boiling had occurred (transmitted light, crossed polars).....	50
Fig. 26. Photomicrograph of sample MUC-02054-003 showing overall texture of 9052 vein with quartz, lattice calcite, bladed quartz, and bladed calcite occurring in tiny veinlets surrounded by massive fluorite (transmitted light, crossed polars).....	51
Fig. 27. Photomicrograph of sample MUC-02054-003 showing the colloform texture of chalcedony occurring around the grain boundaries of the quartz grains (transmitted light, crossed polars).....	52
Fig. 28. Photomicrograph of sample MUC-02054-006 showing pyrite “diseased” with aguilarite and a possible electrum grain (reflected light).....	53

Fig. 29. Photomicrograph of sample MUC-02054-006 with a grain of aguilarite associating with chalcopyrite and galena (reflected light).....54

Fig. 30. Photomicrograph of sample MUC-02054-002 illustrating encrustation of pyrite by aguilarite and chalcopyrite within the aguilarite (reflected light).....54

Fig. 31. Ternary diagram of atomic weight percentages of Ag vs. Se vs. S. Ace vein samples are marked with a hollow circle and GP vein samples are marked with a hollow box.....56

Fig. 32. Paragenetic sequence for the GP and Ace veins of Midas.....57

List of Abbreviations

District Vein Abbreviations:

A	Ace
C	Colorado Grande
D	Discovery
E	Gold Crown Southern Extension
G	Gold Crown
H	Gold Crown Hanging Wall
M	Homestead
P	GP
R	Charger Hill
W	Snow White

Formations and Members:

Tbg	Mafic intrusives and flows
Trf	Rhyolite flows capping the host rocks in the district
Tes5	Esmeralda Formation, upper sedimentary unit
Tes4	Esmeralda Formation, upper tuff unit
Tes3	Esmeralda Formation, middle sedimentary unit
Tes2	Esmeralda Formation, lower tuff unit

Tes1 Esmeralda Formation, lower sedimentary unit

Tep3 Elko Prince Formation, upper member

Tep2 Elko Prince Formation, middle member

Tep1 Elko Prince Formation, lower member

Tlt Lower Tuff Formation

Tjb June Belle Formation

Miscellaneous:

ANIMAL Auburn Noble Isotope Mass Analysis Lab

AuEQ Gold Equivalent

EDAX Energy Dispersive Spectrometry

FW Footwall

HW Hanging wall

ICP-AES Inductively Coupled Plasma – Atomic Emission Spectroscopy

ICP-MS Inductively Coupled Plasma – Mass Spectrometry

ME-MS41 Multi-Element – Mass Spectrometry 41

MLA Mineral Liberation Analyzer

SEM Scanning Electron Microscope

1. INTRODUCTION

GENERAL FEATURES OF EPITHERMAL DEPOSITS

Epithermal precious-metal ores are shallow hydrothermal deposits that form at temperatures less than 300°C and depths shallower than 1.5km, and the veins are epigenetic and often encrust wall fragments (Simmons et al., 2005; Fig. 1). Waldemar Lindgren (1933) originally coined the term “epithermal” ore to define any low-temperature, shallow, hydrothermal system. Typically, these hydrothermal systems form in volcanic arcs and are often associated with bimodal volcanic suites. Due to their susceptibility to erosion, most known deposits are Tertiary in age, though examples much older (e.g. Pajingo, which is a Jurassic deposit in Queensland, Australia) are known (Sillitoe and Hedenquist, 2003; Simmons et al., 2005). Most young epithermal deposits today occur around the Pacific “Rim of fire”. The mining of epithermal deposits account for an important source of gold and silver worldwide. On a global scale, epithermal ore deposits host 6% of all gold and 16% of all silver ever mined (Simmons et al., 2005). These deposits are also relatively straightforward to mine with simple techniques and have been exploited for millennia. In more recent times, precious metals extracted from epithermal ores in Latin America funded the Spanish empire in the 1500’s, and helped fuel the Nevada gold-silver rushes in the 1800’s (Abbot and Wolfe, 2003).

The Midas district hosts the largest known high-grade Au-Ag epithermal deposits within the northern Nevada rift (Fig. 2), and its age (16.5 – 15 Ma) is similar to most other the epithermal precious metal deposits of the northern Great Basin (Zoback et al., 1994; Saunders et al., 1996; Leavitt et al., 2004; Unger, 2008). These deposits are mid-

Miocene low-sulfidation systems that are associated with faulting along the rift and associated bimodal magmatism (Leavitt et al., 2004).



Figure 1. Hand specimen photograph of typical epithermal crustiform texture in the Midas district. Basalt is encrusted in the center of the sample (sample provided by Dr. James Saunders; photography by Rue Anne Chitwood, 2011).

The term low-sulfidation was coined by Hedenquist et al. (2000) and refers to the sulfidation state of the sulfide assemblage in these epithermal deposits. Some authors have suggested that bimodal magmatism associated with these ores simply was the heat source driving convection of meteoric water to leach out the gold from the crust and deposit it in the hydrothermal veins (Nash et al., 1995; John, 2001). However, Kamenov et al. (2007) found, using Pb-isotope data, that the bimodal magmatism (particularly the mafic rocks) appears to be directly linked to epithermal ore formation. In epithermal deposits, pathfinder elements occur with the targeted elements in very close spatial association. These pathfinder elements are easier to detect and they can develop broad dispersion halos, making them useful in exploration in exploration for both known and

unknown mineral deposits (Levinson, 1974; Samal et al., 2008). The pathfinder elements that typically occur with epithermal deposits include Ag, As, Sb, and Hg (Samal et al., 2008).

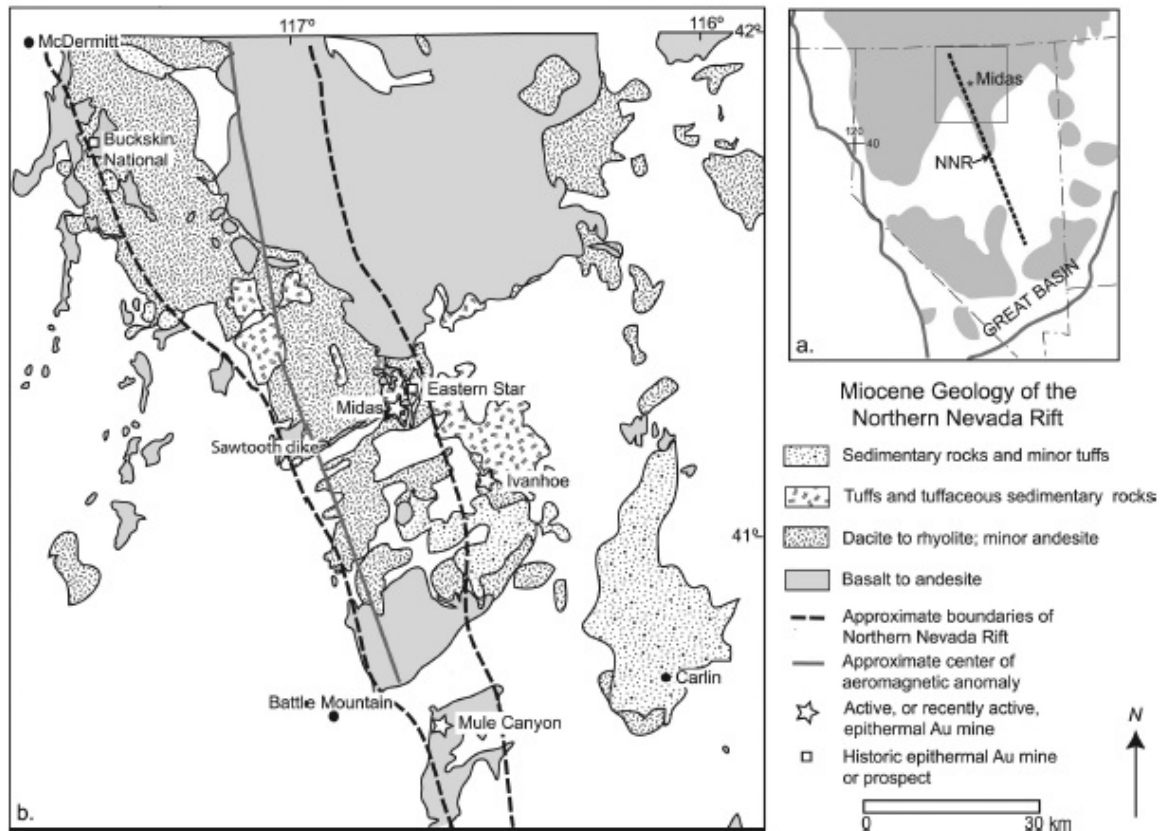


Figure 2. Map showing the location of the northern Nevada rift and Midas mine as well as the bimodal volcanics in the northern Nevada rift (Leavitt et al., 2004).

OBJECTIVE

Within the last three years, newly discovered epithermal veins in the Midas district have been found to contain an unusually high Ag:Au ratio relative to other veins within the Midas district (personal communication, Derick Unger, 2010). The veins currently being mined in the Midas district have a typical Ag:Au ratio of ~12:1, but reconnaissance assaying of the veins that are the subject of this thesis apparently indicate

significantly more silver (up to 300:1 Ag:Au ratio) than is typical (personal communication, Derick Unger and John Marma, 2011). To date, these veins have not yet been the subject of rigorous scientific study. This research seeks to better understand vein paragenesis, ore and gangue mineralogy, and geochemistry, and to apply these findings to future exploration targeting. In the process, such questions as follows will be addressed.

1) Is the mineralogy of the Ag minerals the same as the main production veins? 2) Are the ores the same age as the main production veins? 3) Did all of the Midas veins form from similar ore-forming fluids?

HISTORICAL AND EXPLORATION BACKGROUND

The Midas district is located on the southeastern end of the Snowstorm Mountains and lies roughly 64 miles NE of the town of Winnemucca (Goldstrand and Schmidt, 2000; Fig. 2). Gold-bearing veins were initially discovered in this region in 1907 by Paul Ehlers, causing a gold rush centered on the town of Midas (originally called Rosebud), which was also established in the same year (LaPointe et al., 1991; Cleverly, 1997). Initial production at Midas peaked around 1916 and then took a subsequent drop after 1921, although approximately 300,000 troy oz Au and 3 million oz Ag were produced in total between 1907 and 1930 (Goldstrand and Schmidt, 2000).

All of the historical mining in the district was done by underground workings (narrow vein stoping) from adits (Cleverly, 1997). There were seven primary veins mined in the district: Elko Prince, Rex, Link, Reco, Gold Crown, Esmeralda and Grant Jackson (Cleverly, 1997). The Elko Price and Rex mines were the two largest and long-term

producing mines (Cleverly, 1997). The Ag:Au ratio for these historic veins is 13:1 (Cleverly, 1997).

Extensive exploration was conducted in the Midas district by five major mining companies during the 1980s and 1990s (Goldstrand and Schmidt, 2000). During that time, drill holes intercepted the Colorado Grande vein directly above the current Ken Snyder mine, but relatively low assay values (<0.25 oz/ton), along with the realization that underground mining would be required at Midas, stymied initial development. Thus, the lack of an apparent bulk mineable resource at Midas, coupled to difficulty in consolidating district land positions, perhaps delayed the discovery of the world-class deposits at Midas (Goldstrand and Schmidt, 2000).

In 1992, Dr. Ken Snyder managed to assemble a controlling land package for Franco Nevada, acquired historical data, and completed a district-scale geologic map (Goldstrand and Schmidt, 2000). In 1994, Dr. Snyder began a district-wide reverse circulation (RC) drilling program, and the eighth hole intersected the Discovery vein with 25 feet grading at 0.540 oz Au/ton and 12.37 oz Ag/ton (Goldstrand and Schmidt, 2000). Intercepting the Discovery vein caused the drill program to escalate, and eventually the main vein, Colorado Grande, was intercepted (Goldstrand and Schmidt, 2000). The mine itself was constructed in 1997 and began production in late 1998. Currently there are five veins being mined (Fig. 3): Colorado Grande, Gold Crown, Gold Crown HW, Snow White, and Discovery.

Between 2006 and 2009, five new epithermal veins in the eastern part of the district were discovered (Fig. 3): Homestead, Charger Hill, GP, Bell, and Ace. The

Midas District

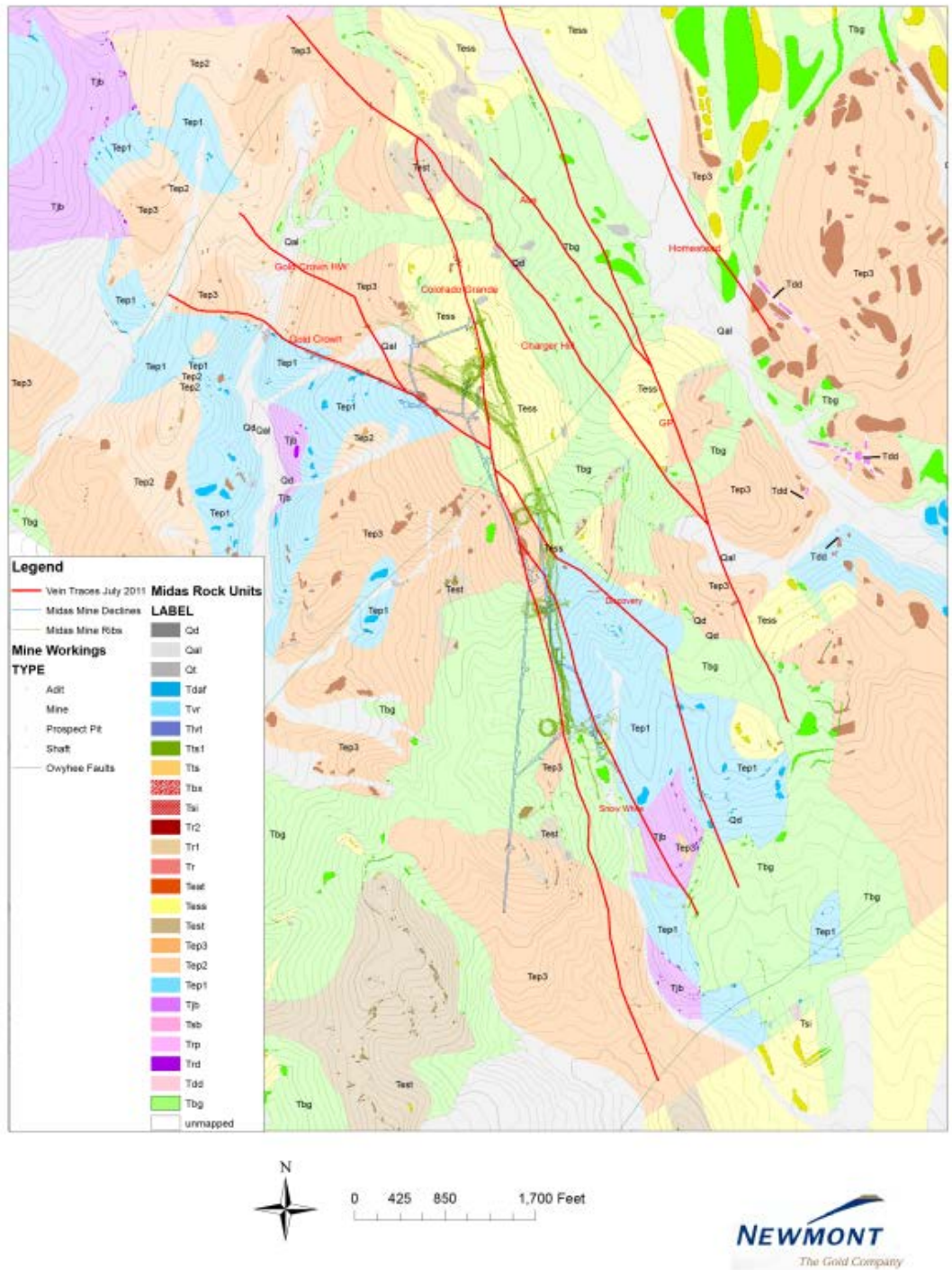


Figure 3. Geologic map of the Midas district zoomed in on vein traces and mine workings. Vein traces are projected onto the surface (see page x and xi for rock abbreviations)(Newmont Mining, 2011).

Charger Hill, GP, and Ace veins are the most significant in terms of vein thickness and grade, and so these three veins are the focus of this study.

Exploration on the eastern veins goes back to 2006 when Charger Hill was identified as a target due to a geophysical anomaly to the southeast of the Discovery vein (personal communication, John Marma, 2011). The same year, Stephen Redak drilled a surface RC hole hoping to intersect the strike of the Charger Hill vein beneath a mafic sill, which was thought to be a vital factor in grade mineralization, but the hole turned out to be a disappointment in both grade and geology (personal communication, John Marma, 2011).

In 2008, the Charger Hill target was reviewed and later confirmed as a drill target. Five holes were drilled and one intersected the ore grade mineralization along the Charger Hill vein (personal communication, John Marma, 2011). An extension of the Gold Crown (Gold Crown Southern Extension) was also discovered with this drill program. An exploration drill hole managed to intersect the GP vein, which was an unknown target at the time, and showed anomalous Au:Ag geochemistry (personal communication, John Marma, 2011). The discovery of the Gold Crown Southern Extension and Charger Hill veins prompted more drilling and confirmed the continuity of the mineralization of these veins as well as the GP vein (personal communication, John Marma, 2011).

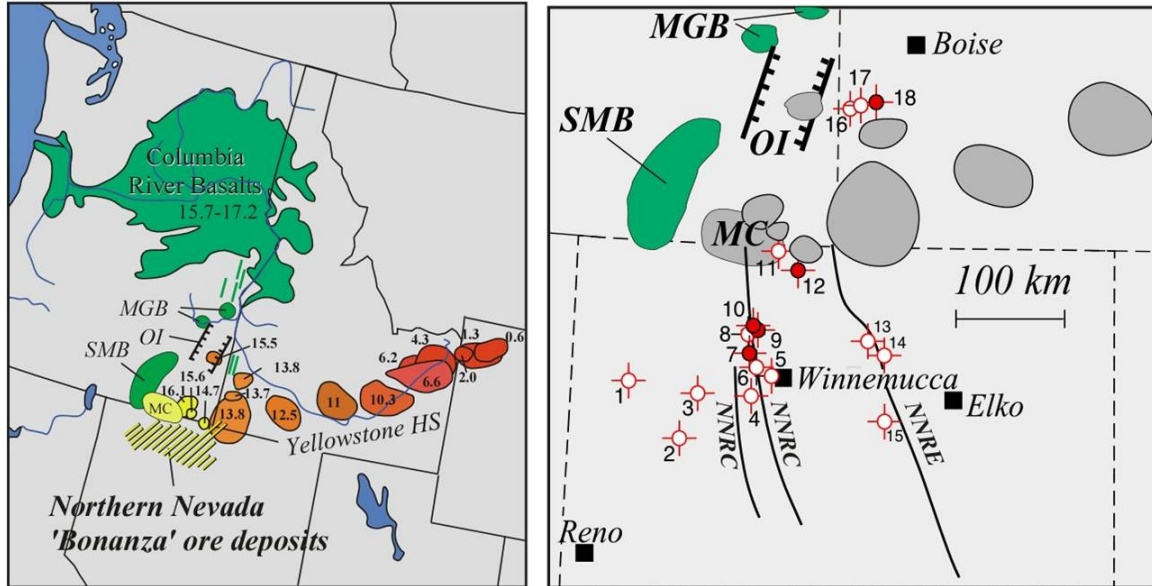
2. GEOLOGIC SETTING

REGIONAL GEOLOGY

The Great Basin is the widest portion of the Basin and Range taphrogen that extends from central Mexico to the Pacific Northwest and occupies a 600x600km² area of internally drained, very rugged topography, the bulk of which is located in Nevada and parts of Utah and California (Dickinson, 2006; Fig. 4). The tectonic history of the Great Basin consists of extensive rifting events that began along the western edge of Precambrian Laurentia (Dickinson, 2006). During Cenozoic, two successive phases of extensional deformation occurred with the most recent occurring during Miocene, after the establishment of the San Andreas Fault in southern California that divides the Pacific and North American plates (Dickinson, 2006).

In the backarc of the Pacific Northwest, basaltic magmatism occurred simultaneously with the eruption of the Columbia River-Steens basalts during the middle part of the Miocene, and these basalts preserve the relationship between coeval magmatism and precious metal mineralization (Dickinson, 2006; Brueseke, 2010; Fig. 4). The northern Great Basin experienced rifting and extension-related bimodal volcanism, both of which are attributed to having formed the low-sulfidation epithermal deposits during middle Miocene (John, 2001). This bimodal volcanism is also associated with the initial emergence of the Yellowstone hotspot (John, 2001; Brueseke et al., 2007; Fig. 4). The volcanics in the Midas district have been deformed into a district-wide dome that has a northwest trend, shallow southeast plunge, and shallow dip (Blair, 1991; Wallace, 1993;

Cleverly, 1997; Casteel et al., 1999; Goldstrand and Schmidt, 2000; Rhys, 2002; Leavitt, 2004; Leavitt et al., 2004).



- | | | | |
|-----------------------------|-------------------|--------------|---------------------|
| SMB: Steens Mountain basalt | 1 Hog Ranch | 7 Sandman | 13 Midas |
| MGB: Malheur Gorge basalt | 2 Seven Troughs | 8 New Alma | 14 Ivanhoe |
| OI: Oregon-Idaho Graben | 3 Rosebud | 9 Jumbo | 15 Mule Canyon |
| MC: McDermitt Craters | 4 Tenmile | 10 Sleeper | 16 DeLamar |
| | 5 Winnemucca Mtn. | 11 McDermitt | 17 Florida Mountain |
| | 6 Golden Amethyst | 12 National | 18 War Eagle Mtn. |

Figure 4. Left: Map of the Northern Great Basin showing the Yellowstone Hotspot tracks. **Right:** Map showing the locations of epithermal deposits and mine sites in northern Nevada and southern Idaho (Saunders et al., 2008).

The northern Nevada rift (Fig. 2) was defined by Zoback and Thompson (1978) as the southern extension of a 700km distinct, north-northwest-trending magnetic anomaly extending from the Oregon border down to east-central Nevada. The northern Nevada rift is crosscut by east-west-striking faults locally called “Owyhee structures” (Riederer, 2007). These Owyhee structures exhibit pre- and post-mineralization displacement, interpreted to reflect reactivation of the pre-mineralization fault structures (Riederer, 2007). There are many mineral occurrences that include gold, silver, mercury, lithium, uranium, tin, and zeolites, but the epithermal gold-silver occurrences are the

most important deposits in the rift (John and Wallace, 2000). The rock types within the northern Nevada rift vary from north to south and include sequences of mafic-felsic volcanic and hypabyssal intrusives underlain by clastic sedimentary rocks (John et al., 2000). The predominant country rocks for all the Northern Great Basin Mid-Miocene Au:Ag deposits are broken down into four groups: (1) Mesozoic metasedimentary phyllites, schists, and metaconglomerates; (2) Mesozoic granitoid intrusions; (3) mid-Miocene rhyolites; and (4) middle Miocene mafic volcanics (Saunders et al., 2008). The rift is not characterized by prominent faults with large displacement nor are the margins distinct. In most places, the internal structure is poorly exposed due to alluvial deposits while in others, the structural characteristics are nearly absent (John et al., 2000). There are only two places where the internal structure can be observed, the Argenta and Malpais Rims (John et al., 2000). The Rims are northeast- to east-northeast-trending upthrown fault blocks formed during late Miocene bounded by steep, north-dipping faults, providing good cross sections of the rocks erupted within the rift (John et al., 2000). As a whole, the northern Nevada rift was produced by two major processes, region-wide extension and the emplacement of Yellowstone-related magmas in the upper crust (John et al., 2000). Overall, the framework of this region is defined by the bimodal magmatism, extensional tectonics, and precious-metal deposit formation (Brueseke, 2010).

DISTRICT GEOLOGY

The Midas deposits are low-sulfidation, selenide-rich, epithermal veins that formed along this northern Nevada rift (Leavitt et al., 2004; Fig. 2,3). The district itself is

completely underlain by Miocene age lithologies. The host rocks in the Midas district exhibits regional propylitic alteration and silicification comprise welded volcanic tuffs, lacustrine sediments, mafic and felsic dikes and sills, and a clastic dike (Goldstrand and Schmidt, 2000; Leavitt et al., 2004).

Casteel et al. (1999) and Goldstrand and Schmidt (2000) defined five major stratigraphic units (Fig. 5) within the district based on results from mapping and drilling of the area: June Belle Formation (Tjb, Trvt), Lower Tuff (Tlt), Elko Prince Formation (Tep), Esmeralda Formation (Tes), finely crystalline gabbroic sill (Tbg1), and coarsely crystalline gabbroic sill (Tbg2). The June Belle Formation (Fig. 5) is the oldest exposed lithology within the district and consists of greenish-colored, strongly welded, lithic crystal ash flow tuff with a thickness of around 39.4-800 feet (Rhys, 2002). Lithic fragments are mostly felsic in nature and display a eutaxitic texture (Rhys, 2002). June Belle formation overlies a Lower Tuff sequence that can be up to 2500 feet thick consisting of a moderately welded crystal-lithic tuff with certain portions resembling the Elko Prince Formation texturally (Rhys, 2002; Goldstrand and Schmidt, 2000).

The Elko Prince (Fig. 5) can be subdivided into three sub-members: a lower member (Tep1), middle member (Tep2), and an upper member (Tep3). The lower member (Tep1) is a green-colored lithic tuff with possible inclusions of lithic fragments, strongly welded tuff, ash tuff, and mafic fragments that can be as thick as 499 feet (Rhys, 2002). The middle member is a grayish-green laminated volcaniclastic sandstone, siltstone, and mudstone that can be up to 102 feet thick and represents a lacustrine deposition (Goldstrand and Schmidt, 2000). The upper member (Tep3) is a green-colored, poorly welded crystal lapilli tuff, which contains anywhere from 10-30%

strongly chloritized lapilli and sanidine crystals within a fine-grained vitric groundmass and can be from 102-351 feet thick (Rhys, 2002; Goldstrand and Schmidt, 2000).

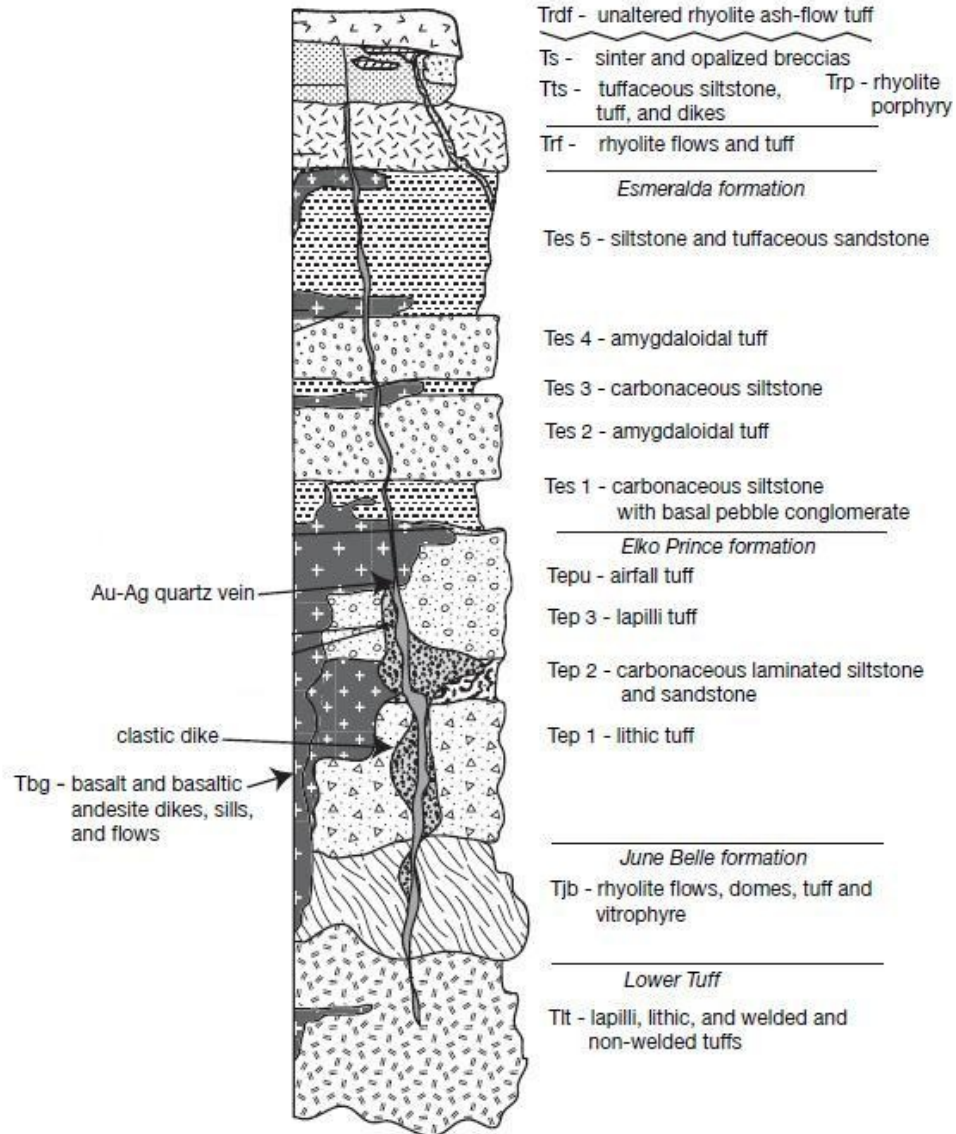


Figure 5. Stratigraphic column of the Midas deposit breaking down the five major stratigraphic units. (Leavitt et al., 2004).

The Esmeralda Formation (Fig. 5) is the highest stratigraphic unit in the sequence that can be broken down into five sub-members: Tes1, Tes2, Tes3, Tes4, and Tes5. Three of the members are sedimentary and are separated by two basalt flows altered to resemble tuffs (Rhys, 2002; Rhys and Ross, 2004). These members are composed of laminated

sandstone, siltstone, and mudstone with minor pebble conglomerates that also record lacustrine deposition much like the Tep2 unit and can also include some plant fragments (Rhys, 2002). The two lower members are less than 98 feet thick, but the uppermost member can be as thick as 351 feet (Rhys, 2002). The basalts occur with an ash tuff with calcite-quartz filled amygdaloids, and can be up to roughly 180 feet and can be undistinguishable if the second sedimentary member is absent (Rhys, 2002). Overall this formation is believed to originate from a pyroclastic flow going into a lake setting based on the presence of columnar jointing, amygdaloids, and perlitic textures (Rhys, 2002; Goldstrand and Schmidt, 2000).

The Colorado Grande vein is one of the primary veins within the Midas district. This vein strike varies from north-south to thirty degrees northwest and dips from seventy five degrees northeast to near vertical, and contains multiple secondary veins that dip steeply northeast (Redak, 2005). The dominant ore minerals are electrum, aguilarite, and naumannite while the dominant gangue minerals are calcite, quartz, and adularia (Redak, 2005). The K-feldspar adularia is a scientifically important mineral in low-sulfidation ores because it is an excellent mineral for age dating because of its high potassium composition (Hames et al., 2009).

GEOCHRONOLOGY:

Geochronology studies conducted in the Midas district are limited, but Leavitt (2004) and Leavitt et al. (2004) are the most extensive and detailed work on geochronology within the district (Table 1,2). The general time frame for the bimodal volcanism event and subsequent formation of low-sulfidation epithermal deposits is

placed around 17-13 Ma during the middle Miocene after various gangue minerals in the veins and host rock were age dated using K/Ar and Ar/Ar dating methods (Hames et al., 2009). Leavitt et al. (2004) utilized $^{40}\text{Ar}/^{39}\text{Ar}$ dating techniques to date adularia from samples of the Colorado Grande vein, Eastern Star vein, Tep3, rhyolite tuff, red rhyolite, basalt, and basaltic andesite. The adularia from the Colorado Grande and Eastern Star veins yielded an age date range of 15.3-15.4 Ma (Table 2), but the dates from the inner and outer bands couldn't be distinguished indicating that the vein formed over a short period of time and at no less than 400 kyr after the youngest host rocks based on error bars (Leavitt et al., 2004). Leavitt et al. (2004) also concluded that hydrothermal activity ceased at 15.2 Ma as there was little to no hydrothermal alteration.

Table 1. K/Ar and $^{40}\text{Ar}/^{39}\text{Ar}$ Ar Dates for Midas District (Leavitt et al., 2004).

Sample ID	Unit / Vein	Material Dated	K/Ar (Ma \pm σ)		$^{40}\text{Ar}/^{39}\text{Ar}$ (Ma \pm σ)			
				Isochron	Total Gas Age	Plateau	Mean	Weighted Mean
MI-S-70	Trdf	sanidine		15.23 \pm 0.10* (MSWD = 1.8)			15.48 \pm 0.36	15.39 \pm 0.08
MJV-KS-1 ¹	C.G. vein	adularia				15.26 \pm 0.05		
MI-S-4	C.G. vein; sp4/5250 S/462'	adularia; outer band		15.30 \pm 0.08* (MSWD = 1.3)	15.35 \pm 0.08	15.30 \pm 0.08		
MI-S-3	C.G. vein; sp4/5250 S/462'	adularia; inner band		15.37 \pm 0.09* (MSWD = 1.8)	15.42 \pm 0.08	15.38 \pm 0.08		
MI-S-7	Eastern Star vein	adularia		15.40 \pm 0.09* (MSWD = 1.2)	15.33 \pm 0.10	15.39 \pm 0.10		
DRS-9-67 ²	Mineralized vein in altered rhyolite	adularia	15.4 \pm 0.8					
MI-S-61	Trf	sanidine		15.63 \pm 0.12* (MSWD = 0.31)			15.65 \pm 0.05	15.65 \pm 0.08
MI-S-17	Tepu	sanidine		15.60 \pm 0.09 (MSWD = 0.97)	15.91 \pm 0.11	15.74 \pm 0.11*		
9LH25 ³	Tba	whole rock	14.7 \pm 0.5					
MI-S-1	Tbg	plagioclase		13.22 \pm 0.15 (MSWD = 1.6; excess argon)	19.37 \pm 0.26	15.9 \pm 0.3* (maximum age)		
MKK-PG-29	Tbg	plagioclase		8.2 \pm 1.05 (MSWD = 2.2; excess argon)	17.59 \pm 0.20	16.0 \pm 0.2* (maximum age)		

The adularia sampled for geochronology by Leavitt et al. (2004) was finely grained and intergrown with quartz, requiring that the age data for that study be obtained

by incremental heating of quartz-adularia mixtures in bulk samples. The approach of Leavitt et al. (2004) is efficient, but limited in ability to resolve variations in single crystal ages that may occur, or the potential for loss of radiogenic ^{40}Ar from the relatively small feldspars during cooling. Adularia crystals in the present study also tend to be finely grained (generally less than 50 μm in diameter) and intergrown with quartz, such that the present study samples are not amenable to single-crystal methods for analyzing adularia (e.g., Hames et al., 2009; Aseto in prep.).

Table 2. Summary of Geochronology of Midas Area (Leavitt et al., 2004).

Rock type / unit	$^{40}\text{Ar}/^{39}\text{Ar}$ Dates ($\text{Ma} \pm \sigma$)	Material Dated	Comments	Other Dates ($\text{Ma} \pm \sigma$)	Material Dated
Trdf, rhyodacite tuff, 5 km NE of Ken Snyder Mine / MI-S-70	15.23 \pm 0.10	sanidine	isochron age (MSWD = 1.8); weighted average age from laser fusion of 10 single crystals; - 15.39 \pm 0.08		
Colorado Grande vein, Ken Snyder Mine / MJV-KS-1 ¹	15.26 \pm 0.05	adularia			
Colorado Grande vein / average of 2 new dates	15.34 \pm 0.08	adularia			
Colorado Grande vein, Ken Snyder Mine / MI-S-4 / sp4/5250S/462 ²	15.30 \pm 0.08	adularia; outer band	isochron age (MSWD = 1.3); plateau age - 15.30 \pm 0.08		
Colorado Grande vein, Ken Snyder Mine / MI-S-3 / sp4/5250S/462 ²	15.37 \pm 0.09	adularia; inner band	isochron age (MSWD = 1.8); plateau age - 15.38 \pm 0.08		
Ivanhoe deep vein, 15 km SE of Ken Snyder Mine ²	15.38 \pm 0.08	adularia			
Trpoi, Sawtooth dike, feeds flows of Trpo overlying Trf ³	15.39 \pm 0.02	sanidine		14.3 \pm 0.8, K/Ar, Trpoi ⁴	sanidine
Eastern Star vein, 5 km E of Ken Snyder Mine / MI-S-7	15.40 \pm 0.09	adularia	isochron age (MSWD = 1.2); plateau age - 15.39 \pm 0.10.		
Mineralized vein in altered rhyolite, Midas district / DRS-9-67 ⁵				15.4 \pm 0.8, K/Ar	adularia
Trf, rhyolite flow east of Squaw Creek / MI-S-61	15.63 \pm 0.12	sanidine	isochron age (MSWD = 0.31); weighted average age from laser fusion on 10 single crystals - 15.65 \pm 0.08		
Tepu, crystal-rich tuff at top of Elko Prince formation / MI-S-17	15.74 \pm 0.11	sanidine	plateau age; isochron age - 15.60 \pm 0.09 (MSWD = 0.97)		
Tbg, basalt overlain by Esmeralda formation / MI-S-1	15.9 \pm 0.3 ⁵	plagioclase	plateau age; isochron age - 13.22 \pm 0.15 (MSWD = 1.6)		

STRUCTURAL GEOLOGY AND ORE CONTROL

The Midas district is classified as a district-wide dome with a north-northwest trend and southeastern shallow plunge, and shallow dip, and is cross-cut by a series of pre- and post-mineralization east-west striking faults (Goldstrand and Schmidt, 2000;

Riederer, 2007; Fig. 3). The ore-bearing veins occur in a conjugate set of faults that dip steeply. These faults display two primary orientations: 1) NS-N30°W and 2) N50°-60°W (Goldstrand and Schmidt, 2000). The Colorado Grande vein displays the former orientation, has a dip from 75°NE to near vertical, and exhibits structural continuity for nearly 6,562 feet without faulting (Goldstrand and Schmidt, 2000). Both fault orientations show pre-mineral normal and right-lateral offset with trace post-mineral brecciation of the vein (Goldstrand and Schmidt, 2000). These pre-mineralized structures formed before 15.2 Ma and were reactivated during the extension of a ENE-trending structure known as the Midas trough, which formed before 6 Ma (Goldstrand and Schmidt, 2000). The Gold Crown HW, Snow White, and Discovery veins are all splay veins to the Colorado Grande vein in the hanging wall and foot wall. Although the Gold Crown is a splay off the Colorado Grande vein, it exhibits the second principle vein orientation of N50°-60°W.

Ore mineralization occurs along specific depths, thicknesses, and distances even though highly anomalous Au-Ag mineralization occurs. Mineable reserves on the Colorado Grande vein occur over a 6,470 ft. strike length and vertical extent of 1,699 ft. (Goldstrand and Schmidt, 2000). The reserves on the subsidiary veins have a shorter vertical extent of roughly 800 ft. on Gold Crown and 295 ft. on the Discovery, and width extents of about 1-20 ft. for the Gold Crown which is a substantial width for a vein (Goldstrand and Schmidt, 2000). At depth, the veins tend to pinch out and form as quartz-filled veinlets. As a result, the Au-Ag grades decrease significantly (due to dilution) over the mining width, which leads to the deposit model that minerable reserves and well-developed veins will not occur below 5,699 ft. (Goldstrand and Schmidt, 2000). On the

surface, the vein outcrops are not well developed and exposure of the Colorado Grande and Gold Crown shows narrow shear zones with inclusions of iron oxides, clay, and clear quartz veinlets surrounded by wall rock silicification (Goldstrand and Schmidt, 2000).

The eastern veins, however, are different from the currently mined veins both in dip direction and their lack of surface expression. In general, the currently mined veins all dip east while the eastern veins all dip steeply west. Recorded strike and dips from the eastern veins by Newmont are as follows: Charger Hill (S50E/80W), GP (S67E/72W), and Ace (S45E/70W).

MIDAS VEIN TEXTURES AND ALTERATIONS

There are three primary types of alteration that occur in the wall rocks and veins of the Midas mine: propylitic, silicic, and argillic. Propylitic alteration is the most common type of alteration at the mine and is readily identified by the presence of chlorite and epidote, which generally stains the matrix varying shades of green, and can also include the presence of calcite and pyrite. Chlorite appears to be the more common indicator mineral of propylitic alteration but epidote also tends to occur at higher temperatures (Goldstrand and Schmidt, 2000). Adjacent to the veins, the wall rock appears bleached but this is still propylitic alteration (Goldstrand and Schmidt, 2000).

Silicic alteration is characterized by a milky texture and occurs locally adjacent to the veins. Silicic alteration is essentially where silica floods into the wall rock during vein formation and dissipates outward. Montmorillonite, a common clay mineral, also occurs with silicic alteration as fracture coatings and veinlets adjacent to the actual veins (Goldstrand and Schmidt, 2000). Argillic alteration is most pronounced in the upper

levels of the hanging walls of the Colorado Grande and Gold Crown veins, and is lithologically dependent (Goldstrand and Schmidt, 2000). Argillic alteration typically occurs in Tep3 and is characterized by a noticeable change in the hardness of the wall rock as it becomes more clay-like.

The Colorado Grande and Gold Crown veins developed during episodes of brecciation and deposition where silica flooding of the wall rocks occurred, followed by deposition of the banded veins (Leavitt et al., 2004). The dark banding in the veins is defined by relative abundance of electrum, naumannite, chalcopryrite, pyrite, sphalerite with minor occurrences of galena, aguilarite, and marcasite (Leavitt et al., 2004; Fig. 6). The white banding consists of quartz, chalcedony, adularia, and calcite (Leavitt et al., 2004; Fig. 6). Early banding shows bladed calcite, adularia, and mosaic quartz while later banding shows more pyrite and crystalline quartz (Leavitt et al., 2004). While deposition of the banding was occurring, brecciation also occurred causing disturbances within the wall rock and vein and during this time calcite and silica were deposited (Leavitt et al., 2004). Overall vein formation episodes can be divided into six primary stages and multiple accompanying substages within each one (Leavitt and Arehart, 2005).

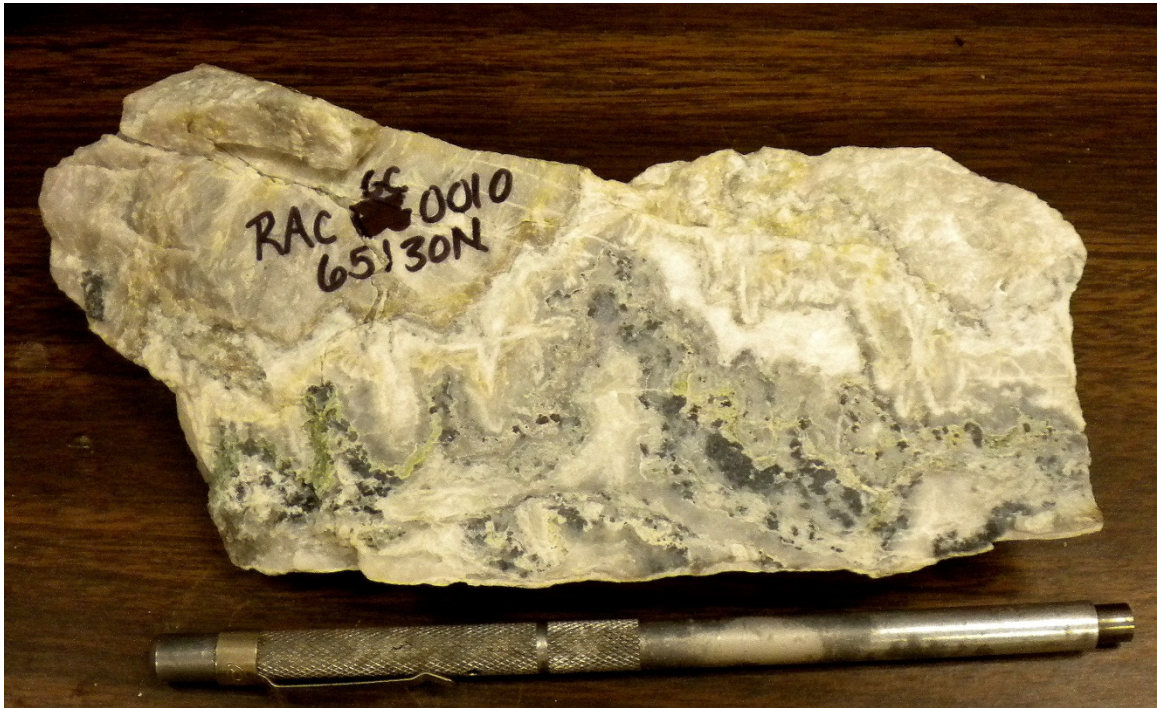


Figure 6. Photograph of hand specimen RACGC010 65130N of Gold Crown HW (305) vein taken from 6N5130 on 6-15-11.

Epithermal deposits in the western U.S. can display ore textures indicative of hydrothermal solutions that transported mineral colloids, and the assemblage of electrum and silica colloids is often synonymous with the formation of bonanza ores (Saunders et al., 2010). Two end-member colloid textures for electrum and naumannite are formally recognized, dendrites and draping features (Saunders et al., 2010). The dendrites protrude from the vein walls while the draping features (“sluice-box” textures) form precious-metal colloids around vein-wall protrusions (Saunders et al., 2010). Additionally, irregularities have been observed as a texture indicative of colloidal particles being precipitated by ore-forming fluids (Saunders et al., 2010). Naumannite colloids also form a texture that appears to have resulted from the deposition of particles on the lee side of vein wall protrusions (Saunders et al., 2010). Un-replaced platy calcite typically forms vein wall protrusions at Midas (Saunders et al., 2010).

3. PREVIOUS WORK

TRACE ELEMENT GEOCHEMISTRY

Five trace-element geochemical studies have been conducted in the Midas district. Blair (1991) studied the Junebell vein and found that As, Sb, and Hg values significantly increased while Cu, Pb, and Zn values significantly decreased going from 985 ft. depth to the surface. Goldstrand (2001) found Au, Ag, As, Se, Hg, B, Sb, Pb, Ti, and Cu to be most useful for surface geochemical exploration for buried veins. Leavitt and Arehart (2005) conducted a major geochemical study focusing on alteration zones and found that Hg and As form halos over the projection of the veins and broaden near the surface. Additionally, they found that Hg, As, and Sb increase in veins at higher elevations and base metals are more enriched with depth (Leavitt and Arehart, 2005). Cleverly (1997) looked at the trace element geochemistry within various types of wall rock and veins.

Cleverly (1997) collected samples from coarse “rejects” (already sampled and crushed) that were sent out for Au-Ag assays. Because of the extensive nature of this sample medium, a broad range of geologic environments could be studied to analyze trace and minor elements for Cu, Mo, Pb, Zn, Ag, Ni, Co, Mn, Cd, V, Be, Li, Sr, Rb, As, Sb, Hg, Se, Te, Sn, Tl, W, and Bi. He concluded that magmatic porphyry fluids could account for the observed elevated concentrations of W and Mo in mineralized material. He also proposed that base metals may have moved into the system (excluding Zn because it is depleted in comparison to wall rock); metal phases in mineralized material is limited to naumannite, acanthite, solid solution seleniferous electrum, seleniferous galena, chalcopyrite, sphalerite, and pyrite; and AuAg, Ag, and Pb are precipitated in the

aforementioned succession as selenium-rich compounds from silver selenides, electrum, and galena (Cleverly, 1997).

Finally, Redak (2005) conducted a trace-element zonation study to the Colorado Grande vein. Mineralization that he studied is confined to a horizontally-oriented ore horizon occurring around 4,501-5,619 ft. depth. He sampled all throughout and around the vertical extents of the ore horizon in order to deduce the trace-element patterns. Redak (2005) determined that Au, Ag, Se, and As are the only useful elements for exploration purposes, and mercury is closely affiliated with Au in the vein and is also found where surface sinters are preserved. Arsenic is enriched above the ore body and no base-metal enrichment is seen except for Cu at depth (Redak, 2005).

Redak (2005) plotted all his trace element data on longitudinal sections to show the distribution of elements within the Colorado Grande vein, and the plots show that the elements are irregularly distributed. The only elements that show regular zonation are Au, Ag, Se, Hg, As, and Cu (Redak, 2005; Figs. 7 and 8).

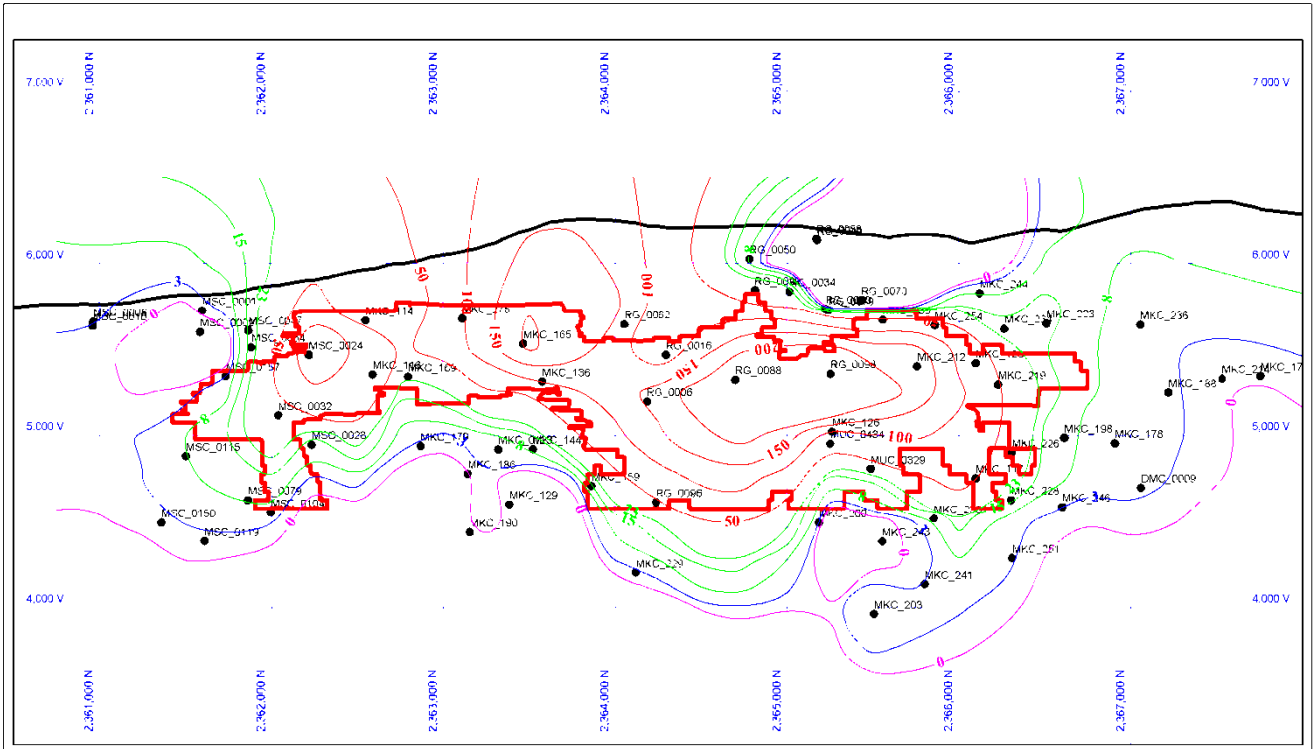


Figure 7. Contoured Au values (ppm) shown in a longitudinal section of the Colorado Grande vein; red line indicates outline of proven/probable ore and mined out areas (Redak, 2005).

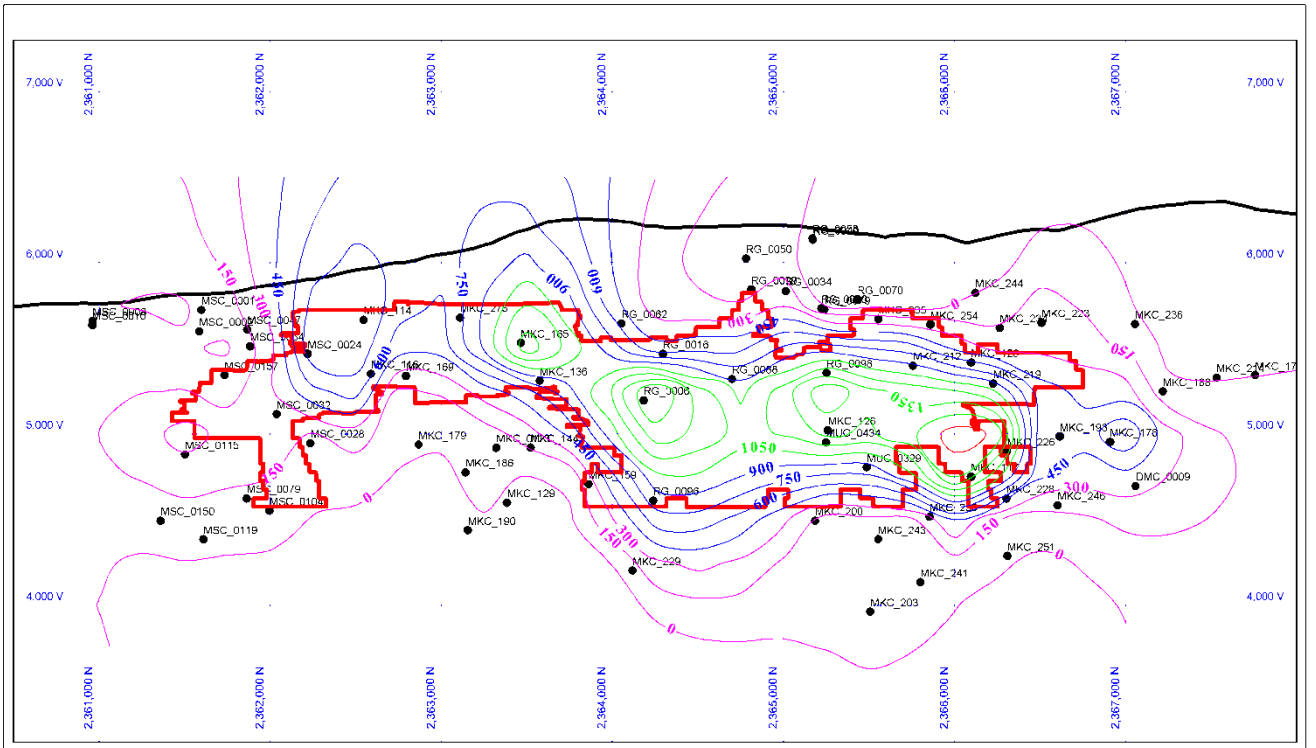


Figure 8. Contoured Ag values (ppm) shown in a longitudinal section of the Colorado Grande vein (Redak, 2005).

SEM/MLA STUDIES

In early 2011, Newmont Mining conducted a silver mineral characterization by Scanning Electron Microscope/Mineral Liberation Analyzer (SEM/MLA) of the eastern veins in the Midas district. This study was done at the Plato Malozemoff Technical Facility Newmont Metallurgical Services in Englewood, Colorado. The MLA involves a combination of a large specimen chamber automated SEM, multiple Energy Dispersive X-ray detectors (EDAX), and automated quantitative mineralogy software. The results of the SEM/MLA indicate that the Ag occurrence in the eastern veins is identical to historic production veins and occurs predominately as aguilarite (Ag_4SeS) 71.6% and naumannite (Ag_2Se) 27.9% with minor amounts of electrum 0.5% (McComb, 2011). The aguilarite and naumannite is mostly associated with quartz and pyrite (McComb, 2011; Fig. 9).

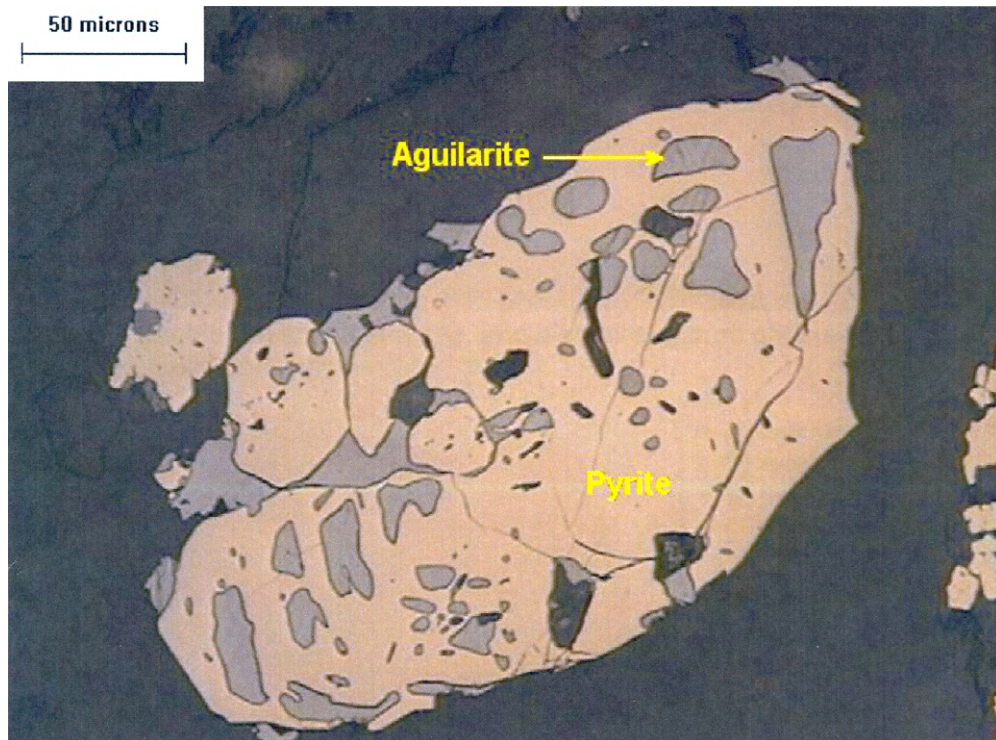


Figure 9. Photomicrograph of aguilarite associating with pyrite (McComb, 2011).

Pb ISOTOPE AND FLUID INCLUSION STUDIES

Multiple geochemical studies have been conducted within the Midas district and northern Nevada region in an effort to more accurately determine the sources of gold in the Mid-Miocene epithermal deposits. These include Pb-isotope analysis, ICP-MS analysis, and fluid inclusion studies. Saunders et al. (2010) conducted a Pb-isotope analysis study. Traditionally, classification schemes for epithermal deposits have generally focused more on the gangue minerals present, which are known to be good markers for ore-forming fluid chemistry. A geochemical classification scheme for low-sulfidation deposits, however, has not yet been developed (Saunders et al., 2010). Saunders et al. (2010) took a classic trilinear diagram and modified it so that molar ratios of Au, Ag, and Pb were normalized and plotted in the cations triangle, and treated Se, Te, and Sb+As in the same fashion plotted on the anions triangle. Since Pb, As, and Sb are very common elements in epithermal deposits and carry higher background levels than the other elements listed above, the concentrations for Pb, As, and Sb had to be reduced by a factor of ten (Saunders et al., 2010).

After plotting all the data onto the diagram, two end-member compositions were found, one of which is the Ag-selenide dominated ores like the ones found at Midas and the other is the Au-telluride ores of Colorado (Saunders et al., 2010). Saunders et al. (2010) concluded that the variations in end-member composition could be attributed to differing magmatic systems, and therefore magmas hold more influence on the ore geochemistry than the host rocks.

Lead isotope studies have also become a significant analytical method in determining ore genesis as it is a common ore metal found in trace levels within native

gold and gold-bearing alloys like electrum (Saunders et al., 2010). Kamenov et al. (2007) found that Pb-isotope traces alloyed with native Au and electrum are similar to basalts erupted from the initial emergence of the Yellowstone hotpot/mantle plume. Hanan et al. (2008) additionally found that Pb-isotope signatures of the Miocene-age basalts and Columbia River basalt lava flows are fairly consistent with an inferred mantle plume origin. The similar isotopic signatures for Pb alloyed with Au in epithermal deposits in Nevada to basalts of the inferred mantle plume seem to imply that the Yellowstone plume was the source of the precious metals deposits (Hames et al., 2009).

Fluid inclusion studies aid in the understanding of the conditions under which a vein formed, but inclusions are difficult to observe within epithermal deposits (personal communication, James Saunders, 2010). White (1985) conducted the first actual fluid inclusion study of Midas and found a temperature range of 175-200°C, but his data is considered unreliable as the source data is not available. Goldstrand and Schmidt (2000) found a formation temperature of 240°C with low salinities and a suggested neutral pH for the fluids.

Simpson and Mauk (2001) wrote an unpublished Newmont report on a study in which twelve vein samples, consisting of massive colloform banded quartz and quartz breccias, were analyzed for fluid inclusions. Originally, there were nineteen samples, but due to a lack of primary inclusions, the sample number was reduced to the twelve that displayed the best secondary inclusions (Simpson and Mauk, 2001). They found a homogenization temperature range from 199-266°C and concluded an average temperature of 227°C with low salinities (Simpson and Mauk, 2001).

The most recent fluid inclusion study done on Midas deposits was conducted by Matt Riederer (2007). He implemented the classification scheme developed by Roedder (1984) to group fluid inclusions into primary, psuedosecondary, and secondary categories using primary inclusions whenever possible and psuedosecondary inclusions where primary inclusions were absent (Riederer, 2007). Riederer (2007) found an ore precipitating homogenization temperature range between 190-260°C with freezing temperatures between -1.0 to 0°C, which is consistent with what Simpson and Mauk (2001) determined, and concluded homogenization and final ice-melt temperatures at Midas are analogous to most epithermal ore deposits.

4. METHODOLOGY

FIELD WORK

Field work was conducted over the summer of 2011 under the direction and supervision of Newmont Mining Corporation through a summer internship at the Midas Mine Operations located three miles from the town of Midas, Nevada. The basic goal of the internship was to provide a broad range of experience in all the geological aspects of the mining industry while also gathering the necessary data and information to write this thesis. Initial work at the mine consisted of becoming familiar with the geology of the district. This was done by logging exploration core and spending a week underground working ore control.

One exploration drill hole had been drilled and produced a 200 ft. core with a direct intercept of the Ace vein (Fig. 10). A week was spent in the Midas core shed testing the core to determine rock strength, overall length of core recovered, and logging the core in detail. Pucks were taken from various levels within the actual vein and sent off for density analysis (Fig. 10). The remainder vein in the core was cut into additional pucks to produce thin sections for geochemical and mineralogical studies.



Figure 10. Photograph of MUC-02054 exploration core from Ace (9052) vein.

Underground samples were collected from two actively mined headings of the Gold Crown vein: 6N5130 and 6S5530. The only area where the eastern veins are exposed in the mine currently is an exploration drift at the 4800 level. The 4-4800 drift intercepted two of the five eastern veins: GP and Ace. Samples were acquired from two accesses intercepting the Ace vein and from two exposures of the GP vein (Fig. 11) in the exploration drift.



Figure 11. Photograph of hand specimen RACGP017 44800E of GP (905) vein taken from 4-4800 on 7-18-11.

Fourteen of these drill piercings had multi-element analysis (ICP-MS) results completed by ALS Minerals. The remaining drill piercings were reviewed and fifteen additional samples were selected for multi-element analysis based on assay values. Coarse rejects of the original core from the selected drill piercings was requested from the storage facility in Carlin, NV. Newmont Mining sent the samples off to ALS Minerals for multi-element analysis by ICP-MS. The assay techniques are described below.

GEOCHEMISTRY

There are multiple assay techniques that can be employed with rock samples. Newmont Mining's primary assay technique is the fire assay process. The fire assay technique is the most effective for gold samples as it can withstand larger sample sizes than other techniques, which is crucial since elemental gold will only occur in low levels and therefore requires a good pre-concentration step (SGS, 2010). This technique has great extraction capabilities and low detection limits as small as 5ppb Au (SGS, 2010). There are multiple steps that must be conducted to make the fire assay technique work: fluxing, fusion, cupellation, and gravimetric finish. In the flux step the proper levels of acidic, basic, oxidizing, and reducing reagents must be maintained for fusion step to work properly, and together this assemblage of reagents is called a slag. In Ag analysis, an inquart (milligrams of silver) is mixed into the slag to make the Ag: Au ratio 3:1 so that the Ag will dissolve and leave the Au behind (SGS, 2010).

The fusion step involves using the proper slag to fuse with the sample matrix to form another slag that will dissolve away the base metals and a 30 g Pb button (SGS, 2010). The now fused sample is poured into crucible and placed in a fire assay furnace at 900°C. In the furnace the fusion process begins to breakdown the sample matrix and releases the precious metals, and is done in conditions to ensure that elemental Pb is reduced in the litharge (SGS, 2010). The now reduced Pb will combine with the precious metals and settle to the bottom of the crucible, and after about an hour, the melt is poured into a conical mold (SGS, 2010).

The cupellation step involves separating the Pb from the precious metals by means of rapid oxidation of elemental Pb into PbO in a cupel at 840°C (SGS, 2010). The

Pb will absorb into the cupel leaving the precious metals on the surface as a prill (small spherical globe), and this prill is used in the final step of the fire assay technique (SGS, 2010). The prill is composed of in part Ag and Au alloy (SGS, 2010)

There are several options for a finishing process, but the one most commonly used by Newmont Mining is the gravimetric finish. In this step, the prill is removed from the cupel, cleaned, and flattened with a hammer and anvil. For Ag analysis, the prill is weighed, and then for Au analysis, the prill is treated with hot, diluted nitric acid that will dissolve the Ag and leave the Au behind (parting) (SGS, 2010). The Au is then washed, annealed, cooled, and weighed.

After initial assaying, the remaining core not tested (collectively termed “coarse rejects” by mining companies) was collected from selected drill-holes and were sent to ALS labs to conduct multi-element analysis using Inductively Coupled Plasma – Mass Spectrometry (ICP-MS) and Inductively Coupled Plasma – Atomic Emission Spectroscopy (ICP-AES). A 0.5g prepared sample is digested with aqua regia in a graphite heating block and the solution is diluted with deionized water and mixed and analyzed (ALS labs ME-MS41 Analytical Method, 2011). Following ICP-AES the solution is reviewed for Bi, Hg, Mo, W, and Ag and diluted as necessary and then analyzed with ICP-MS for the remaining elements with analytical results corrected for inter-element spectral interferences (ALS labs ME-MS41 Analytical Method, 2011). Elements that are of interest to this study include: Au, Ag, As, Sb, Hg, Tl, Cu, Pb, Zn, Mo, Ba, Se, Te, S, Fe, Mg, P, Sr, V, Al, Ca, K, and Na.

ORE PETROGRAPHY

Standard polished thin sections and polished thick sections were made to conduct SEM analyses. A selection of five billets from the GP vein and five billets from the Ace vein were sent to Vancouver Geotech labs to be made into standard polished thin sections while a selection of nine samples from the GP vein and nine samples from the Ace vein were made into polished thick sections at the Auburn University Fluid Inclusions Lab in the Department of Geology and Geography.

SEM analysis was conducted at the Wilmore Laboratories materials characterization facility of the Materials Engineering Department at Auburn University under the direction of Dr. Bart Prorak. Samples were observed in back-scatter mode to choose sites for spot EDAX semi-quantitative analysis of all Ag minerals to see what minerals are present, how much Se, Au, Ag, and electrum there is in the eastern veins, and if the fluorite present is late stage.

5. RESULTS

GEOCHEMISTRY

Analyses by ICP-MS were conducted for the following elements (ppm) from the selected coarse rejects of the Midas eastern veins: Ag, As, Sb, Hg, Tl, Cu, Pb, Zn, Mo, Ba, Bi, Cd, Ni, Se, Te, W, Cr, Co, S, Fe, Mg, Mn, P, Sr, U, V, Ce, Cs, Nb, Re, Rb, Be, B, Ga, Ge, La, Sc, Al, Ca, K, Na, Ti, Hf, In, Li, Sn, Ta, Th, Y, Zr, and Au. A correlation matrix was generated for a subset of these elements that were detected in all the samples. The elements used for the correlation matrix include: As, Sb, Hg, Tl, Cu, Pb, Zn, Mo, Ba, Se, Te, S, Fe, Mg, P, V, Al, Ca, K, Na, Ag, and Au. The correlation matrix below (Table 3) shows how each element correlates to another, with strong positive correlations highlighted in yellow and strong negative correlations highlighted in blue. Any correlation above 0.5 is considered to have a strongly positive correlation and anything lower than -0.5 is considered as having a strongly negative statistical correlation.

The strongest positive correlations were between Tl:K, P:V, Mg:V, Mg:P, Fe:V, Fe:P, Fe:Mg and Ag:Se. The strong Ag:Se correlation would indicate the significant presence of Ag-selenide minerals within the eastern veins (Fig. 12). Silver also strongly correlates with Pb, which is consistent with the ore petrography studies conducted, and indicates the presence of galena occurring with the Ag-minerals. Notably, Au did not correlate strongly with any elements. An overall Ag:Au ratio was calculated from the averages of the ppm values of Ag and Au and yielded a ratio of 176:1 (see Appendix I for ICP-MS data and ratio calculation).

Table 3. ICP-MS correlation matrix of selected elements from coarse rejects of eastern veins.

	As	Sb	Hg	Tl	Cu	Pb	Zn	Mo	Ba	Se	Te	S	Fe	Mg	P	Sr	V	Al	Ca	K	Na	Ag	Au	
As	1																							
Sb	0.588496	1																						
Hg	-0.14997	0.198481	1																					
Tl	0.14014	0.254425	0.334039	1																				
Cu	-0.04687	-0.11051	-0.04243	-0.31696	1																			
Pb	0.128565	0.101655	-0.0305	-0.11696	0.752711	1																		
Zn	-0.02585	0.010931	-0.14498	-0.35131	0.8635	0.737304	1																	
Mo	0.268271	0.417876	0.049445	0.2626	-0.21417	0.043718	-0.11007	1																
Ba	0.106099	0.153194	0.062591	0.717729	-0.27345	-0.06567	-0.23995	0.430592	1															
Se	-0.18277	0.030547	-0.00395	0.158838	0.388622	0.534066	0.416464	0.006046	0.062837	1														
Te	-0.1804	-0.07329	0.119845	-0.21926	0.279453	0.059098	0.105529	-0.23235	-0.28522	0.346235	1													
S	0.76399	0.628193	-0.07238	0.134213	-0.15035	-0.13975	-0.0959	0.23089	0.001677	-0.14296	0.006103	1												
Fe	0.072438	-0.14258	-0.21131	-0.53591	0.477494	0.203765	0.504617	-0.29221	-0.4016	-0.31977	-0.09113	-0.06903	1											
Mg	-0.09996	-0.31309	-0.18321	-0.54301	0.48167	0.260026	0.521701	-0.40157	-0.39755	-0.26968	-0.08319	-0.29528	0.95488	1										
P	-0.07221	-0.28249	-0.19345	-0.54135	0.523256	0.234833	0.496717	-0.44449	-0.41421	-0.26003	0.002872	-0.25365	0.963718	0.976559	1									
Sr	0.074796	0.049251	0.068569	0.235734	-0.08035	-0.00739	-0.1013	0.071026	0.195105	-0.01492	-0.06532	0.170118	-0.11043	-0.13401	-0.12223	1								
V	-0.1619	-0.28865	-0.17603	-0.51237	0.527997	0.250504	0.500797	-0.4126	-0.35756	-0.20988	-0.00106	-0.32692	0.945214	0.966063	0.982208	-0.1174	1							
Al	0.028306	-0.05585	-0.05297	0.376051	0.12557	0.045171	0.106945	-0.10281	0.445398	-0.15356	-0.28779	-0.13672	0.345339	0.378534	0.387764	0.18975	0.407904	1						
Ca	-0.31583	-0.0666	0.142472	0.351538	-0.24533	-0.1696	-0.29443	-0.12261	0.275345	0.330903	0.356853	-0.18942	-0.59197	-0.48887	-0.45875	0.242225	-0.42167	0.062966	1					
K	0.0115	0.099053	0.20356	0.942999	-0.2662	-0.10318	-0.28631	0.16755	0.758919	0.247144	-0.20349	0.001687	-0.47988	-0.45567	-0.45191	0.312617	-0.40294	0.503924	0.497809	1				
Na	0.172605	0.13862	-0.04419	0.429534	-0.22037	-0.18298	-0.23227	0.177965	0.625184	-0.11727	-0.17399	0.162457	-0.2059	-0.23268	-0.20742	0.235806	-0.1773	0.592612	0.508738	0.567997	1			
Ag	-0.0385	0.167691	-0.01334	0.135274	0.324187	0.585395	0.303274	0.084946	0.069593	0.906028	0.385158	-0.09459	-0.27516	-0.25194	-0.2249	-0.01634	-0.181	-0.19645	0.280461	0.177567	-0.17639	1		
Au	0.380045	0.12231	-0.06405	-0.02903	-0.03448	0.060177	-0.04051	-0.0493	-0.14539	0.032727	-0.05572	0.407252	0.060632	-0.05489	0.014214	0.015891	-0.08513	-0.18046	-0.20656	-0.08272	-0.21565	0.129155	1	

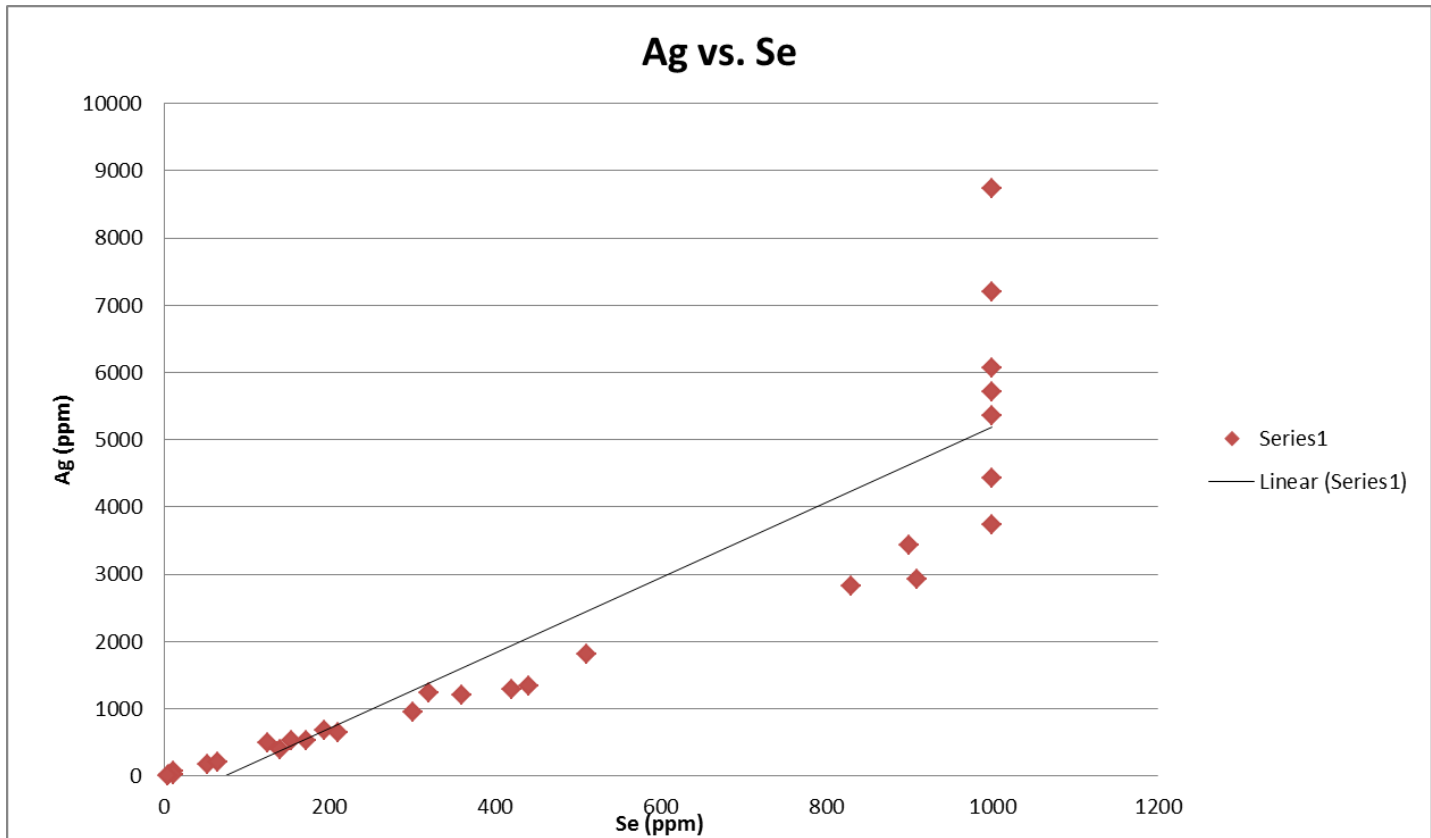


Figure 12. Scatter plot with trendline showing the correlation between Ag and Se.

EASTERN VEINS STRUCTURAL INTERPRETATION

Initial longitudinal sections of the foot wall (FW) geology at the intersection of the vein suggest there are north east-trending faults cutting through the eastern vein area. These faults displace the felsic and mafic units as horst and graben structures, which are observed in the district on a large-scale. Larger north eastern-trending faults locally called the NOW (Northern Owyhee) and SOW (Southern Owyhee) do show post mineralization movement, which offsets the Colorado Grande vein and its subsidiary veins (pers. commun., Mike Robinson and Gabriel Graf of Newmont Mining, 2012).

Additional longitudinal sections depicting the gold equivalents and true thickness of the veins were generated in order to determine if there was a relationship between vein thickness and ore grade and if there was any particular preferred lithology for mineralization of Au and Ag. Overall, higher-grade mineralization has been found to be restricted to an elevation range of 4,300-4,900 ft. regardless of rock type (Figs.13 through 21).

In the Charger Hill vein longitudinal sections, there appears to be preferential mineralization occurring within the Elko Prince Formation and the mafics sills (Figs. 13 and 14). The NOW appears to only affect high-grade locations by offsetting the Elko Prince layers so this Owyhee fault is suggested to be younger than the mineralization event (Figs. 13 and 14). There also does not appear to be any distinctive correlation between vein thickness and ore grade (Figs. 14 and 15). It is possible that the pre-mineral northeastern faults could act as conduits for the hydrothermal fluids.

In the GP vein, the fault structures have an effect on the locations of mineralization indicating that the smaller north-east trending faults were already there

prior to mineralization. Like the Charger Hill vein, mineralization appears to be preferentially enriched in the Elko Prince Formation and the mafics sills (Figs. 16 and 17). Also, like Charger Hill, there is no distinctive correlation between vein thickness and ore grade (Figs. 17 and 18). The long section of the Au equivalents and true thickness show that high-grade material occurs in varying thicknesses and this was also observed in the underground exploration drift. The Ace vein has high-grade occurrences like Charger Hill and GP and is affected by the faults and still occurs within the Elko Prince Formation and mafics sills (Figs. 19 and 20). There is also no apparent relationship between vein thickness and ore grade (Figs. 20 and 21). The Charger Hill and GP vein also intersect the Ace vein which could have an effect on the overall mineralization and any pre-mineral northeastern faults could also act as conduits for hydrothermal fluids affecting the locations of mineralization.

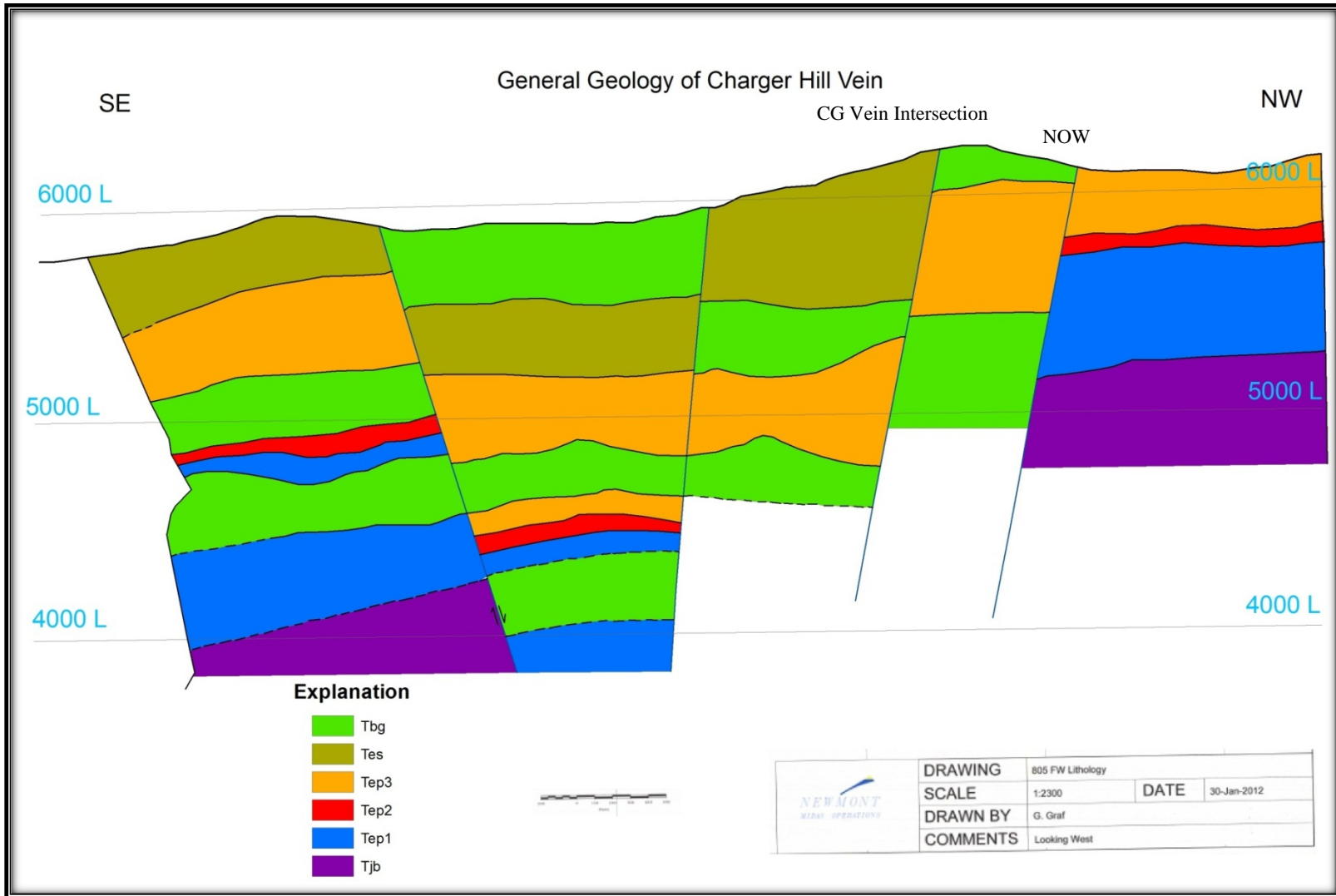


Figure 13. Longitudinal section of the Charger Hill FW showing varying lithologies along the vein (modified from Gabriel Graf, Midas Mine Geology Department, 2012).

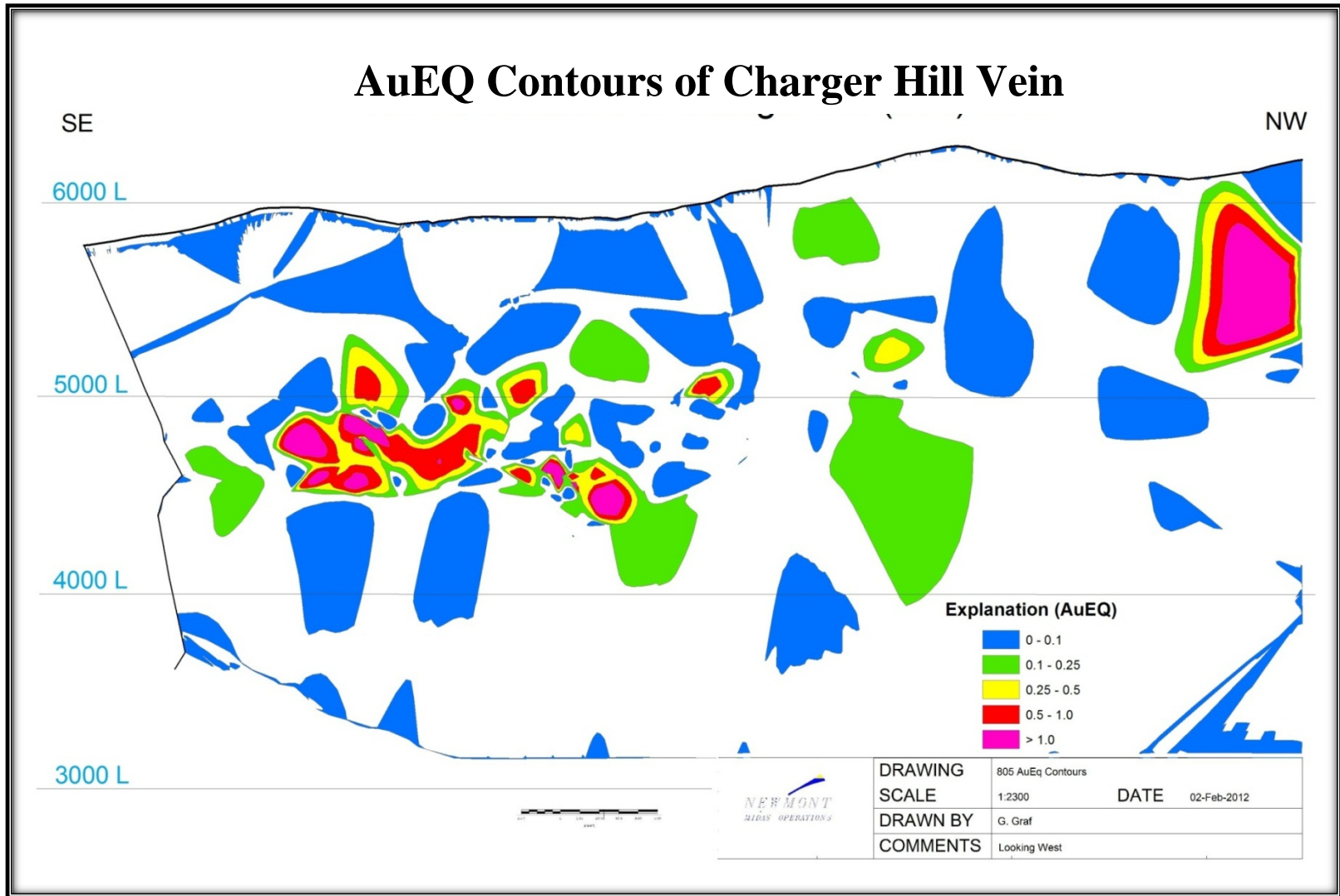


Figure 14. Longitudinal section of the Charger Hill vein showing Au equivalents (AuEQ) along the vein (modified from Gabriel Graf, Midas Mine Geology Department, 2012).

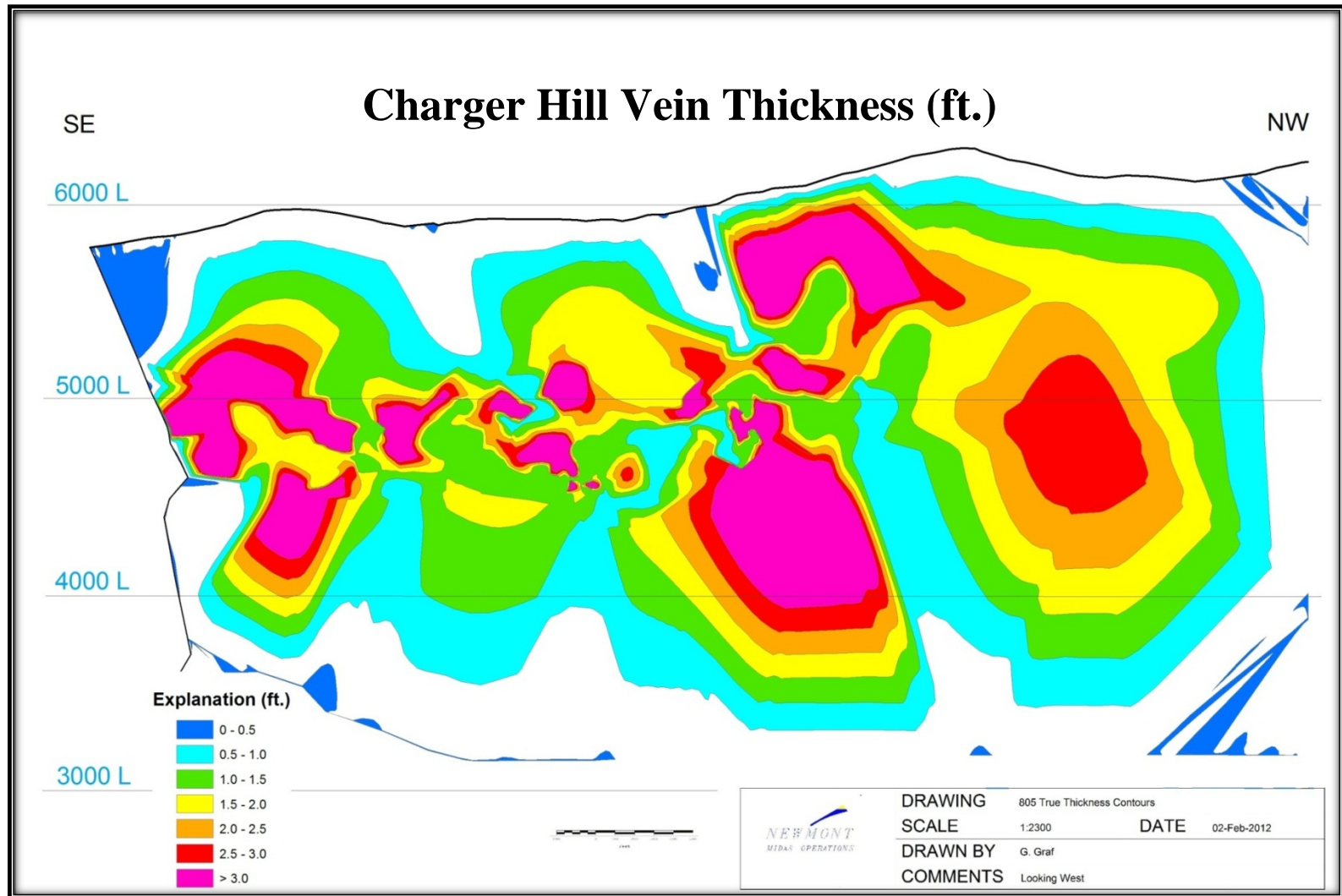


Figure 15. Longitudinal section of the Charger Hill vein showing the true thickness of the vein (modified from Gabriel Graf, Midas Mine Geology Department, 2012).

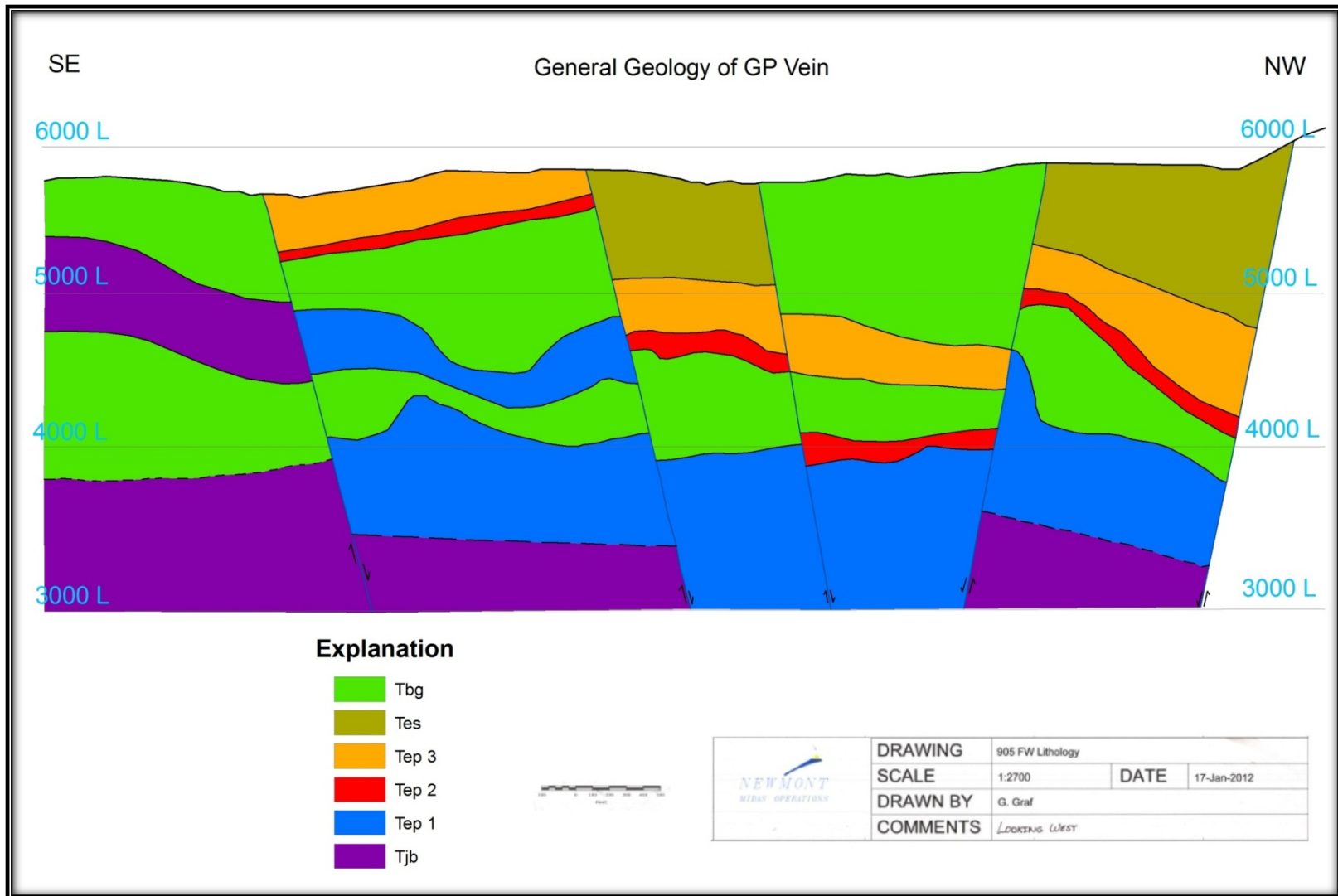


Figure 16. Longitudinal section of the GP FW showing varying lithologies along the vein (modified from Gabriel Graf, Midas Mine Geology Department, 2012).

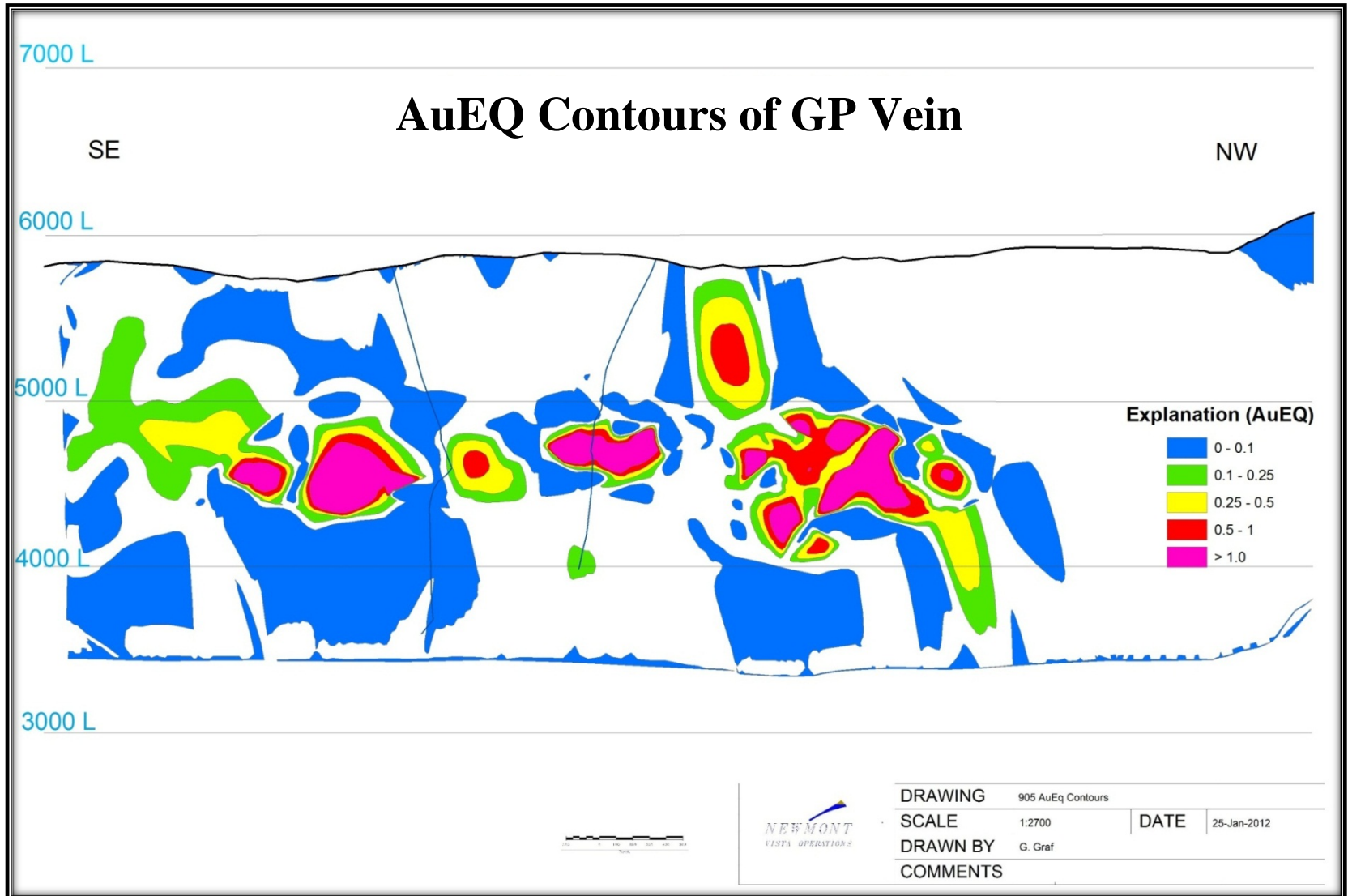


Figure 17. Longitudinal section of the GP vein showing Au equivalents (AuEQ) along the vein (modified from Gabriel Graf, Midas Mine Geology Department, 2012).

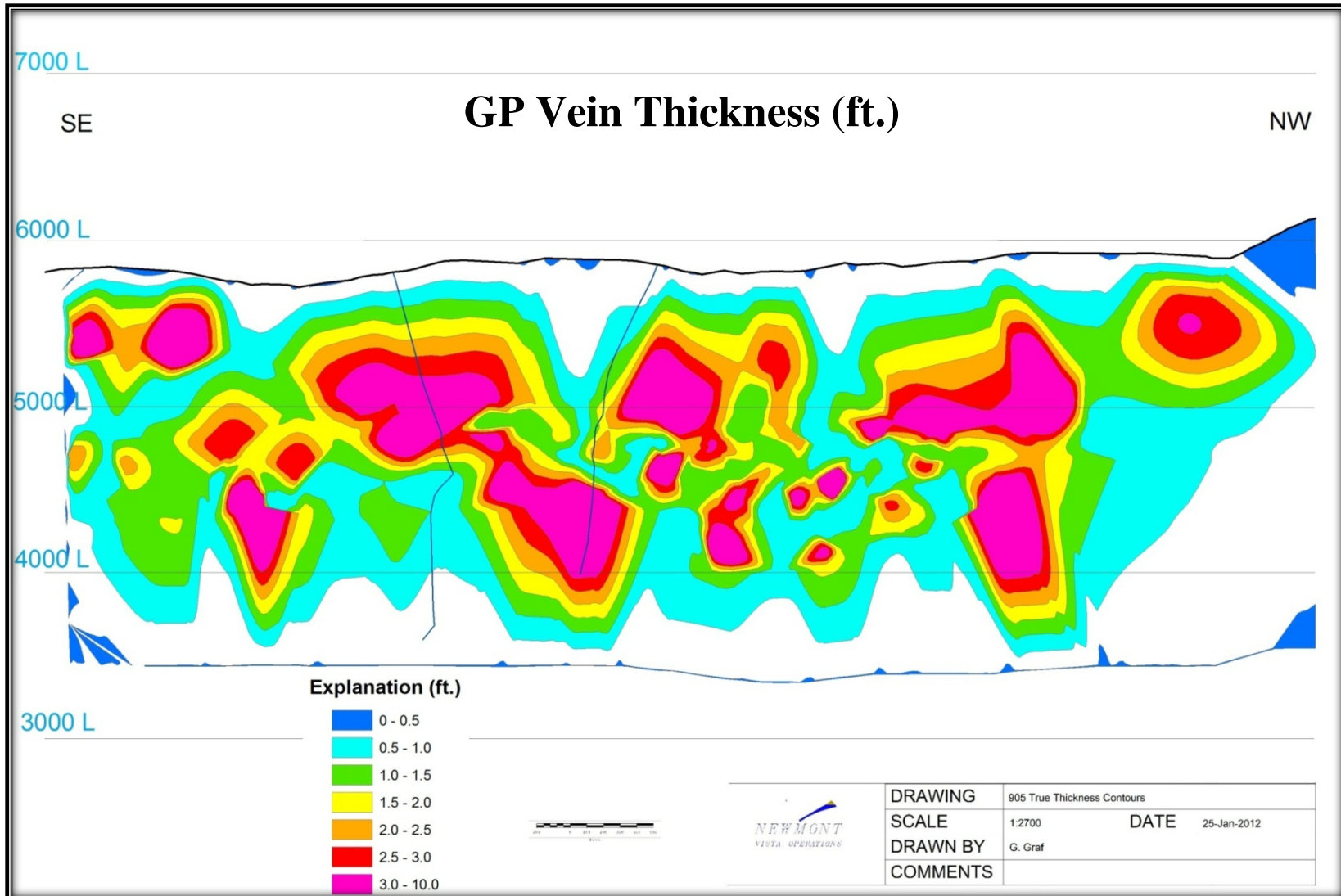


Figure 18. Longitudinal section of the GP vein showing the true thickness of the vein (modified from Gabriel Graf, Midas Mine Geology Department, 2012).

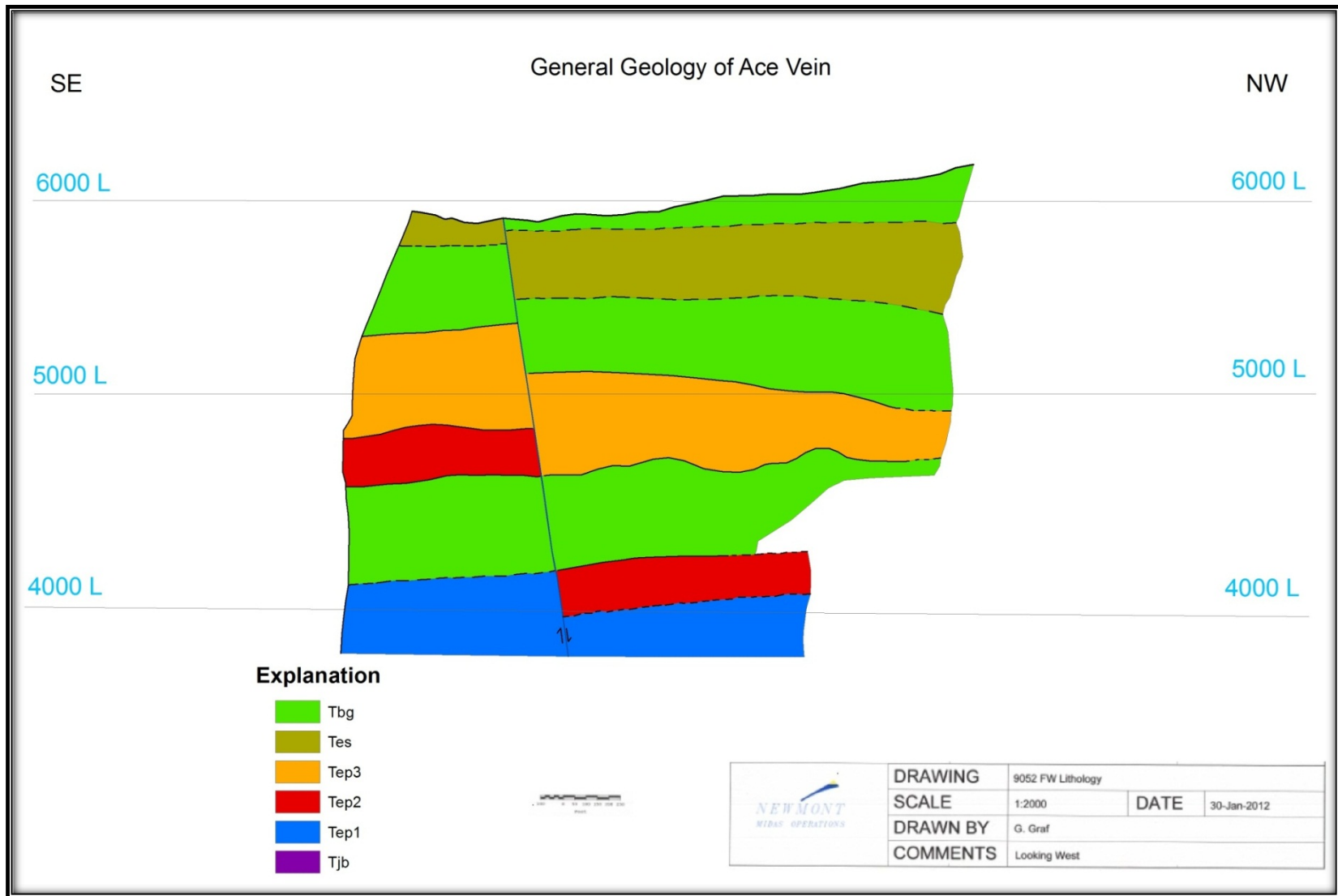


Figure 19. Longitudinal section of the Ace vein FW showing varying lithologies along the vein (modified from Gabriel Graf, Midas Mine Geology Department, 2012).

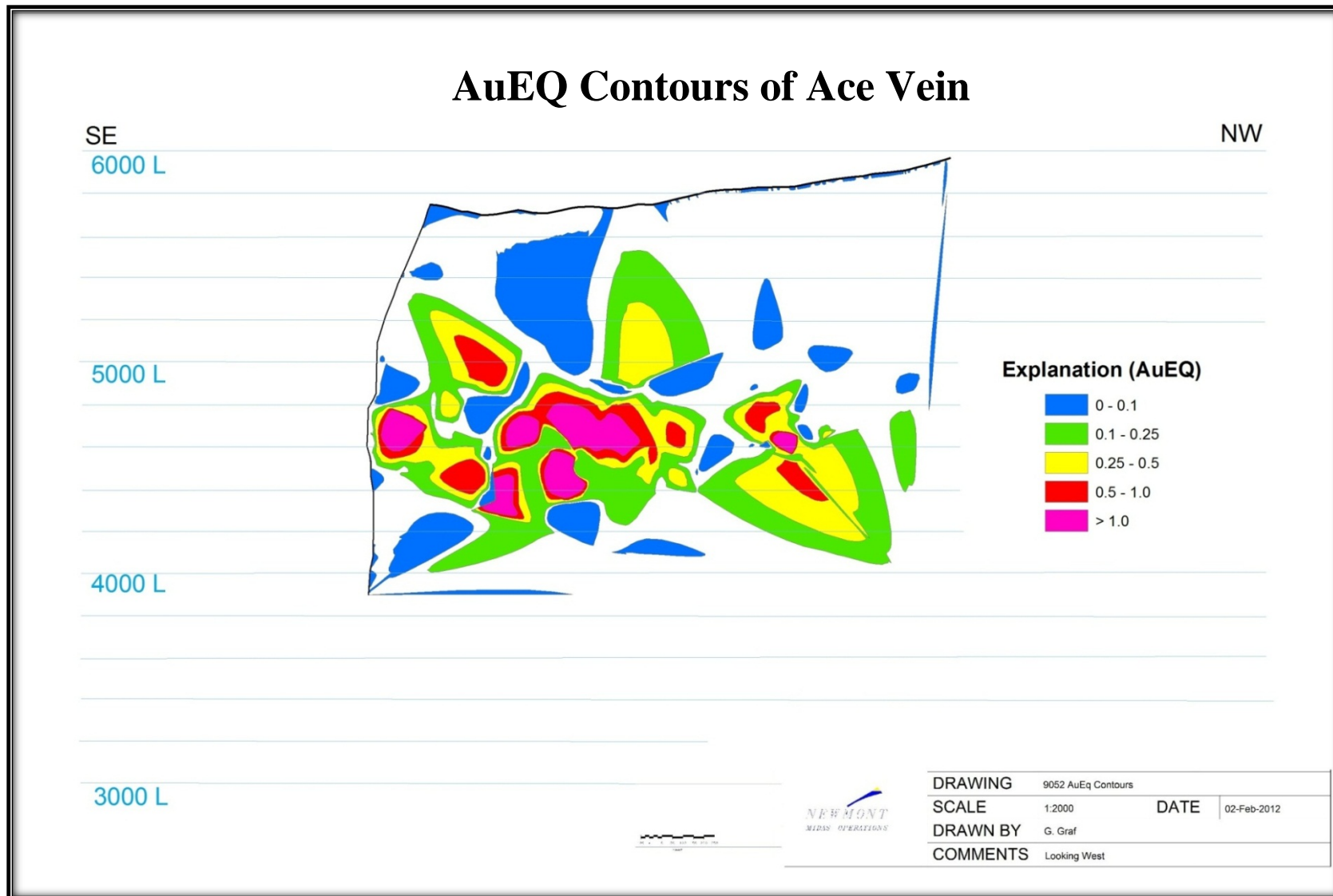


Figure 20. Longitudinal section of the Ace vein showing Au equivalents (AuEQ) along the vein (modified from Gabriel Graf, Midas Mine Geology Department, 2012).

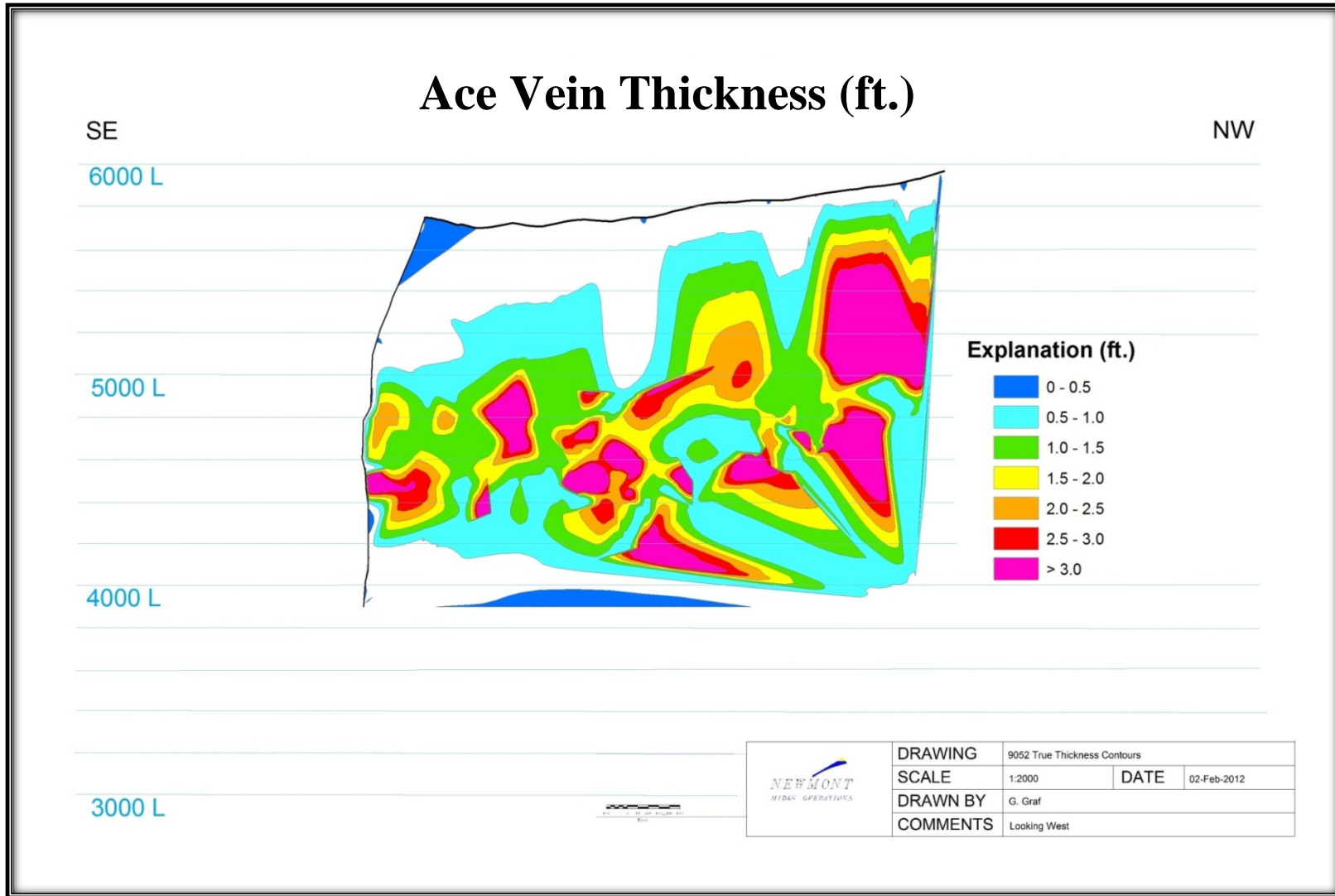


Figure 21. Longitudinal section of the Ace vein showing the true thickness of the vein (modified from Gabriel Graf, Midas Mine Geology Department, 2012).

ORE PETROGRAPHY

Basic ore petrography was conducted to obtain a representative sample of the mineralogy of the eastern veins. Samples from the GP vein were collected from an exploration drift at the 4800 level, while samples from the Ace vein were collected from a 200 ft. exploration drill-hole core.

Gangue minerals in the GP vein are typical epithermal types (quartz \pm adularia \pm calcite), but additionally contain an extensive amount of fluorite (CaF_2). About 90% of the metallic minerals consist of pyrite (FeS_2) with sphalerite (ZnS) surrounding the pyrite and inclusions of the Ag-minerals aguilarite (Ag_4SeS), acanthite (Ag_2S), and naumannite (Ag_2Se) within the pyrite (Figs. 22 and 23).

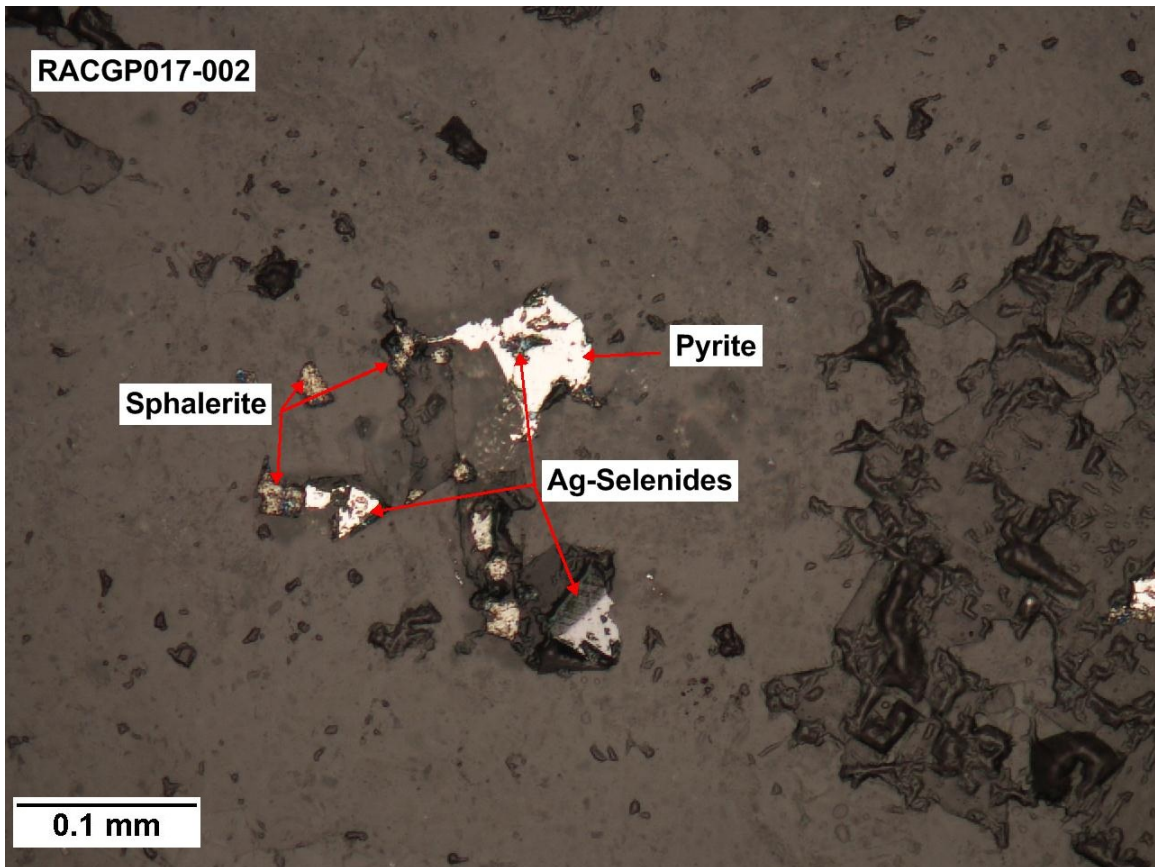


Figure 22. Photomicrograph of sample RACGP017-002 showing pyrite associated with Ag-selenide minerals and sphalerite predominately occurring around the rims of the pyrite (reflected light).

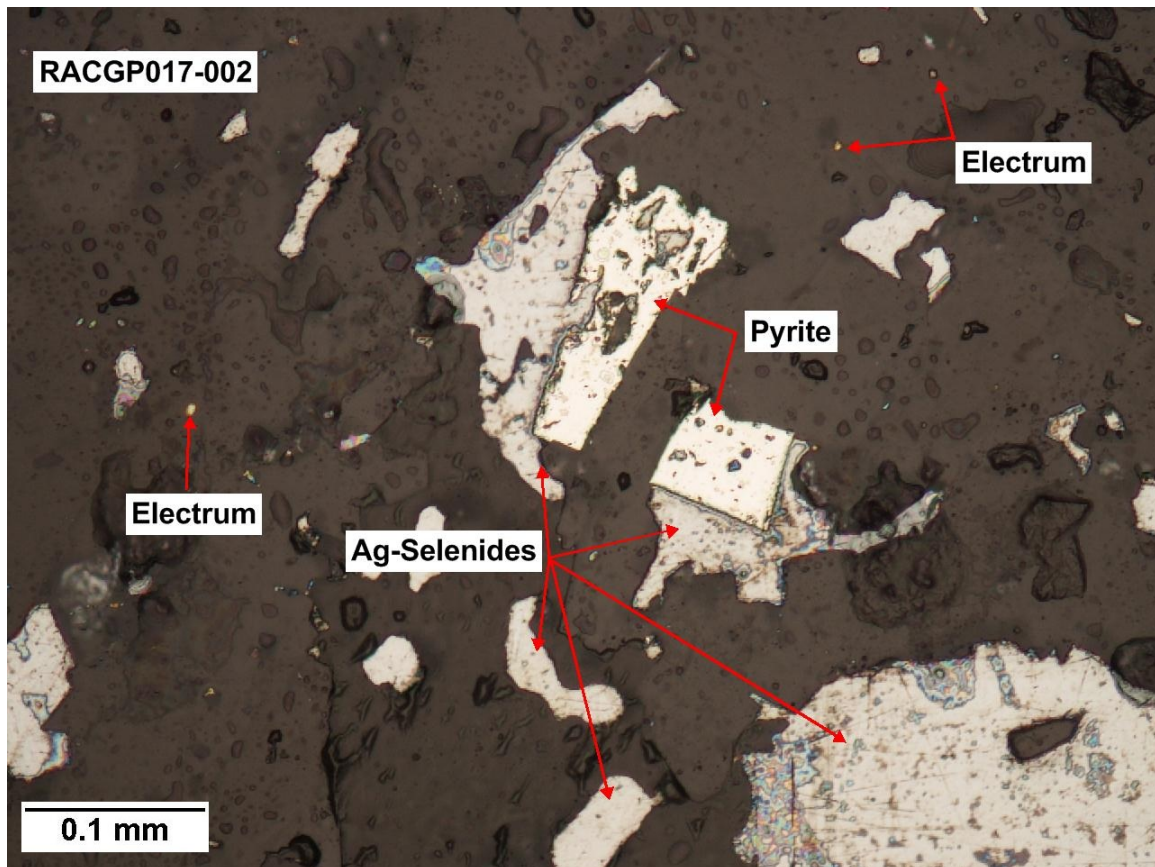


Figure 23. Photomicrograph of sample RACGP017-002 showing additional pyrite association with Ag-selenide minerals and tiny electrum grains (reflected light).

However, not all Ag-mineral grains are associated with pyrite. Chalcopyrite (CuFeS_2) and tiny grains of electrum are also associated within Ag-minerals (Fig. 24), which is similar to the epithermal deposits in Hishikari, Japan (Izawa et al., 1990). The electrum does not associate directly with pyrite indicating possible co-precipitation with isolated mineral precipitation. The overall abundance of electrum in the GP vein appears to be significantly lower relative to the main production veins at Midas based on SEM analysis and ore petrography. The dominant Ag-minerals within the eastern veins are the silver selenides aguilarite and naumannite.

Fluorite appears in distinct triangular shapes that behave isotropically under the crossed-polar transmitted light and is intermixed with the quartz and adularia grains, indicating co-precipitation of the fluorite \pm quartz \pm adularia rather than late-stage cross-

cutting veinlets. There is also an abundance of quartz and submicroscopic white mica crystals. The mica crystals are most likely sericite since it is colorless in plane polarized light. Tiny adularia crystals are also displayed as psuedorhomboidal shapes and behave like quartz in extinction. The presence of both sericite and adularia crystals indicated that the pH of the sample is around 6 indicating that the fluids were right at the phase boundary between the two minerals. The overall paragenetic sequence of the eastern veins is very similar to the main production veins of Midas with the exception of the fluorite mineralization, which occurs as late-stage in the main production veins (Goldstrand and Schmidt, 2000).

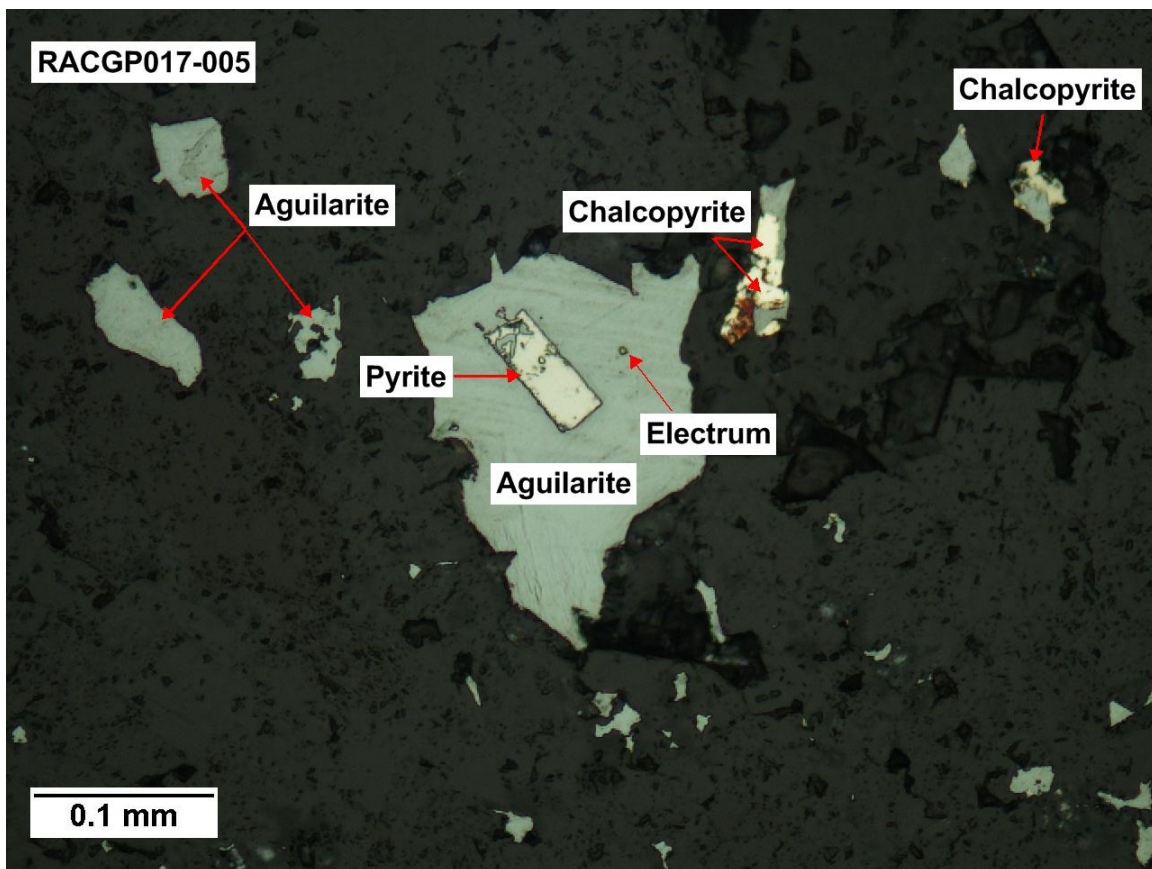


Figure 24. Photomicrograph of sample RACGP017-005 showing encrustation of pyrite within the Ag-selenide, aguilareite, and electrum and chalcopryite also associated with the aguilareite (reflected light).

The dominant quartz texture present is jig-saw (Fig. 25) visible from the cluster of interpenetrating grain boundaries (Moncada et al., 2011). The jig-saw texture indicates recrystallization occurred at temperatures greater than 180° C (Fournier, 1985; Saunders, 1994). There is also an abundance of bladed (platy) calcite and bladed quartz pseudomorphs (Fig. 25). In some samples, the bladed calcite is more prominent than in others. The presence of bladed calcite indicates that it was not late-stage and originated from hydrothermal boiling, which is a prominent epithermal deposition mechanism. The presence of quartz pseudomorphs indicates that boiling is located in close proximity to metal deposition margins (Simmons and Christenson, 1994).

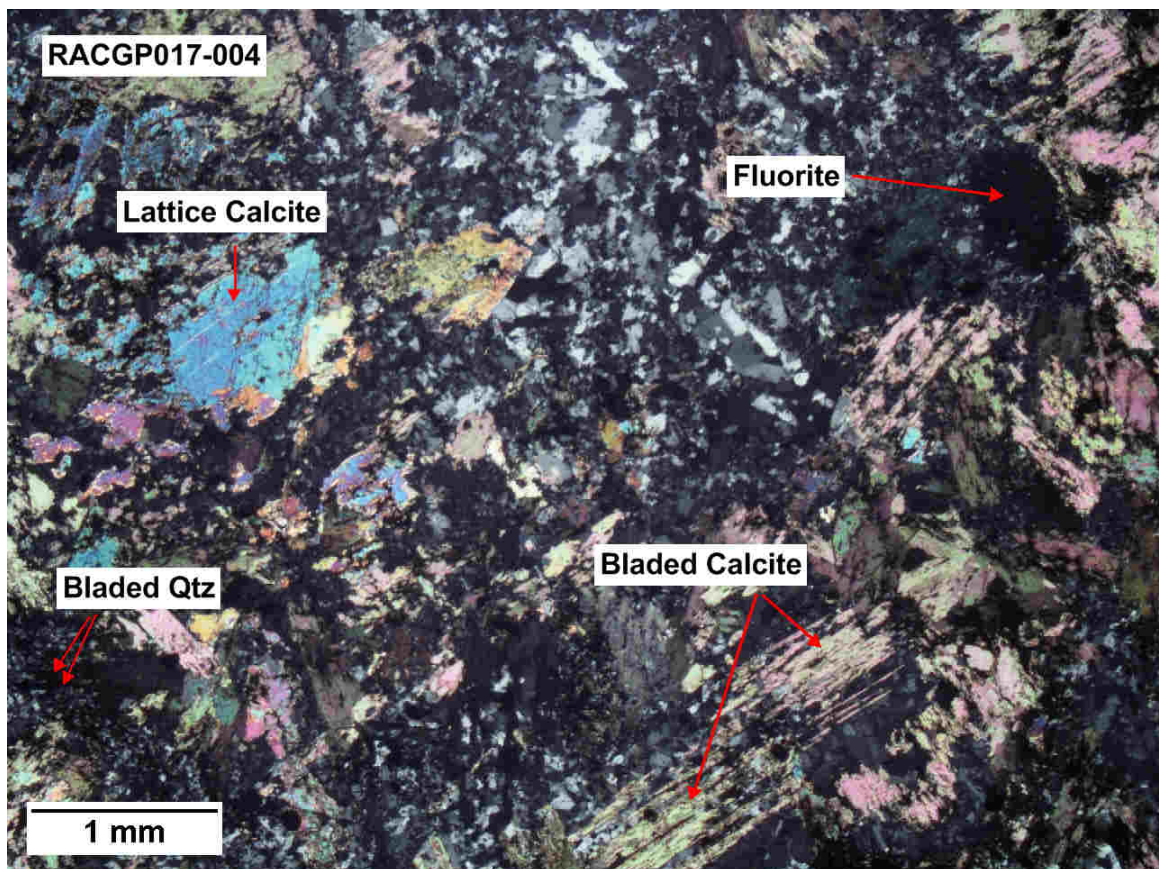


Figure 25. Photomicrograph of sample RACGP017-004 showing gangue minerals and textures. Fluorite appears isotropic. Bladed calcite and quartz indicate hydrothermal boiling had occurred (transmitted light, crossed polars).

Gangue minerals in the Ace vein consist of quartz \pm calcite \pm adularia \pm fluorite similar to the GP vein. However, fluorite is more coarse-grained in Ace than in the GP. In a couple of the samples fluorite occurs in tiny veinlets with small calcite crystal inclusions within the fluorite. This indicates late-stage deposition of the fluorite relative to the other gangue minerals. However, several samples from the Ace vein have a large percentage of fluorite intermixed with lattice calcite or bladed calcite (Fig. 26). This could indicate late-stage mineralization of fluorite as opposed to the co-precipitation of fluorite with the gangue minerals in the GP vein.

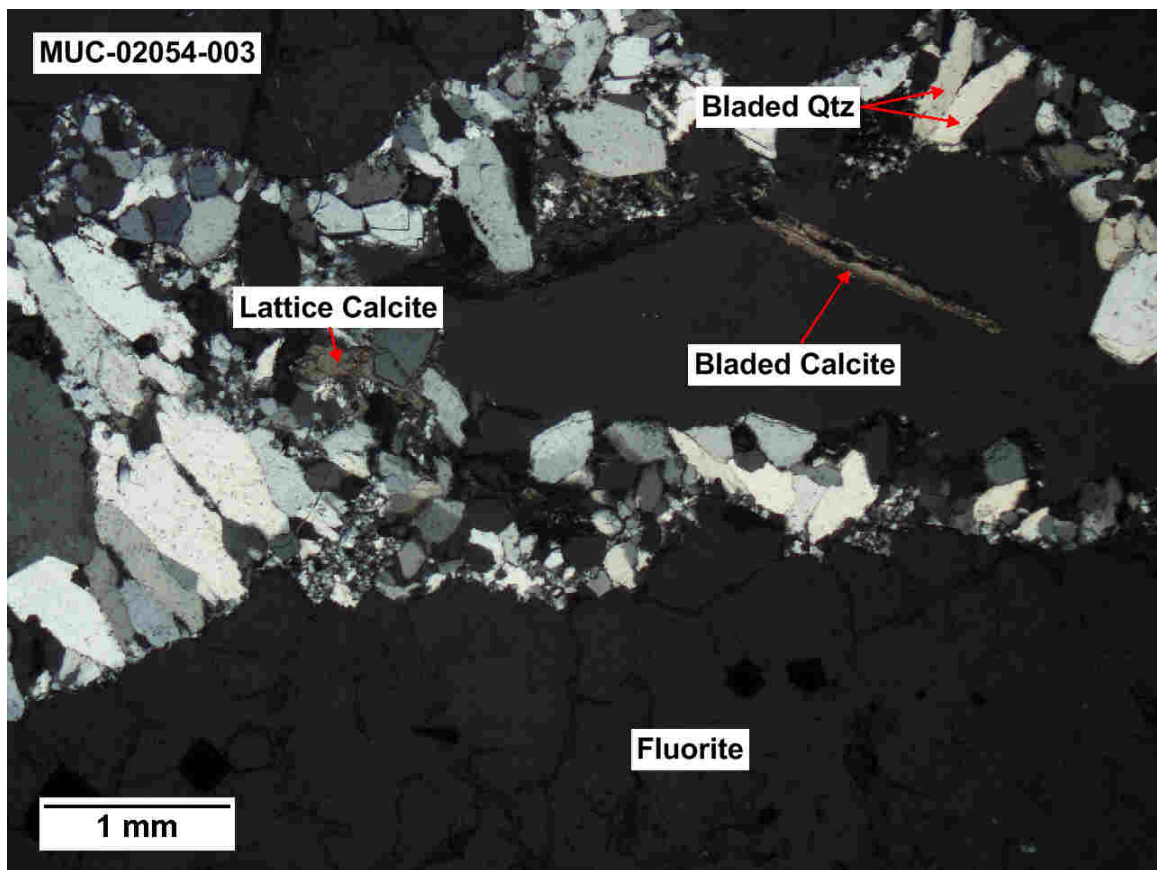


Figure 26. Photomicrograph of sample MUC-02054-003 showing overall texture of 9052 vein with quartz, lattice calcite, bladed quartz, and bladed calcite occurring in tiny veinlets surrounded by massive fluorite (transmitted light, crossed polars).

Adularia grains occur as psuedorhombhedrons and fluid inclusions can be seen that do not contain vapor bubbles. Furthermore, there were no observed fluid inclusions in fluorite that would be suitable for microthermometric analysis. Quartz occurs in veinlets exhibiting jig-saw and colloform texture (chalcedony) (Fig. 27). This texture likely resulted from the recrystallization of chalcedony (Camprubi and Albinson, 2007; Dong et al., 1995). The textures present in these samples are very similar to textures seen in the Veta Madre epithermal systems of the Guanajuato Mining District in Mexico (Moncada et al., 2011). Quartz psuedomorphs are present in tiny, bladed crystals as well as bladed calcite indicating more hydrothermal boiling. Lattice calcite is also observed, which is more common within the main production veins at Midas.

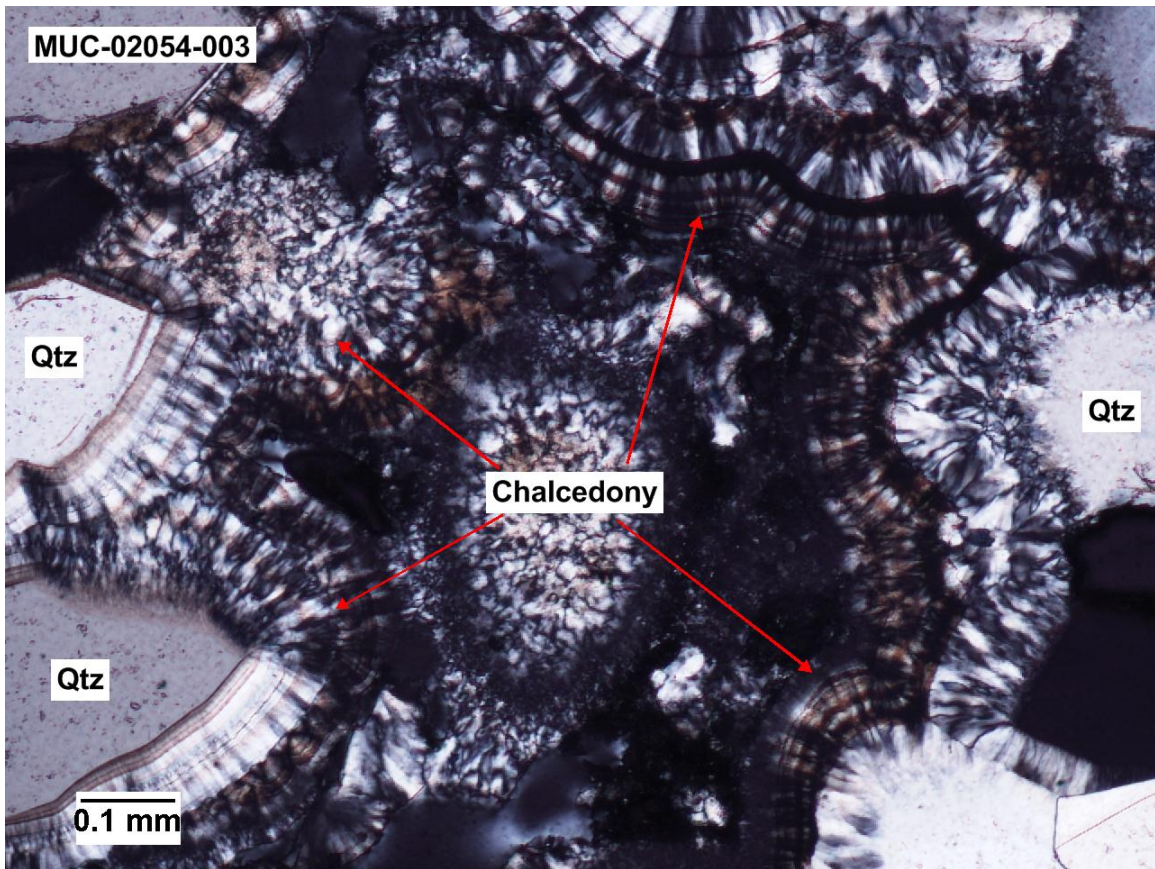


Figure 27. Photomicrograph of sample MUC-02054-003 showing the colloform texture of chalcedony occurring around the grain boundaries of the quartz grains (transmitted light, crossed polars).

Metallic minerals consist of mostly pyrite mixed with chalcopyrite and Ag-minerals aguilarite and naumannite (Fig. 28). Sphalerite and fine-grained galena is also seen within these samples (Fig. 29). The Ag-minerals occur with chalcopyrite and pyrite (Fig. 30). Some grains display crustiform texture with a Ag-mineral encrusted around pyrite.

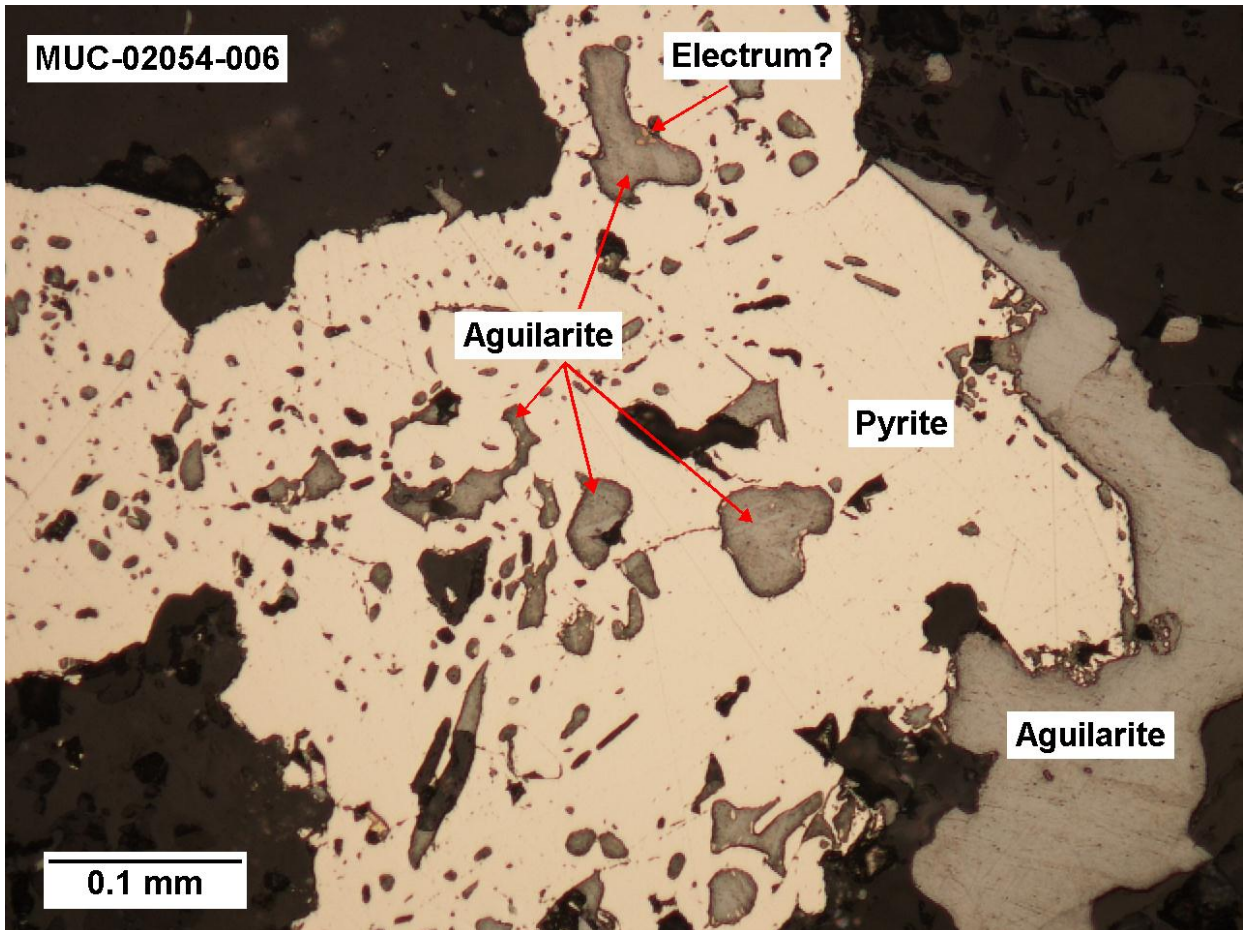


Figure 28. Photomicrograph of sample MUC-02054-006 showing pyrite “diseased” with aguilarite and a possible electrum grain (reflected light).

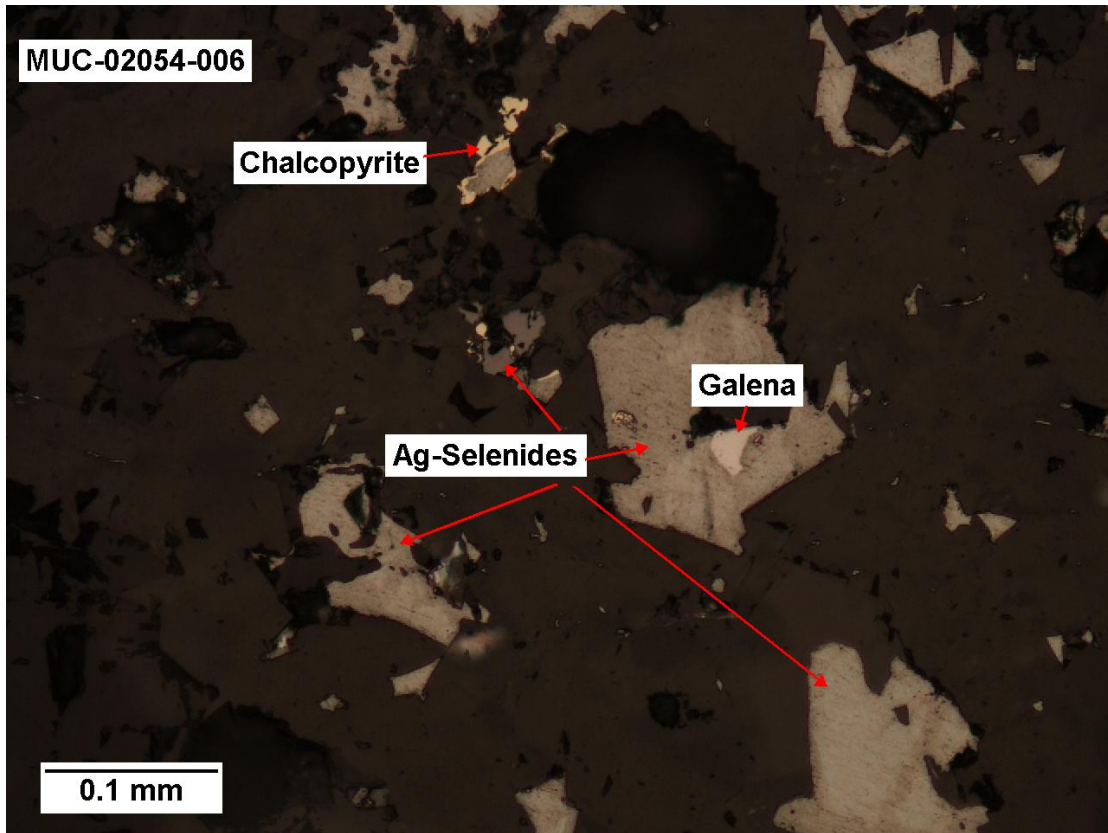


Figure 29. Photomicrograph of sample MUC-02054-002 with aguilarite and chalcopyrite and galena (reflected light).

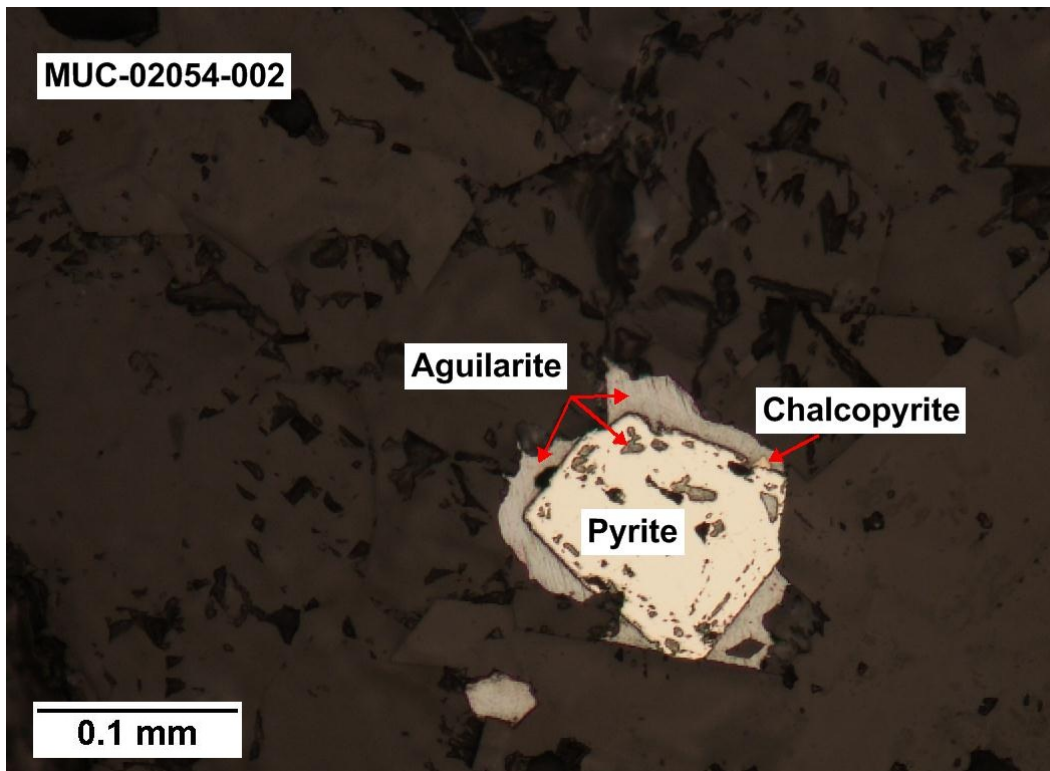


Figure 30. Photomicrograph of sample MUC-02054-002 illustrating encrustation of pyrite by aguilarite and chalcopyrite within the aguilarite (reflected light).

SEM-EDAX characterization of the GP and Ace veins confirms what was observed in the thin section samples. A polished thick section made from the RACGP017 hand sample was used in classifying the Ag-minerals for the GP vein; while the polished thin section sample MUC-02054-004 was used for characterizing the Ace vein. Most Ag-mineral percentages indicate a range of atomic percentages between 60-70% Ag, 20-30% Se, and 10-20% S (Fig. 31). Naumannite, aguilarite, and acanthite were plotted on the ternary diagram to see where the Ag-minerals of the eastern veins plotted. Based on the SEM results, an aguilarite-naumannite solid solution appears to be the dominant Ag-mineral since the main cluster of data points plot between aguilarite and naumannite (Fig. 31).

Electrum was found in the Ace vein samples in association with the Ag-minerals. Only three instances of pure native gold were found with one occurring in the GP sample and the other two occurring within the Ace vein. Also, it can be noted that in a few areas where electrum occurs, there are also tiny grains of pure lead. The occurrence of pure Au and native Pb is rare in nature and suggests a possible minor supergene event (pers. commun., James Saunders, 2012). Electrum grains also contain a higher atomic percentage of Au than Ag, but there were a few electrum grains where the atomic percentage of Ag was greater than Au. Semi-quantitative SEM-EDAX analyses at Auburn were compared to precise electron microprobe analyses at the University of Georgia and results were similar. Selected photos and atomic weight percentages are presented in Appendix 3. Based on the ore petrography observations and SEM characterization, a suggested paragenetic sequence for the eastern veins is presented in Figure 32 below.

Ternary Diagram of Ag-Selenide Minerals

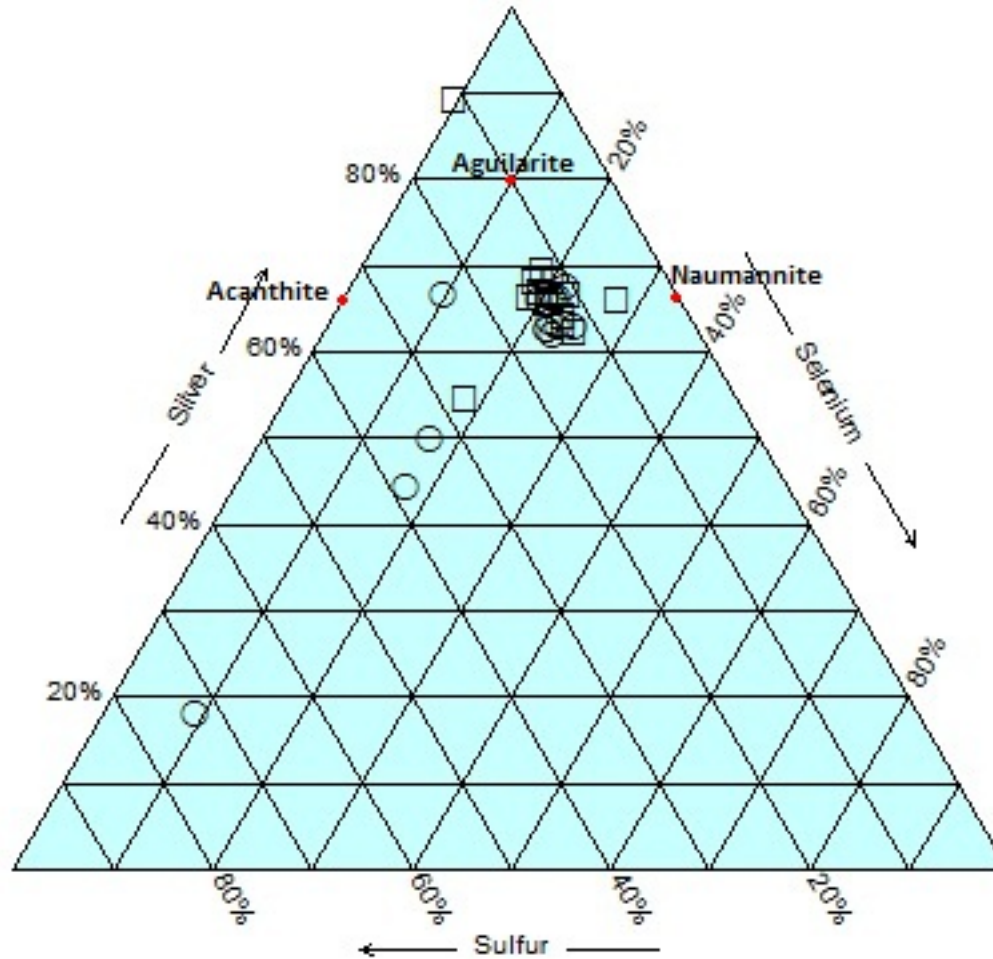


Figure 31. Ternary diagram of atomic percentages of Ag vs. Se vs. S. Ace vein samples are marked with a hollow circle and GP vein samples are marked with a hollow square.

Minerals	Wall Rock Alteration	Veins		Post-mineralization
		Early	"Main"	
Pyrite	—————	—————	—————	
Chlorite	—————			
Epidote	—— — —			
Chalcopyrite	—————	——	—————	
Biotite	—————			
Quartz	—— — —	—— — —	—————	
Calcite	—————	—————	—————	—————
Adularia		—————	—————	
Galena		—————		
Sphalerite		—————		——
Electrum		—— — — — —		
Naumannite		—————		
Aguilarite		—————		
Acanthite		—————		
Fluorite		—————	—————	——

Figure 32. Suggested paragenetic sequence for the GP and Ace veins of Midas.

6. DISCUSSION

Geochemical results indicate many strong correlations between select elements, but the correlation that is of greatest interest is the strong connection of Ag:Se (Fig. 12). The results of this study and previous studies on the eastern veins confirm a high percentage of Ag-selenide minerals present along with the sulfides pyrite, chalcopyrite, and sphalerite. Gold has no significant correlation to any element (Table 3). The silica textures suggest the fluids were at a temperature of $\leq 250^{\circ}\text{C}$ when the base metals precipitated (Saunders, 1994). Electrum occurrences are significantly rarer in comparison to the main production veins like Colorado Grande and Gold Crown at Midas based on the samples that were collected, but the electrum grains contained a higher atomic percentage of Au than Ag and occurred with naumannite. Goldstrand and Schmidt (2000) also confirmed electrum's close spatial association with naumannite occurring in the Colorado Grande and Gold Crown veins using petrographic and SEM analysis.

Ag:Au-grade zonation long sections appear to show an overall trend of mineralization occurring in the Elko Prince Formation and mafics unit (Figs. 13, 14, 16, 17, 19, 20). Higher-grade mineralization tends to also occur along the same elevation indicating some type of elevational control on precious metal precipitation. The smaller north east-trending faults are pre-mineralization as there is no offset of mineralization surrounding these structures (Figs. 13, 16, 19). It is likely that these smaller faults and vein intersections may have provided areas of increased fluid flow and potential locations for deposition.

Petrographic and SEM-EDAX analysis confirms that Au is rare relative to the main production veins and occurs as electrum in these veins (Figs. 23 and 24). The presence of bladed calcite and bladed quartz textures is attributed to hydrothermal fluid boiling (Figs. 26 and 27), which is a normal mechanism in epithermal vein genesis (Simmons and Christenson, 1994). Also, the presence of colloform texture around quartz grains (chalcedony) indicates a possible recrystallization period of amorphous silica (Saunders, 1994; Dong et al., 1995; Camprubi and Albinson, 2007). The dominant mineral species within the eastern veins are base metals and Ag-selenides. The overall paragenetic sequence of the veins indicates that the Ag-selenides are the same age as the sulfides due to the fact that the Ag-selenides appear to have embayed the pyrite (Figs. 28 and 32). In addition there are several areas where there is encrustation of the sulfides by the Ag-selenides (Fig. 30) generally indicating co-precipitation of precious metals and base metals.

The presence of high Se in the Midas eastern veins can be attributed to a large-scale abundance of Se-rich ores within the western parts of the northern Great Basin and more specifically, the northern Nevada Rift. Selenium is geochemically volatile, and during the Laramide subduction event, partial melting of mantle material coupled with magma generation and magma degassing lead to a mobilization of volatile elements and compounds including selenium (Hedenquist and Lowenstern, 1994; Heinrich et al., 1999; Saunders et al., 2008; Richards, 2009; Saunders and Brueske, 2012). Electrum grains in the studied eastern vein are rare and only occur within Ag-selenide grains at the microscopic level. Only one grain of pure gold was found within the Ace vein sample MUC-02054-004, but it was in association with the Ag-selenide minerals.

Based on the petrographic, SEM-EDAX, and ICP-MAS evidence found in this study, the eastern veins appear to be a distal product of the same large-scale magmatic-hydrothermal event that formed the main production veins. The Ag:Au ratio in the Colorado Grande vein is roughly 12:1 whereas the eastern veins' Ag:Au ratio is roughly 176:1 based on average ppm values of Au vs. Ag. The likely reason why this ratio of Ag:Au is severely skewed in the eastern veins apparently is not so much that the eastern veins are Ag-rich, but that the eastern veins are Au-deficient (refer to Appendix 3 for additional SEM data). The reason for the Au-deficiency in the eastern veins likely is a result of the dynamics of hydrothermal fluid transport. Similar trends have been observed in other areas of the northern Great Basin like the DeLamar mine in Silver City, Idaho, which also shows a trend of decreasing Au and an increase in the Ag:Au ratio from 4:1 to 10:1 (Marek, 1991). The only difference in this Au-decreasing trend in DeLamar versus the Au-decreasing trend in the Midas eastern veins is that the concentration of Au in the DeLamar system decreases from east to west versus the Midas trend of Au decreasing from west to east (Marek, 1991). Other districts in the northern Great Basin that show this Au-decreasing trend include Sleeper and Buckskin National in Nevada. The details of hydrodynamic transport of precious metal nanoparticles or colloids is beyond the scope of this thesis but obviously warrants additional research.

The apparent source of Au in ore-forming fluids has been attributed to basaltic magmas from the bimodal assemblage common in the northern Great Basin. Detailed geochemical analyses demonstrated rhyolitic magmas were not a likely source as previously thought because their Au-content is so low (Noble et al., 1988; Connors et al., 1993). The basaltic magmas provided the Au by either degassing the magmas, as

proposed by Heinrich et al. (1999) and Saunders et al. (2008), or leaching of Au-rich basalts by ore-forming solutions proposed by Noble et al. (1988). In more recent years, the discovery of a distinct Pb-isotope signature of electrum led to the conclusion that Au originated from a more “primitive” magma (Kamenov et al., 2007). Ascending plumes of magma can stall at a shallow depth and the heat produced from that stalled magma will initiate crustal melting, which produces the rhyolitic portion of the bimodal volcanism in the region, helping also to drive the hydrothermal circulation of meteoric water (Kamenov et al., 2007). Hydrothermal circulation continues as episodic pulses of magmatic volatiles apparently contributed Au to the shallow, meteoric water-dominated geothermal system (Kamenov et al., 2007). Hydrothermal fluid transport depends on several factors to include the overall chemical makeup of the fluid and minerals contained within the fluid, hydrothermal alteration assemblages, and aqueous solubilities (Seward and Barnes, 1997).

Metal transport in hydrothermal systems can be classified under the theory of electron donor-acceptor of hard and soft Lewis acids and bases (Pearson, 1963; Ahrlund, 1968; Parr and Pearson, 1983). This electron donor-acceptor theory states that hard metals will form stable complexes with hard ligands with the metals acting as the acceptors and the ligands acting as the electron donors. Soft metals like Au and Ag will do the exact opposite and form stable complexes with soft donors, but also will easily dislocate electrons of energy and a large number of electrons in the outer shell (Seward and Barnes, 1997). The complexes formed between soft metals and soft donors is characteristically covalent and increases in electronegativity as the two approach each other. The soft metals tend to combine with halide ions, but in the case of epithermal

systems, HS^- is the key constituent in the hydrothermal fluids that attaches to Ag^+ to form a stable hydrosulfide complex (Seward and Barnes, 1997). Sulfide mineral precipitation in hydrothermal fluids will involve a reduction of aqueous sulfate to sulfide, which combines with metals like Au and Ag during cooling periods where metal complexes will destabilize and then attach to the stabilized hydrosulfide (Reed and Palandri, 2006).

Hydrothermal fluid chemistry of Au:Ag ore-forming systems is characterized by the formation of two hydrosulfide complexes: $\text{AuHS}^0 / (\text{AgHS}^0)$ and $\text{Au}(\text{HS})_2^- / (\text{Ag}(\text{HS})_2^-)$ (Seward and Barnes, 1997). These two complexes along with the cyanide complex $\text{Au}(\text{CN})_2^-$ are among the most stable complexes and several orders of magnitude more stable than the chloride complex $\text{Au}(\text{Cl})_2^-$ (Seward, 1991). As stated before, the HS^- complex is the primary constituent for Au:Ag transport within low sulfidation epithermal systems, especially in systems at low salinity and near neutral pH, which is true of the eastern veins at Midas. It is also important to note that the Au and Ag in the ore zones are both dissolved in ore-forming solutions and electrum and silver-selenides are transported in this hydrothermal fluid as either nanoparticles or colloids. The sluice-box textures present in several samples of the Ace and GP vein are indicative of electrum and naumannite occurring as colloids. It is suggested here that these nanoparticles nucleated from Au-rich ore-forming solutions deep below the “epithermal” environment and were transported upward by the solutions.

The Colorado Grande, Gold Crown, Gold Crown HW, Discovery, and Snow White veins all exhibit higher concentrations of Au than in the eastern veins as described previously. This is due perhaps to the density differences between Au and Ag colloids that might have formed deeper, therefore enabling Au the ability to travel only so far

from its magmatic source. Density differences between native Ag and Au are drastic with Ag at 10.5 g/cm^3 and Au at 19.3 g/cm^3 . Since Au is far denser than Ag, it is likely the pulse from the magmatic fluid would not carry heavier Au particles very far from its source, which would be the main production veins. The density of electrum ranges from $12.5\text{-}15.5 \text{ g/cm}^3$ while Ag-minerals like naumannite, aguilarite, and acanthite range from $6.5\text{-}8 \text{ g/cm}^3$, $7.4\text{-}7.56 \text{ g/cm}^3$, and $7.2\text{-}7.4 \text{ g/cm}^3$ respectively, indicating a preference for the transport of Ag-mineral particles over Au particles and an explanation for what appears to be a lop-sided Ag:Au ratio present in the eastern veins relative to the main production veins in the Midas district.

Saunders (1990, 1994) demonstrated that gold and AgSeS colloids would have a negative surface charge and that for the particles to stick and aggregate, the surface charge repulsion must be overcome. This could be done two ways in the “boiling zone” at Midas: 1) electrum particles growing larger, thus increasing their momentum; and 2) increased velocity of particles as they enter the boiling zone. Electrum nanoparticles should have a higher sticking efficiency because of their metallic bonding capabilities, as opposed to nanoparticles having Se and S in them, thus, Ag-S-Se particles are less dense, have lower sticking efficiency, and move up and out away from the Au-rich parts of the veins. So both the chemical and physical transport and deposition mechanisms are important in forming the Midas-Sleeper-Hishikari-type colloid aggregation ore mineral textures.

In comparison to the main production veins in the Midas district, Leavitt (2004) indicated that the presence of chlorite and calcite in fractures and veinlets suggested lateral fluid flow. As the hydrothermal system developed H_2S -bearing fluids in

conjunction with water and rock associations, it resulted in observed moderate to strong propylitic alteration (Leavitt, 2004), which in the MUC-02054 core occurred throughout the 200 ft. sample. The pathfinder element Ag would move through hydrothermal fluids as a bisulfide complex and deposited with sulfur. This, along with the increase in Zn levels reflects the presence of these sulfide complexes (Henley and Hedenquist, 1986). Silicic alteration observed in the eastern veins and the main production veins formed during a cooling period of fluids rich in silica and ascended along fractures and faults moving laterally across bedding (Leavitt, 2004). Leavitt (2004) compared the Midas district to a hot-spring system where there is an increase in pathfinder element Hg, As, and Sb and a decrease in Au:Ag with abundant silica above ore zones towards the paleosurface (Silberman and Berger, 1985). Leavitt's (2004) characterization of the Midas district overall agrees with the general interpretation here of how the eastern veins formed with the exception of the added component proposed here that physical transport of Au and Ag phases also played an important role in Au to Ag ratios.

7. CONCLUSIONS

- ❖ Overall, the mineralogy of the eastern veins is similar to the main production veins with the exception of the large percentage of fluorite present in the eastern veins.
- ❖ Geochemical analysis indicates that there is a strong correlation between Ag and Se indicating the presence of Ag-selenide minerals in great abundance.
- ❖ Silica textures and fluid inclusions petrography indicate base metal precipitation occurred at $\leq 250^{\circ}\text{C}$, in keeping with earlier more detailed fluid inclusion studies done on Midas veins.
- ❖ Electrum occurs in significantly lower quantity in the eastern veins than it does in the Colorado Grande and its subsidiary veins. Atomic percentages are higher in Au than Ag in electrum grains.
- ❖ The sulfides and Ag-selenides occur in close spatial association. The sulfides are thought to be older than the Ag-selenides based on encrustation and diseased textures observed within the sulfide minerals. There are a few select areas where the opposite occurs suggesting co-precipitation of base and precious metals.
- ❖ Longitudinal sections indicate mineralization in the Ace, GP, and Charger Hill veins occurs within the Elko Prince Formation and mafics sills.
- ❖ High-grade mineralization tends to be restricted to an elevation range of 4,300-4,900 ft. indicating a type of elevation control on precious metal precipitation or the elevation where boiling occurs.

- ❖ One of the primary Owyhee fault structures, NOW, occurred after mineralization while the smaller north eastern-trending fault structures occurred prior to mineralization. This indicates that Owyhee fault structures have an apparent effect on the location of precious metal precipitation.
- ❖ Petrographic analyses found bladed calcite and quartz pseudomorphs that indicate hydrothermal boiling, and the presence of colloform textures indicates the recrystallization of amorphous silica.
- ❖ The paragenetic sequence is approximately the same as the Colorado Grande with the exception of the co-precipitation of the base and precious metals and the large percentage of fluorite present in the eastern veins.
- ❖ Geochronology studies on the eastern veins to date have not been obtained. Adularia samples were too finely grained and intermixed with quartz, adularia, and fluorite making age dating very difficult.
- ❖ The disparate nature of the Ag:Au ratios in the central and eastern veins is attributed to the eastern veins being Au-poor rather than Ag-rich based on the low quantity of electrum found relative to the main production veins.
- ❖ The low quantity of Au appears to be the result of hydrothermal fluid transport dynamics, colloidal/nanoparticle transport, and the higher density of Au vs Ag implying that Au particles would not travel very far from the source.
- ❖ Based on the geochemistry, mineralogy, and geochronology studies conducted, the eastern veins appear to be a distal product of the magmatic event that created the Colorado Grande vein and its subsidiary veins.

REFERENCES

Abbot, M.B., and Wolfe, A.P., 2003, Intensive pre-Incan metallurgy recorded by lake sediments from the Bolivian Andes: *Science*, v. 301, p. 1893-1895.

Arhland, S., 1968, Thermodynamics of complex formation between hard and soft acceptors and donors: *Structure and Bonding*, v. 5, p. 118-149.

Blair, K.R., 1991, Geology of the Gold Circle district, Elko County, Nevada: Unpublished M.S. thesis, University of Arizona, Tucson, p. 1-85.

Brueseke, M.E., Heizler, M.T., Hart, W.K., Mertzman, S.A., 2007, Distribution and geochronology of Oregon Plateau (U.S.A.) flood basalt volcanism: The Steens Basalt revisited: *Journal of Volcanology and Geothermal Research*, v. 161, p. 187-214.

Brueseke, M.E., 2010, Magmatism and mineralization in the Oregon Plateau and northern Great Basin: Mid-Miocene volcanism and associated bonanza ore deposits and their relations to the inception of the Yellowstone hotspot: Geological Society of Nevada 2010 Symposium: Great Basin Evolution and Metallogeny, Reno, NV, May 2010, p. 247-255.

Camprubí, A., Albinson, T., 2007, Epithermal deposits in Mexico – update of current knowledge, and an empirical reclassification: Geological Society of America Special Paper 422, p. 377-415.

Casteel, M.V., Schmidt, K., Goldstrand, P., Bernard, J., Sandberg, J., 1999, Geological setting of the Ken Snyder gold and silver mine, Elko County, Nevada, in Kizis, J.A., Jr., ed., 1999 Spring Field Trip Guidebook, Low-sulphidation gold deposits in northern Nevada: Geological Society of Nevada Special Publication no. 29, p. 213-220.

Cleverly, J.S., 1997, A Geological and Mineralogical Investigation of a Selenium rich, Volcanic Hosted, Epithermal Gold-Silver deposit, The Midas District, Nevada: Unpublished M.Sc. thesis, University of Leicester, p. 1-98.

Connors, K.A., Noble, D.C., Bussey, S.D., Weiss, S.I., 1993, Initial gold contents of silicic volcanic rocks: Bearing on the behavior of gold in magmatic systems: *Geology*, v. 21, p. 937-940.

Dong, G., Morrison, G., Jaireth, S., 1995, Quartz textures in epithermal veins, Queensland; classification, origin and implication: *Economic Geology*, v. 90, no. 6, p. 1841-1856.

Dalrymple, G.B., Alexander, E.C., Lanphere, M.A., and Kraker, G.P., 1981, Irradiation of samples for $^{40}\text{Ar}/^{39}\text{Ar}$ dating using the Geological Survey TRIGA Reactor: USGS Professional Paper 1176, p. 1-55.

Dickinson, W.R., 2006, Geotectonic evolution of the Great Basin: *Geosphere*, v. 2, no. 7, p. 353-368.

Fournier, R.O., 1985, The behavior of silica in hydrothermal solutions: Reviews in *Economic Geology*, v. 2, p. 45-61.

Gammons, C.H., and Barnes, H.L., 1989, The solubility of Ag_2S in near-neutral aqueous sulfide solutions at 25 to 300°C: *Geochim. Cosmochim. Acta* 53, p. 279-290.

Goldstrand, P.M., and Schmidt, K.W., 2000, Geology, Mineralization, and Ore Controls at the Ken Snyder Gold-Silver Mine, Elko County, Nevada: *Geology and Ore Deposits 2000: The Great Basin and Beyond Proceedings*, v. 1, p. 265-287.

Goldstrand, P., 2001, Midas ICP-MS Biogeochemical Survey: Midas JV, internal report, p. 1-5.

Hames, W., Unger, D., Saunders, J., Kamenov, G., 2009, Early Yellowstone hotspot magmatism and gold metallogeny: *Journal of Volcanology and Geothermal Research*, v. 188, p. 214-224.

Hanan, B.B., Shervais, J.W., Vetter, S.K., 2008, Yellowstone plume-continental lithosphere interaction beneath Snake River Plain: *Geology*, v. 36, p. 51-54.

Heald, P., Foley, N. K., Hayba, D.O., 1987, Comparative anatomy of volcanic-hosted epithermal deposits: acid-sulfate and adularia-sericite types: *Economic Geology*, v. 82, p. 1-26.

Henley, R.W., and Hedenquist, J.W., 1986, Introduction to the geochemistry of active and fossil geothermal systems, *in* Henley, R.W., Hedenquist, J.W., and Roberts, P.J., eds., *Guide to the active epithermal (geothermal) systems and precious metal deposits of New Zealand: Monograph Series on Mineral Deposits*, no. 26, p. 1-22.

Hedenquist, J.W., and Lowenstern, J.B., 1994, The role of magmas in forming hydrothermal ore deposits: *Nature*, v. 370, p. 519-527.

Hedenquist, J.W., Arribas, A.R., Gonzalez-Urien, E., 2000, Exploration for Epithermal Gold Deposits: *SEG Reviews*, v. 13, p. 245-277.

Heinrich, C.A., Gunther, D., Audetat, A., Ulrich, T., and Frischknecht, R., 1999, Metal fractionation between magmatic brine and vapor, determined by microanalysis of fluid inclusions: *Geology*, v. 27, p. 755-758.

Izawa, E., Urashima, Y., Ibaraki, K., Suzuki, R., Yokoyama, T., Kawasaki, K., Koga, A., Taguchi, S., 1990, The Hishikari gold deposit: high-grade epithermal veins in Quaternary volcanics of southern Kyushu, Japan: *Journal of Geochemical Exploration*, v. 36, i. 1-3, p. 1-56.

John, D. A., 2001, Miocene and Early Pliocene Epithermal Gold-Silver Deposits in the Northern Great Basin, Western United States: Characteristics, Distribution, and Relationship to Magmatism: *Economic Geology*, v. 96, p. 1827-1853.

John, D.A., and Wallace, A.R., 2000, Epithermal Gold-Silver Deposits Related to the Northern Nevada Rift: *Geology and Ore Deposits 2000: The Great Basin and Beyond Proceedings*, v. 1, p. 155-175.

John, D.A., Wallace, A.R., Ponce, D.A., Fleck, R.B., Conrad, J.E., 2000, New Perspectives on the Geology and Origin of the Northern Nevada Rift: *Geology and Ore Deposits 2000: The Great Basin and Beyond Proceedings*, v. 1, p. 127-154.

Kamenov, G.D., Saunders, J.A., Hames, W.E., Unger, D.L., 2007, Mafic Magmas as Sources for Gold in Middle Miocene Epithermal Deposits of the Northern Great Basin, United States: Evidence from Pb Isotope Compositions of Native Gold: *Economic Geology*, v. 102, p. 1191-1195.

LaPointe, D.D., Tingley, J.V., and Jones, R.B., 1991, Mineral resources of Elko County, Nevada: *Nevada Bureau of Mines and Geology Bulletin*, v. 106, p. 1-236.

Leavitt, E.D., 2004, Midas epithermal gold-silver deposit, Ken Snyder Mine, Elko County, Nevada: *Dissertation/thesis*, University of Nevada at Reno, p. 1-236.

Leavitt, E.D., Spell, T.L., Goldstrand, P.M., Arehart, G.B., 2004, Geochronology of the Midas Low-Sulfidation Epithermal Gold-Silver Deposit, Elko County, Nevada: *Economic Geology*, v. 99, p. 1665-1686.

Leavitt, E.D., and Arehart, G.B., 2005, Alteration, geochemistry, and paragenesis of the Midas epithermal gold-silver deposit, Elko County, Nevada, in Rhoden, H.N., Steininger,

R.C., and Vikre, P.G., eds., Geological Society of Nevada Symposium 2005: Window to the World, Reno, Nevada, May 2005, p. 563-627.

Levinson, A.A., 1974, Introduction to Exploration Geochemistry: Applied Publishing Ltd., p. 1-612.

Lindgren, W., 1906, Ore Deposition and Deep Mining: Economic Geology, v. 1, p. 34-46.

Lindgren, W., 1933, Mineral Deposits: New York, McGraw-Hill, 4th ed., p. 930.

Ludwig, K.R., 2003, User's manual for Isoplot, v. 3.0, a geochronological tool kit for Microsoft Excel: Berkeley Geochronological Center, Special Publication no. 4.

Marek, J.M., 1991, Reserve Review Report on Delamar and Florida Mountains: Independent Mining Consultants, INC., p. 1-32.

McComb, M., 2011, Silver Characterization by SEM/MLA of Midas Eastern Expansion Metallurgical Composites: Newmont unpublished internal report.

Moncada, D., Mutchler, S., Nieto, A., Reynolds, T.J., Rimstidt, J.D., Bodnar, R.J., 2011, Mineral textures and fluid inclusion petrography of the epithermal Ag-Au deposits at Guanajuato, Mexico: Application to exploration: Journal of Geochemical Exploration, In Press, Corrected Proof, p. 1-16.

Mountain, B.W., and Seward, T.M., 1995, The solubility of chalcocite and the speciation of copper in H₂S-bearing solutions at 22°C, In: *Water-Rock Interaction 8*, Kharaka, Y.K., and Chudaev, O.V. (eds.), Rotterdam: Balkema, p. 815-818.

Nash, J.T., Utterback, W.C., and Trudel, W.S., 1995, Geology and geochemistry of Tertiary volcanic host rocks, Sleep gold-silver deposit, Humboldt County, Nevada: U.S. Geological Survey Bulletin, v. 2090, p. 1-63.

Noble, D.C., McCormack, J.K., McKee, E.H., Silberman, M.L., Wallace, A.B., 1988, Time of mineralization in the evolution of the McDermitt caldera-complex, Nevada-Oregon, and the relation of middle Miocene mineralization in the northern Great Basin to coeval regional basaltic magmatic activity: Economic Geology, v. 83, p. 859-863.

Parr, R.G., and Pearson, R.G., 1983, Absolute hardness: companion parameter to absolute negativity: Journal of American Chemistry Society, v. 105, p. 7512-7516.

Pearson, R.G., 1963, Hard and soft acids and bases: Journal of American Chemistry Society, v. 85, p. 3533-3539.

Reed, M.H., and Palandri, J., 2006, Sulfide Mineral Precipitation from Hydrothermal Fluids: Reviews in Mineralogy and Geochemistry, v. 61, p. 609-631.

Redak, S., 2005, Midas Mine, Colorado Grande Vein Trace Element Zonation Study: Newmont unpublished internal report.

Renne, P.R., Swisher, C.C., Deino, A.L., Karner, D.B., Owens, T.L., and DePaolo, D.J., 1998, Intercalibration of standards, absolute ages, and uncertainties in $^{40}\text{Ar}/^{39}\text{Ar}$ dating: Chemical Geology, v. 145, p. 117-152.

Rhys, D.A., 2002, Structural Geology of the Midas Deposit Elko County, Nevada, with Implications for Exploration and Mining: Newmont unpublished report.

Rhys, D.A., and Ross, K.V., 2004, Midas North Mapping Project: Results and Recommendations, with Extended Legend and Interpreted Stratigraphy: Newmont unpublished report.

Richards, J.P., 2009, Postsubduction porphyry Cu-Au and epithermal Au deposits: Products of remelting of subduction-modified lithosphere: *Geology*, v. 37, p. 247-250.

Riederer, M. J., 2007, Fluid Inclusion Study of the Midas Low-Sulfidation Epithermal Au/Ag Mine, Elko County, Nevada: MS thesis University of Wisconsin-Madison, p. 1-144.

Roedder, E., 1984, Fluid Inclusions, *Reviews in Mineralogy*, v. 12, p. 1-644.

Rott, E.H., 1931, Ore Deposits of the Gold Circle Mining District, Elko County, Nevada: *University of Nevada Bulletin*, v. 25, p. 1-29.

Samal, A.R., Mohanty, M.K., Fifiarek, R.H., 2008, Backward elimination procedure for a predictive model of gold concentration: *Journal of Geochemical Exploration*, v. 97, p. 69-82.

Saunders, J.A., 1990, Colloidal transport of gold and silica in epithermal precious metal systems: Evidence from the Sleeper deposit, Nevada: *Geology*, v. 18, p. 757-760.

Saunders, J.A., 1994, Silica and gold textures in bonanza ores of the Sleeper deposit, Humboldt County, Nevada: Evidence for colloids and implications for epithermal ore-forming processes: *Economic Geology*, v. 89, p. 628-638.

Saunders, J.A., Cook, R.B., and Schoenly, P.A., 1996, Electrum disequilibrium crystallization textures in volcanic-hosted epithermal gold deposits in Coyner, A.R., and Fahey, P.L., eds., *Geology and Ore Deposits of the American Cordillera: Geological Society of Nevada Symposium Proceedings*, p. 173-179.

Saunders, J.A., Unger, D.L., Kamenov, G.D., Fayek, M., Hames, W.E., Utterback, W.C., 2008, Genesis of Middle Miocene Yellowstone hotspot-related bonanza epithermal Au-Ag deposits, Northern Great Basin, USA: *Mineralium Deposita*, v. 43, p. 715-734.

Saunders, J.A., Kamenov, G.D., Hofstra, A.H., Unger, D.L., Creaser, R.A., Barra, F., 2011a, "Forensic" geochemical approaches to constrain the source of Au-Ag in low-sulfidation epithermal ores, *in* Steininger, R., and Pennell, W., eds., Great Basin Evolution and Metallogeny: Geological Society of Nevada 2010 Symposium, Reno, NV, May 14-22, 2010, p. 693-700.

Saunders, J.A., Beasley, L., Vikre, P., Unger, D.L., 2011b, Colloidal and physical transport textures exhibited by electrum and naumannite in bonanza epithermal veins from western USA, and their significance, *in* Steininger, R., and Pennell, W., eds., Great Basin Evolution and Metallogeny: Geological Society of Nevada 2010 Symposium, Reno, NV, May 14-22, 2010, p. 825-832.

Saunders, J.A., and Brueseke, M.E., 2012, Volatility of Se and Te during subduction-related distillation and the geochemistry of epithermal ores of the western United States: *Economic Geology*, v. 107, p. 165-172.

Schwarzenbach, G., and Widmer, M., 1966, Die Löslichkeit von Metallsulfiden II, Silbersulfid: *Helv. Chim. Acta* 49, p. 111-123.

Seward, T.M., 1991, The hydrothermal geochemistry of gold, In: *Gold Metallogeny and Exploration*, Foster, R.P. (ed.), Glasgow: Blackie and Son, p. 37-62.

Seward, T.M., and Barnes, H.L., 1997, Chapter 9: Metal Transport by Hydrothermal Ore Fluids, In: *Geochemistry of Hydrothermal Ore Deposits 3*, Barnes H.L. (ed.), Hoboken, NJ: John Wiley and Sons, Inc, p. 435-486.

SGS, 2010, Rocks to Results, A Practical Guide to Laboratory Operations: Minerals Services, 4th Edition, September 2010, p. 41-43.

SGS, 2011, Geochem Analysis: Minerals Services, p. 1-58.

Silberman, M.L., and Berger, B.R., 1985, Relationship of trace-element patterns to alteration and morphology in epithermal precious-metal deposits, *in* Berger, B.R., and Bethke, P.M., eds., *Geology and Geochemistry of Epithermal Systems: Review in Economic Geology*, v. 2, p. 203-232.

Sillitoe, R.H., and Hedenquist, J.W., 2003, Linkages between Volcanotectonic Settings, Ore-Fluid Compositions, and Epithermal Precious Metal Deposits: *Society of Economic Geologists: Special Publication 10*, p. 316-343.

Simmons, S.F., and Christenson, B.W., 1994, Origins of calcite in a boiling geothermal system: *American Journal of Science*, v. 294, p. 361-400.

Simmons, S.F., White, N.C., John, D.A., 2005, Geological Characteristics of Epithermal Precious and Base Metal Deposits: *Economic Geology 100th Anniversary Volume*, p. 485-522.

Simpson, M.P., and Mauk, J.L., 2001, Preliminary descriptions and assessment of fluid inclusions in nineteen vein samples from Midas, Nevada, USA: Newmont unpublished internal report.

Unger, D.L., 2008, Geochronology and Geochemistry of Mid-Miocene Bonanza Low-Sulfidation Epithermal Ores Of The Northern Great Basin, USA: MS thesis Auburn University, p. 1-152.

White, D.E., 1985, Vein and disseminated gold-silver deposits of the Great Basin through space and time: Geologic characteristics of sediment- and volcanic-hosted disseminated gold deposits; search for an occurrence model, Reno, NV: *United States Geological Survey Bulletin*.

Zoback, M.L., McKee, E.H., Blakely, R.J., and Thompson, G.A., 1994, The northern Nevada rift: Regional tectonomagmatic relations and middle Miocene stress direction: Geological Society of America Bulletin, v. 106, p. 371-382.

Zoback, M.L., and Thompson, G.A., 1978, Basin and Range rifting in northern Nevada: Clues from a mid-Miocene rift and its subsequent offsets: Geology, v. 6, p. 111-116.

APPENDIX I

ICP-MS geochemical data and calculation for Ag: Au ratio for Midas eastern veins.

DATE RECEIVED : 2011-09-27 DATE FINALIZED : 2011-10-22																											
PROJECT : "MIDAS/VARIOUS"																											
CERTIFICATE COMMENTS : "1000 gram nominal pulp size ME-MS41:Interference: Ca>10% on ICP-MS As ICP-AES results shown. "																											
PO NUMBER : "17957-555E-RET"																											
SAMPLE DESCRIPTION	WEI-21 kg	FTG-01 START feet	FTG-01 END feet	ME-MS41 As	ME-MS41 Sb	ME-MS41 Hg	ME-MS41 Tl	ME-MS41 Cu	ME-MS41 Pb	ME-MS41 Zn	ME-MS41 Mo	ME-MS41 Ba	ME-MS41 Se	ME-MS41 Te	ME-MS41 S	ME-MS41 Fe	ME-MS41 Mg	ME-MS41 P	ME-MS41 Sr	ME-MS41 V	ME-MS41 Al	ME-MS41 Ca	ME-MS41 K	ME-MS41 Na	Ag-GRA21 Ag	ME-GRA21 Au	
KXC-16143	1.18	1025.4	1026.2	18.2	2.1	0.76	0.26	456	88.4	231	1.69	70	1000	2.1	13600	55300	8600	1880	80.2	167	19600	41500	7100	600	5720	14.7	
KXC-15469	0.78	185.2	186.3	9	2.44	0.11	0.54	83.6	12.1	119	1.6	340	420	0.68	10000	40300	8800	1570	155	149	35000	131000	19900	6500	1290	3.31	
KXC-15589	0.26	890	890.8	6	2.64	14.85	0.85	54.8	20.1	61	3.19	180	300	0.93	5900	10300	900	150	125.5	8	18000	129000	19300	1600	947	5.34	
KXC-23075	0.73	933	933.7	6	1.08	0.06	0.07	30.7	5.1	91	1.92	60	5.6	0.01	2200	65300	17400	2300	91.6	223	21200	59700	3500	900	12.5	6.38	
KXC-22674	2.29	934.7	936.2	45.7	5.06	0.5	0.25	15.8	13.8	117	4.17	20	193.5	0.01	23400	26300	900	280	91.9	4	5400	49500	700	100	675	7.84	
KXC-24831	3.04	386.7	388.4	29.5	3.02	0.53	0.66	13.3	16.2	104	2.43	80	140.5	0.02	25500	28900	2100	370	20.5	6	14000	18400	12000	900	389	35.3	
KXC-37148	1.07	1080	1080.9	35.8	1.56	0.11	0.12	56.2	11.2	88	2.04	40	11.8	0.07	15500	51900	9900	1820	29.8	104	16700	24400	1900	500	62.5	76.9	
KXC-39914	2.24	1223.2	1224.7	26.8	1.55	0.19	0.16	98.2	8.6	152	1.25	50	52.5	0.09	9900	72400	20300	2710	37.9	189	29600	18200	1800	700	165	5.38	
KXC-41333	0.37	448.8	449.6	32	1.8	0.12	0.47	9	7.6	54	1.89	340	11.8	0.01	11400	12500	400	250	88.3	4	21600	176000	13800	7700	18.8	9.53	
KXC-41049	2.48	786.6	788.2	7	1.6	0.31	0.52	20.6	15	67	3.49	200	510	0.61	6100	11000	1400	150	87.7	5	22000	188000	19000	4800	1815	4.19	
KXC-41067	0.31	1091.2	1092.2	9.9	2.14	0.23	0.16	24.9	9.9	53	2.99	20	154.5	0.8	8000	10700	700	330	66.4	11	21900	90600	600	2000	522	4.59	
KXC-44329	0.86	957.3	958.5	8.2	0.64	0.12	0.15	87.7	17.8	82	1.16	50	210	0.57	3600	31100	6000	1110	67.9	74	10200	62600	1300	400	638	3.59	
KXC-44611	0.89	495.3	496.6	14	1.5	0.54	0.06	112	58.1	138	1.47	10	1000	4.24	11600	13300	2000	470	153.5	20	3600	209000	500	100	6070	13.1	
KXC-43017	0.42	849	850.2	1	0.35	0.1	0.32	9	3.9	25	0.57	100	320	0.23	1700	2800	200	90	54.6	1	8100	128000	9700	500	1240	3.34	
KXC-43679	4.5	846.4	849.8	14.4	1.19	0.05	0.03	609	350	440	1.43	40	900	0.2	2800	69000	21400	2810	110	234	25900	33400	1300	800	3440	6.81	
KXC-43680	4.93	849.8	853.6	2.6	0.9	0.02	0.02	26.5	7.1	125	1.07	30	3.9	0.01	1300	74900	21000	2880	99.6	261	23600	36800	900	900	9.38	0.281	
KXC-43681	0.8	853.6	854.8	30.1	1.12	0.08	0.72	60.6	17.7	105	1.73	200	171.5	0.37	10500	25700	5900	750	79.6	51	24300	69600	20700	1800	531	2.13	
KXC-43964	0.59	448.6	449.4	36	2.59	0.27	0.69	16	17.3	86	6	220	440	0.03	18900	22800	900	170	78.2	7	30900	151000	22900	9000	1330	4.25	
KXC-46811	0.32	206.9	207.7	21.1	1.74	1.08	0.11	36.3	49.6	160	2.33	70	830	0.16	16900	23100	3100	150	32.9	4	7400	25400	2100	500	2830	19.9	
KXC-45649	0.28	496.6	497.5	21	1.93	1.62	0.72	13.7	18.7	77	3.83	250	360	0.02	15800	16200	400	170	2700	3	25900	161000	24900	4700	1200	14.7	
KXC-45188	0.95	893.5	894.5	16.3	2.08	0.29	0.32	46.6	24	133	5.02	300	125	0.06	11200	24800	4100	300	32.5	21	17300	15400	5400	600	498	10.4	
KXC-45189	1.27	894.5	896.1	18.2	1.89	0.27	0.41	30.1	17.8	99	11.8	270	65.1	0.04	10500	23500	1200	140	20.1	8	11600	14400	7400	1700	206	3.75	
KXC-46854	0.99	582.2	583	8	1.51	0.34	0.52	34.9	11.3	153	3.83	290	1000	0.12	7100	11800	900	180	32.6	6	19500	114000	19000	3100	3740	9.94	
KXC-47669	1.11	478	478.8	44.7	3.88	1.27	0.69	82.7	234	105	6.74	310	1000	0.06	11200	17600	1200	240	323	18	19000	39800	17200	1800	8740	23.3	
KXC-47565	1.71	146.9	148.6	8	1.65	0.82	0.59	43.5	90	77	2.68	160	1000	0.49	9100	8800	300	100	86.7	3	15600	173000	17500	900	7190	25	
KXC-47602	0.97	473.4	474.8	7	1.24	1.12	0.06	106	64.2	139	3.87	10	1000	0.29	5700	11200	800	60	74.9	5	4100	109000	300	100	4430	12.1	
KXC-47868	0.56	210	211.1	13.8	0.65	0.26	1.03	33	24.1	63	2.12	270	910	0.01	4200	7200	500	130	65.5	5	26200	96600	30100	1200	2930	13.2	
KXC-48488	0.48	525.7	526.5	4	2.97	0.67	0.69	40	48.7	192	3.86	210	1000	0.09	2800	11800	500	120	67.3	8	20400	175000	21800	2000	5350	13.3	
																										Ag Avg.	Au Avg.
																										2213.899	12.59111
																										Ag: Au	175.8304

APPENDIX II

CORE LOG PHOTOS OF MUC-02054 AND CORE LOG DATA FROM VISUAL LOGGER

Core Photos were taken by Teddy Berg of Newmont Mining in July 2011.



































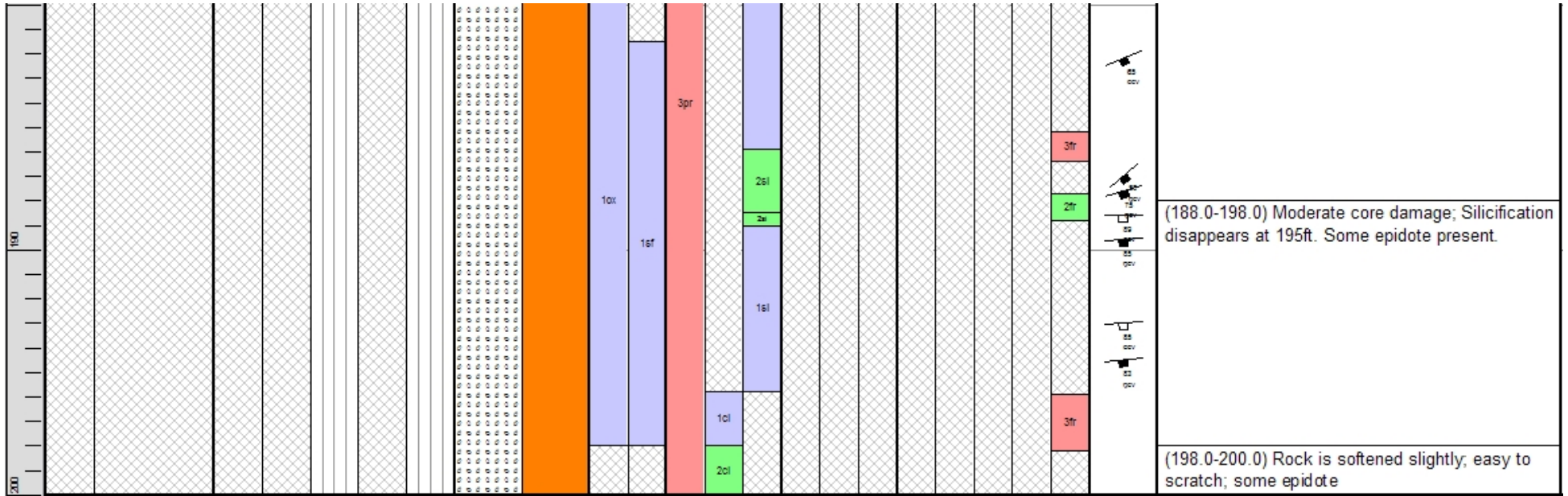


Geotech			Assay		Lithology		Met		Alteration			Vein			Structure				Graphic	Descriptive			
Recovery	Length	Len > 4 in	ROD	Samples	AUPREF_KSM	AGPREF_KSM	Rock Type	Formation	FeOx	Sulfides	Propylitic	Argillic	Silicification	Calcite	Quartz	Naumannite	Fault	Breccia	Gouge	Shearing	Fracture	Graphic	Comments
							Tep3		1ox														(0.0-23.2) First 0.7 in. of core are gravel pieces. Strong propylitic alt. Blt 5-10 ft. large Clasts observed; could be lithic fragment or isolated Silicification. From 18-23.2ft. pyrite can be seen in Clasts. Fe Ox stains can also be seen.
							MST		1ox	1sf													(23.2-25.4) Black mudstone with interspersed Veinlets of pyrite. Bedding can be observed.
									1ox	1sf	3pr												(27.9-28.0) Qtz Stringer; much of core here is broken up. Small Qtz, CaCO3 veins observed in the pieces
									1ox	2sf	2pr												(28.0-38.0) Significant core damage.
										3pr													(38.0-49.0) Strong propylitic alt.; weak silicification; Qtz CaCO3 veinlets observed.

	Geotech				Assay		Lithology		Met		Alteration			Vein			Structure				Graphic	Descriptive		
	Recovery	Length	Len > 4 in	ROD	Samples	AUPREF_KSM	AGPREF_KSM	Rock Type	Formation	FeOx	Sulfides	Propylitic	Argillic	Silicification	Calcite	Quartz	Naumannite	Fault	Breccia	Gouge	Shearing		Fracture	Graphic
40																								
50																								(38.0-49.0) Strong propylitic alt.; weak silicification; Qtz CaCO3 veinlets observed.
60																								(49.0-68.0) More siliceous towards 88 ft.; start to see epidote & weak iron stains. About 65-66ft. small fractures filled with fluorite & calcite; at 68.4ft. slightly larger CaCO3 fracture observed. B/t 68-78ft. tiny qtz veinlets & silicified fragments
70																								(68.0-78.0) Large CaCO3, qtz clast at 74 ft.

Geotech					Assay		Lithology		Met		Alteration			Vein			Structure					Graphic	Descriptive
Recovery	Length	Len > 4 in	RQD	Samples	AUPREF_KSM	AGPREF_KSM	Rock Type	Formation	FeOx	Sulfides	Propylitic	Argillic	Silicification	Calcite	Quartz	Naumannite	Fault	Breccia	Gouge	Shearing	Fracture	Graphic	Comments
																							(78.0-88.0) Breccia; mostly cast-supported with small sections matrix-supported. clasts are siltstone, fiamme; matrix is SiO2, flourite, brassy sulfides (pyrite). Upper margin is a vuggy silicified zone; limonite iron staining; shearing fabrics (texture obscured).
																							(88.0-89.2) Breccia; mostly cast-supported with small sections matrix-supported. clasts are siltstone, fiamme; matrix is SiO2, flourite, brassy sulfides (pyrite). Upper margin is a vuggy silicified zone; limonite iron staining; shearing fabrics (texture obscured).
																							(89.2-89.4) Outside margin shows intense silicification.
																							(89.4-98.0) Silicification still strong; pyrite, CaCO3, flourite filled in fractures, veinlets. Epidote halos surround fractures. Minor qtz vein at 94.1ft. vugs out at upper margin; pyrite, flourite found.
																							(98.0-108.0) Silicification temporarily decreases and then increases again with depth. Some silicic fragments found in tuff. More iron staining seen. At 101ft. CaCO3 filled fracture seen.
																							(108.0-111.5) Less silicification; iron staining; pyrite present; minor CaCO3 filled fractures. Fairly significant vein of CaCO3 qtz, flourite at 109.9-110.6ft.
																							(111.5-111.9) No sample. Taken out for density analysis.

	Geotech				Assay		Lithology	Met	Alteration			Vein			Structure				Graphic	Descriptive				
	Recovery	Length	Len > 4 in	RQD	Samples	AUPREF_KSM			AGPREF_KSM	Rock Type	Formation	FeOx	Sulfides	Propylitic	Argillic	Silicification	Calcite	Quartz			Naumannite	Fault	Breccia	Gouge
120																								analysis.
																								(111.9-112.9) Small qtz, CaCO3, flourite vein found at 112.4-112.7 ft.
																								(112.9-113.3) No Sample.
																								(113.3-116.5) Start to see vein at 114.7ft. cutting down the hole; pinches out at 115.69 ft. From 115.69-116.47 ft. vein becomes more prominent; start to see naumannite; weak to no banding. Calcite vuggy.
																								(116.5-116.8) No Sample.
																								(116.8-118.0) Qtz, CaCO3, flourite vein with blebby to weakly-banded naumannite. Hematite staining; frothy texture (decalcification); amethyst; Milky quartz = lots of adularia.
																								(118.0-119.5) Vein: flourite matrix breccia w/ qtz CaCO3, naumannite, vein clasts; naumannite clots w/ vein; weakly banded; moves to fluorite, pyrite; more banding towards 119 ft.
																								(119.5-119.8) No Sample
																								(119.8-120.4) Vein: Slight, frothy texture in flourite; milky quartz; moderate naumannite banding; little calcite present; small inclusion of Tep3.
																								(120.4-121.9) Tep3 with small vein inclusion of qtz, CaCO3 with iron staining.
																								(121.9-123.2) Vein: weakly-banded qtz, CaCO3, flourite vein w/ minor naumannite; flourite forms vugs; texturally late; few lithic clasts present (Tep3, possibly mafic); flourite-very purple.
																								(123.2-138.0) Tep3 with strong silicification: lots of pyrite; goes from chlorite-rich to epidote; autobrecciation ; towards 138ft. starts bleaching; some small qtz, calcite vein inclusions. Crushed pumice also seen.
																								(138.0-148.0) Moderate silicification; Chlorite-rich; moderate iron staining; few small fractures; pyrite seen; calcite-filled fractures. Massive fracturing of the core from 149.6-150.9 ft.
																								(148.0-158.0) Significant damage to core. Few tiny fractures; some iron staining.
130																								
140																								
150																								

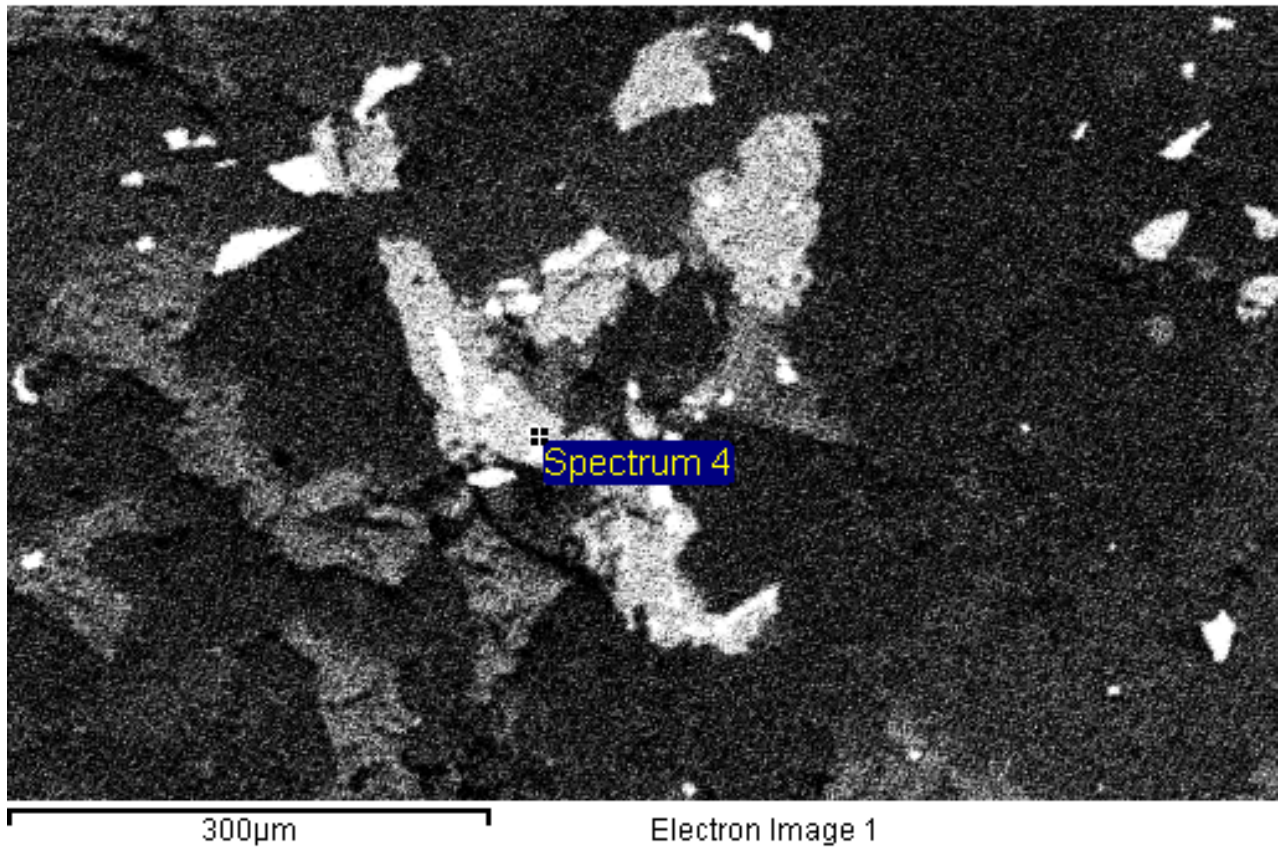


APPENDIX III

Selected Scanning Electron Microscope – Energy Dispersive Spectrometry (SEM/EDAX) Data.

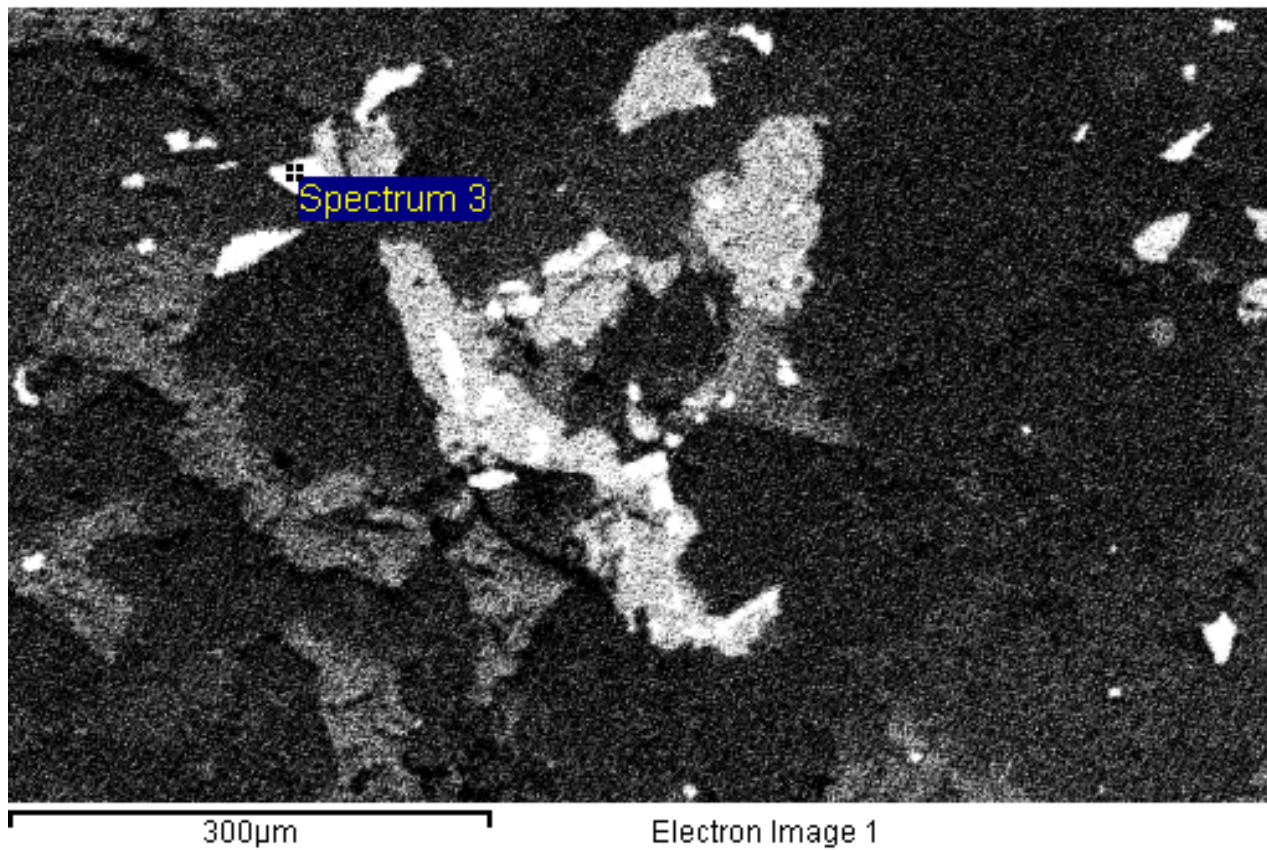
GP (905) Vein – Electrum-Pyrite Grain Boundary

27/10/2011 17:24:55

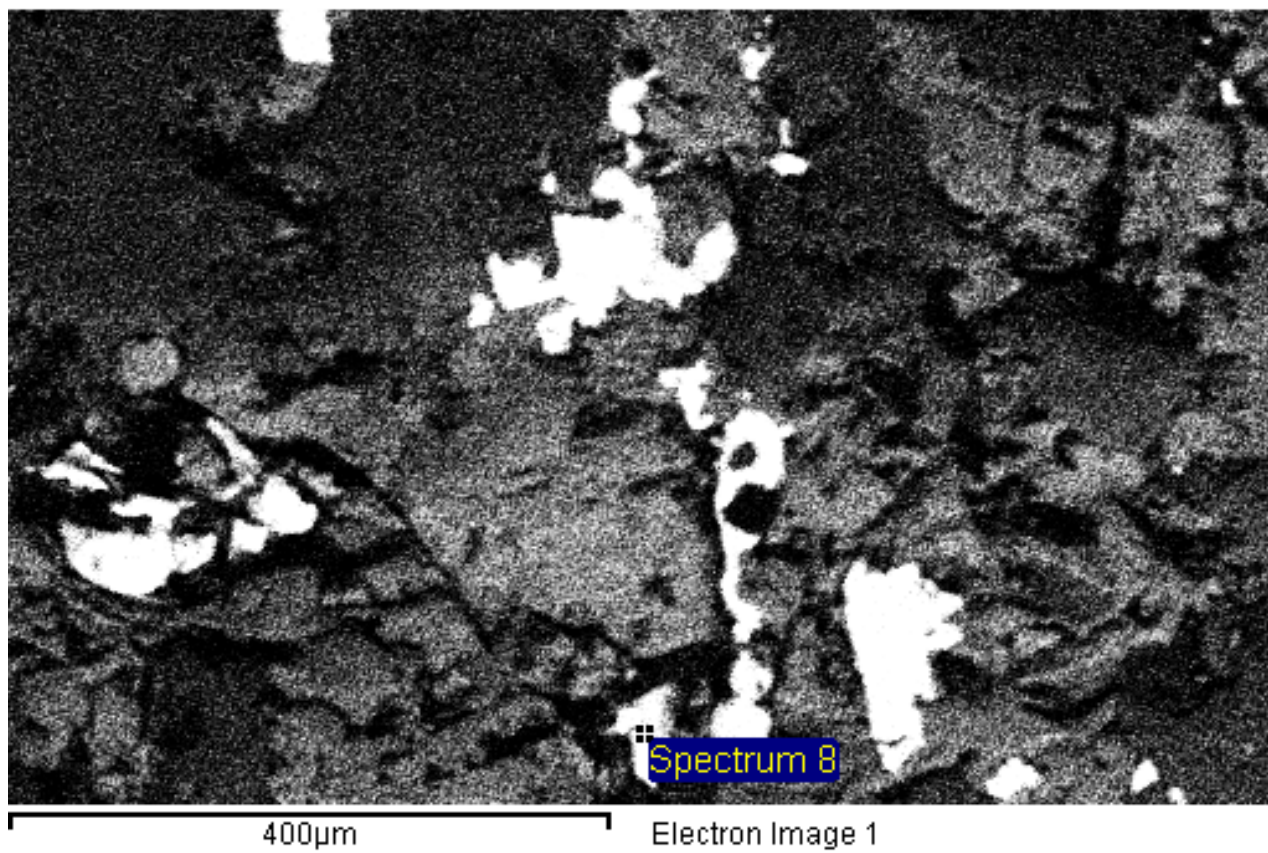


Element	Weight%	Atomic%
S K	25.25	53.79
Fe K	15.34	18.76
Ag L	23.93	15.15
Au M	35.48	12.30
Totals	100.00	

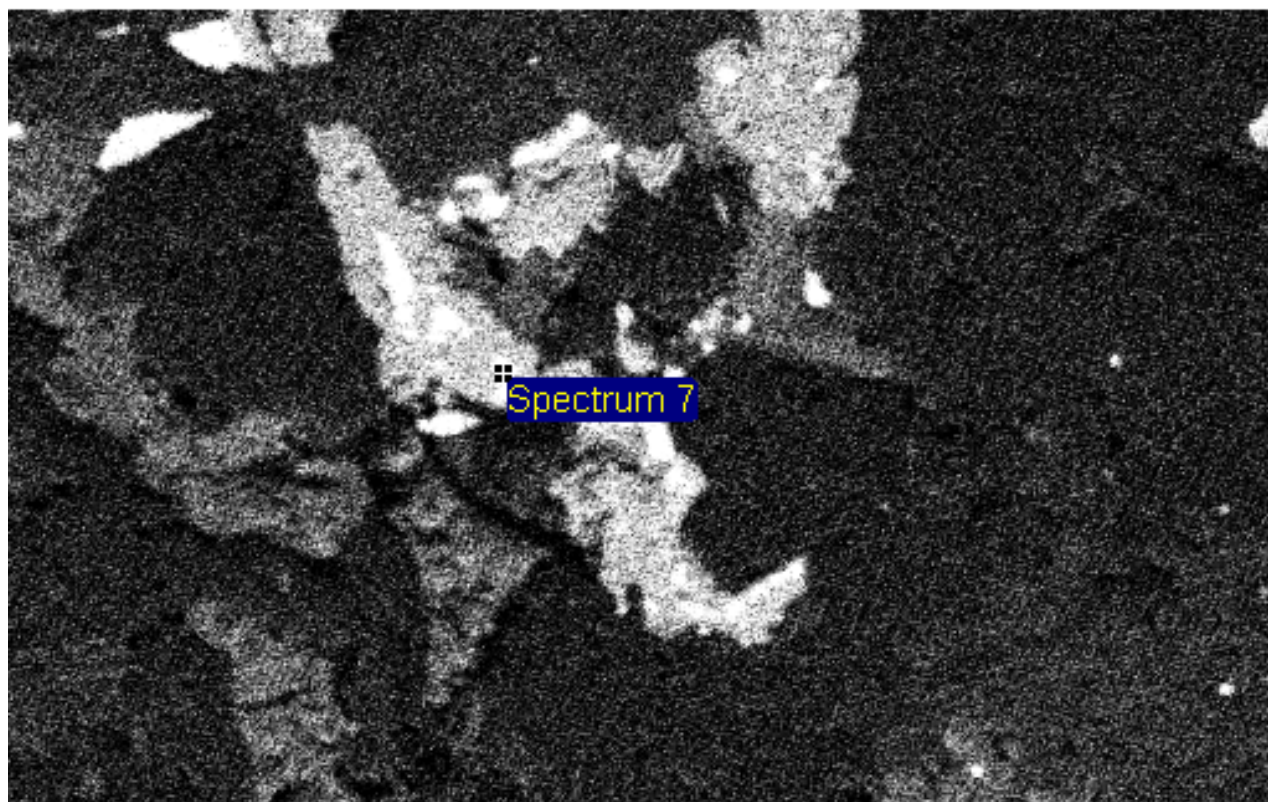
INCA



Element	Weight%	Atomic%
S K	4.23	12.24
Se L	17.01	20.00
Ag L	78.76	67.77
Totals	100.00	



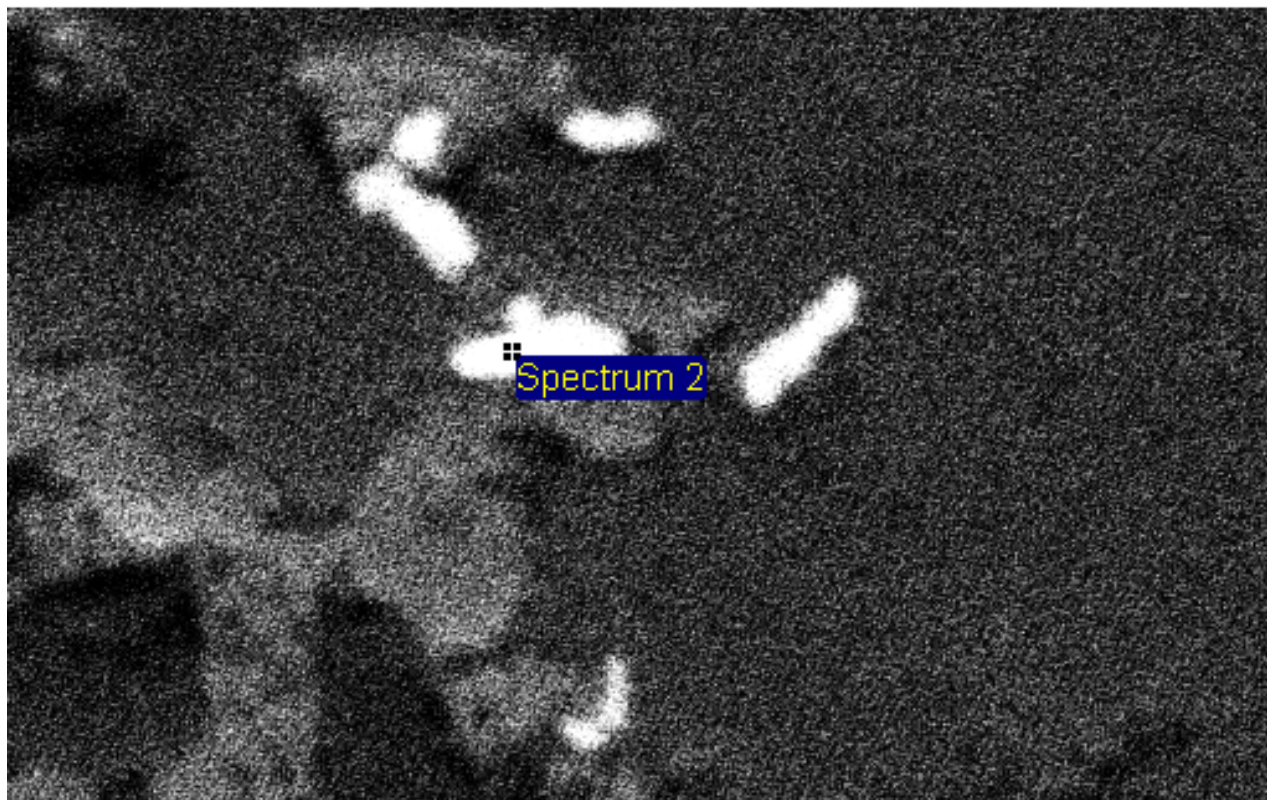
Element	Weight%	Atomic%
S K	3.56	11.03
Ag L	96.44	88.97
Totals	100.00	



300µm

Electron Image 1

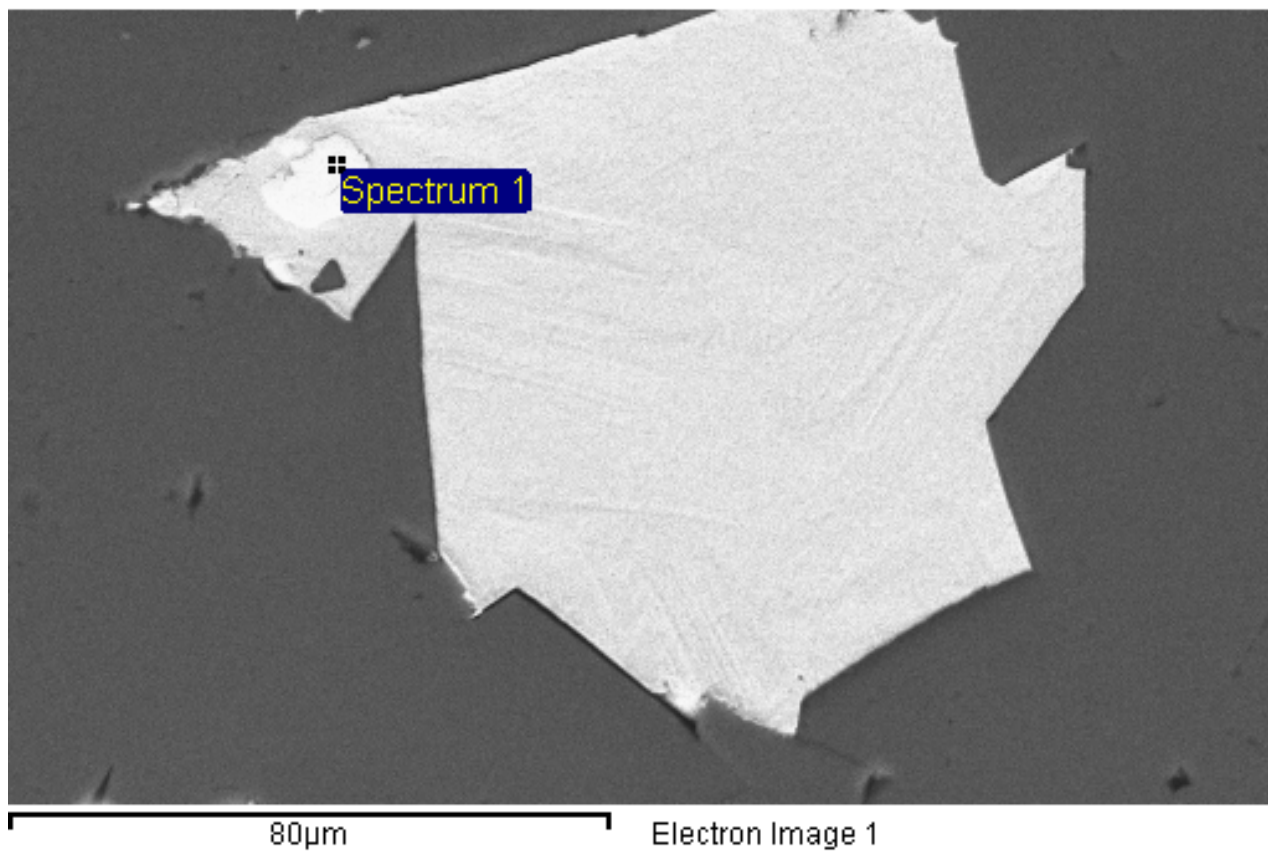
Element	Weight%	Atomic%
Fe K	5.64	14.95
Ag L	23.75	32.61
Au M	45.96	34.56
Tl M	24.66	17.87
Totals	100.00	



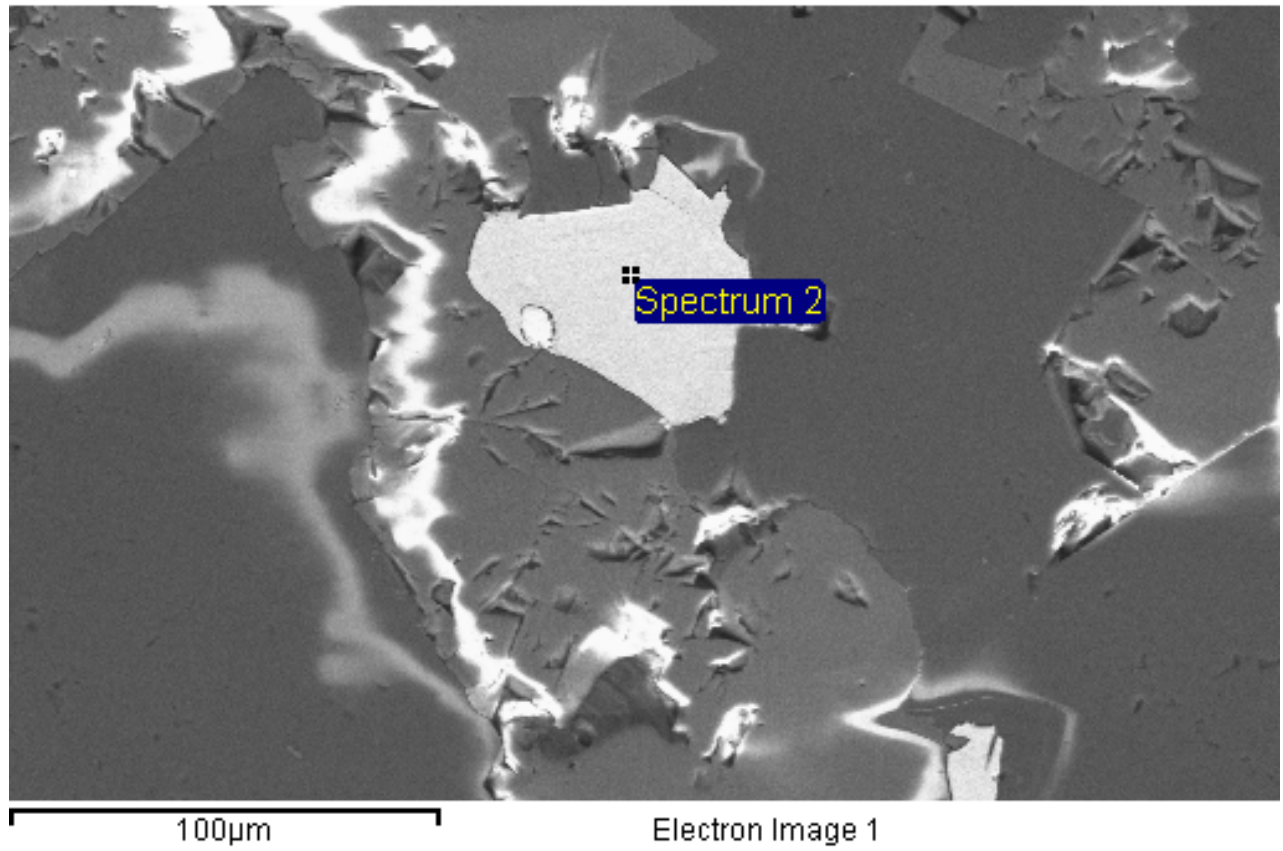
100µm

Electron Image 1

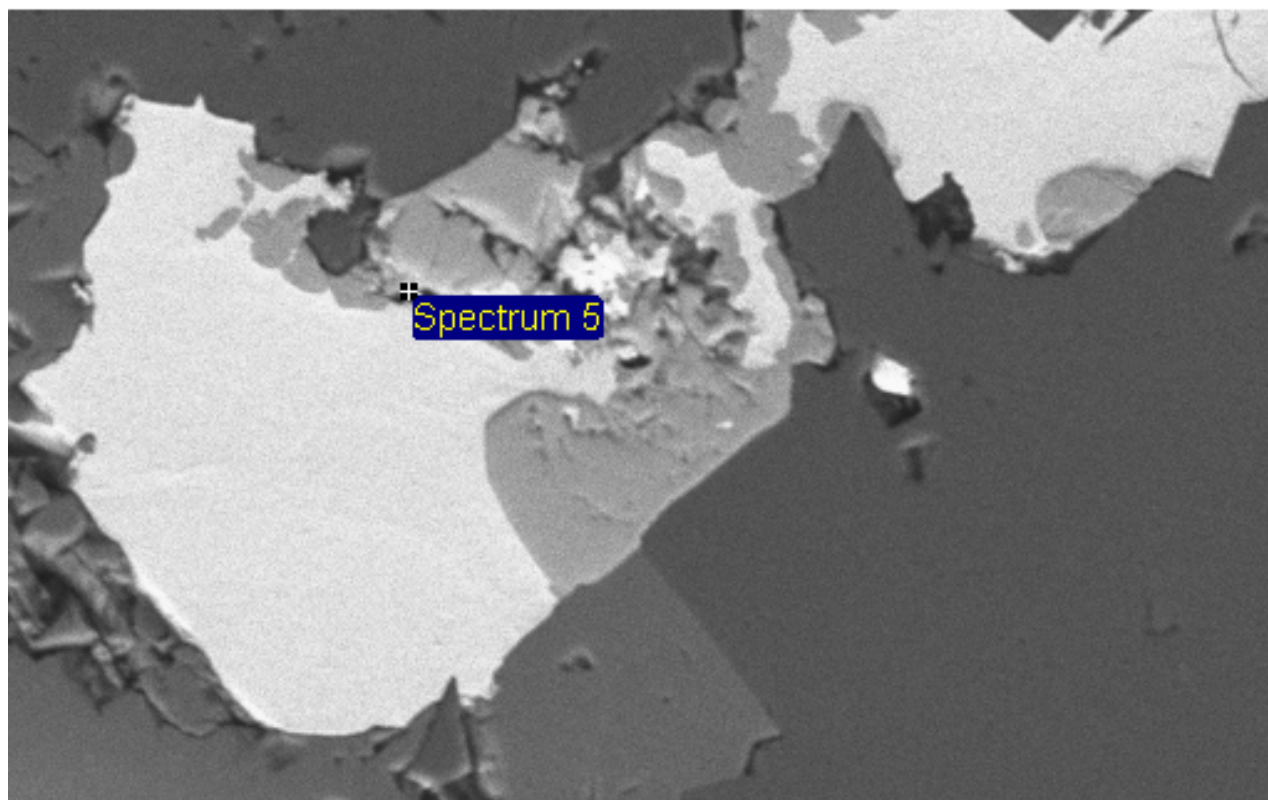
Element	Weight%	Atomic%
Pb M	100.00	100.00
Totals	100.00	



Element	Weight%	Atomic%
Ag L	31.54	45.69
Au M	68.46	54.31
Totals	100.00	



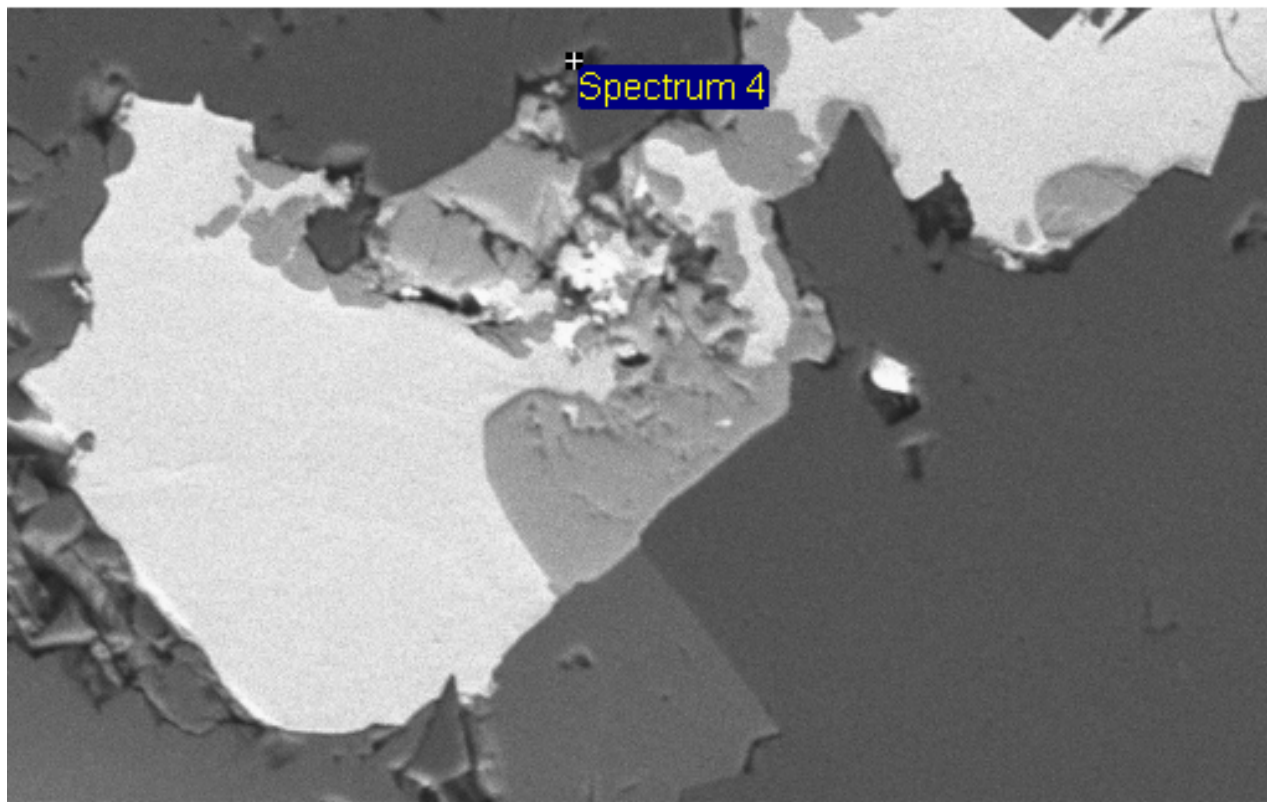
Element	Weight%	Atomic%
S K	4.15	11.98
Se L	18.61	21.80
Ag L	77.24	66.23
Totals	100.00	



100µm

Electron Image 1

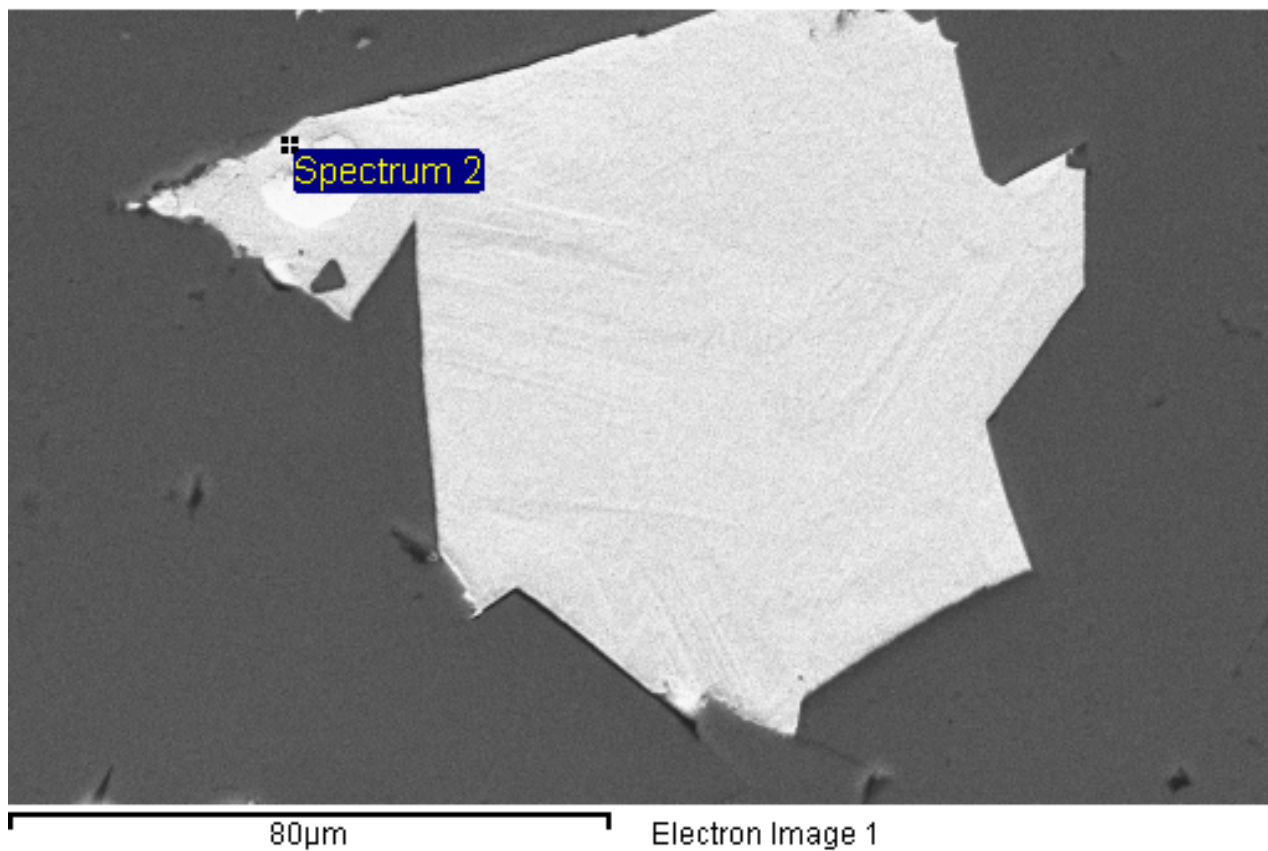
Element	Weight%	Atomic%
S K	10.90	32.10
Zn K	13.88	20.06
Ag L	29.72	26.02
Au M	45.50	21.82
Totals	100.00	



100µm

Electron Image 1

Element	Weight%	Atomic%
Au M	100.00	100.00
Totals	100.00	



Element	Weight%	Atomic%
Pb M	100.00	100.00
Totals	100.00	